

NAVAL POSTGRADUATE SCHOOL

Monterey, California



THESIS

**DEVELOPMENT AND CONTROL OF A THREE-AXIS
SATELLITE SIMULATOR FOR THE BIFOCAL RELAY
MIRROR INITIATIVE**

by

Vincent S. Chernesky

December 2001

Thesis Advisor:

Michael G. Spencer

Thesis Co-Advisor:

Brij N. Agrawal

Approved for public release; Distribution is unlimited

Report Documentation Page

Report Date 19Dec2001	Report Type N/A	Dates Covered (from... to) - -
Title and Subtitle Development and Control of a Three-Axis Satellite Simulator for the Bifocal Relay Mirror Initiative		Contract Number
		Grant Number
		Program Element Number
Author(s) Chernesky, Vincent S.		Project Number
		Task Number
		Work Unit Number
Performing Organization Name(s) and Address(es) Naval Postgraduate School Monterey, California		Performing Organization Report Number
Sponsoring/Monitoring Agency Name(s) and Address(es)		Sponsor/Monitor's Acronym(s)
		Sponsor/Monitor's Report Number(s)
Distribution/Availability Statement Approved for public release, distribution unlimited		
Supplementary Notes		
Abstract		
Subject Terms		
Report Classification unclassified	Classification of this page unclassified	
Classification of Abstract unclassified	Limitation of Abstract UU	
Number of Pages 104		

THIS PAGE INTENTIONALLY LEFT BLANK

REPORT DOCUMENTATION PAGE

Form Approved OMB No. 0704-0188

Public reporting burden for this collection of information is estimated to average 1 hour per response, including the time for reviewing instruction, searching existing data sources, gathering and maintaining the data needed, and completing and reviewing the collection of information. Send comments regarding this burden estimate or any other aspect of this collection of information, including suggestions for reducing this burden, to Washington headquarters Services, Directorate for Information Operations and Reports, 1215 Jefferson Davis Highway, Suite 1204, Arlington, VA 22202-4302, and to the Office of Management and Budget, Paperwork Reduction Project (0704-0188) Washington DC 20503.

1. AGENCY USE ONLY (Leave blank)	2. REPORT DATE December 2001	3. REPORT TYPE AND DATES COVERED Master's Thesis	
4. TITLE AND SUBTITLE: Development and Control of a Three-Axis Satellite Simulator for the Bifocal Relay Mirror Initiative		5. FUNDING NUMBERS	
6. AUTHOR(S) Chernesky, Vincent S.			
7. PERFORMING ORGANIZATION NAME(S) AND ADDRESS(ES) Naval Postgraduate School Monterey, CA 93943-5000		8. PERFORMING ORGANIZATION REPORT NUMBER	
9. SPONSORING /MONITORING AGENCY NAME(S) AND ADDRESS(ES) N/A		10. SPONSORING/MONITORING AGENCY REPORT NUMBER	
11. SUPPLEMENTARY NOTES The views expressed in this thesis are those of the author and do not reflect the official policy or position of the Department of Defense or the U.S. Government.			
12a. DISTRIBUTION / AVAILABILITY STATEMENT Approved for public release; Distribution is unlimited		12b. DISTRIBUTION CODE	
13. ABSTRACT (maximum 200 words) The Three Axis Satellite Simulator (TASS) is a 4-foot diameter octagonal platform supported on a spherical air bearing. The platform hosts several satellite subsystems, including rate gyros, reaction wheels, thrusters, sun sensors, and an onboard control computer. This free-floating design allows for realistic emulation of satellite attitude dynamics in a laboratory environment. The bifocal relay mirror spacecraft system is composed of two optically coupled telescopes used to redirect the laser light from ground-based, aircraft-based or spacecraft based lasers to distant points on the earth or in space for a variety of non-weapon, force enhancement missions. A developmental version of this system was integrated onto the TASS as an auxiliary payload. The objective of this thesis was to develop and test the integrated optics and TASS system. This effort included hardware design, fabrication, and installation; platform mass property determination; and the development and testing of control laws and signal processing routines utilizing MATLAB and SIMULINK. The combination of the TASS with the bifocal relay mirror payload allowed for dynamic, real-time testing and validation of the target acquisition, tracking, and laser beam pointing technologies as well as satellite stabilization			
14. SUBJECT TERMS Attitude determination, Attitude control, MATLAB, SIMULINK, Satellite Simulator, Air Bearing			15. NUMBER OF PAGES
16. PRICE CODE			
17. SECURITY CLASSIFICATION OF REPORT Unclassified	18. SECURITY CLASSIFICATION OF THIS PAGE Unclassified	19. SECURITY CLASSIFICATION OF ABSTRACT Unclassified	20. LIMITATION OF ABSTRACT UL

NSN 7540-01-280-5500

Standard Form 298 (Rev. 2-89)
Prescribed by ANSI Std. Z39-18

THIS PAGE INTENTIONALLY LEFT BLANK

Approved for public release; Distribution is unlimited

**DEVELOPMENT AND CONTROL OF A THREE-AXIS SATELLITE
SIMULATOR FOR THE BIFOCAL RELAY MIRROR INITIATIVE**

Vincent S. Chernesky
Lieutenant, United States Navy
B.S., Rensselaer Polytechnic Institute, 1994

Submitted in partial fulfillment of the
requirements for the degree of

MASTERS OF SCIENCE IN ASTRONAUTICAL ENGINEERING

from the

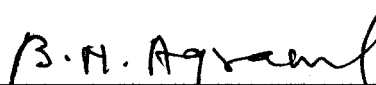
NAVAL POSTGRADUATE SCHOOL
December 2001

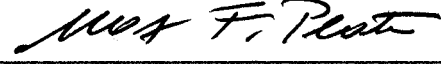
Author:


Vincent S. Chernesky

Approved by:


Michael G. Spencer, Thesis Advisor


Brij N. Agrawal, Co-Advisor


Max F. Platzer

Max F. Platzer, Chairman
Department of Aeronautics and Astronautics

THIS PAGE INTENTIONALLY LEFT BLANK

ABSTRACT

The Three Axis Satellite Simulator (TASS) is a 4-foot diameter octagonal platform supported on a spherical air bearing. The platform hosts several satellite subsystems, including rate gyros, reaction wheels, thrusters, sun sensors, and an onboard control computer. This free-floating design allows for realistic emulation of satellite attitude dynamics in a laboratory environment.

The bifocal relay mirror spacecraft system is composed of two optically coupled telescopes used to redirect the laser light from ground-based, aircraft-based or spacecraft based lasers to distant points on the earth or in space for a variety of non-weapon, force enhancement missions. A developmental version of this system was integrated onto the TASS as an auxiliary payload.

The objective of this thesis was to develop and test the integrated optics and TASS system. This effort included hardware design, fabrication, and installation; platform mass property determination; and the development and testing of control laws and signal processing routines utilizing MATLAB and SIMULINK. The combination of the TASS with the bifocal relay mirror payload allowed for dynamic, real-time testing and validation of the target acquisition, tracking, and laser beam pointing technologies as well as satellite stabilization.

THIS PAGE INTENTIONALLY LEFT BLANK

TABLE OF CONTENTS

I.	INTRODUCTION.....	1
A.	BACKGROUND	1
1.	Bifocal Relay Mirror and DII	1
2.	Spacecraft Research and Design Center.....	5
B.	THREE-AXIS SATELLITE SIMULATOR (TASS).....	5
1.	Hardware	5
2.	Software	5
3.	Bifocal Relay Mirror Payload.....	6
C.	SCOPE OF THESIS	6
II.	HARDWARE DEVELOPMENT	7
A.	OVERVIEW	7
B.	REFERENCE FRAMES AND AXES.....	10
1.	GDC Axes	10
2.	Control Axes.....	11
3.	Principal Axes.....	14
4.	Mass Properties Axes.....	15
C.	POWER SYSTEM.....	15
1.	Original Power System Design	16
2.	Battery Voltage and Capacity.....	17
3.	Video-Capable Power System Modification.....	18
D.	REACTION WHEELS.....	20
1.	Reaction Wheel Commanding and Overspeed.....	20
2.	Failure and Troubleshooting Reaction Wheel #012	22
3.	Voltage/Current Clamp Development	23
E.	RATE GYROS	24
F.	SUN SENSORS	24
1.	Original Sun Sensor Design	24
2.	Three-Axis Sun Sensor Modification	25
3.	Angular Calibration of Sun Sensor	25
G.	MAGNETOMETER.....	30
H.	VIDEO SYSTEM	31
I.	MASS PROPERTIES	34
1.	Background	34
2.	Mass.....	35
3.	Moments of Inertia and Principal Axes	36
4.	Balancing	38
III.	SOFTWARE DEVELOPMENT & SIGNAL PROCESSING.....	39
A.	INTERFACE CARDS	39
B.	MATLAB/SIMULINK/REALTIME WORKSHOP INTEGRATION	39
C.	SIGNAL PROCESSING	40

1. Rate Gyros	40
2. Sun Sensor	42
D. CONTROLLER DEVELOPMENT.....	44
IV. SYSTEM ANALYSIS.....	49
A. RESULTS	49
V. FUTURE SENSORS AND SYSTEMS	55
A. SENSOR IMPROVEMENTS.....	55
1. Sensor Requirements.....	55
2. Pseudolite GPS	56
3. Star Trackers.....	57
4. Inertial Measurement Unit.....	57
5. Laser Tracking.....	58
B. BALANCING IMPROVEMENTS.....	59
1. Active Balancing Unit.....	59
2. CAD Principal Axes Determination	61
C. SYSTEM CHARACTERIZATION.....	62
1. Gain Determination	62
2. Alternate Control Methods	62
VI. SUMMARY AND CONCLUSIONS	63
APPENDIX A: MASS PROPERTIES SPREADSHEET.....	65
APPENDIX B: SIMULINK DIAGRAMS.....	67
APPENDIX C: VOLTAGE/CURRENT CLAMP DESIGN.....	73
APPENDIX D: DAQCARD-1200 SIGNAL SUMMARY	77
APPENDIX E: VIDEO HARDWARE DIAGRAMS	79
APPENDIX F: POWER ANALYSIS.....	81
APPENDIX G: VIDEO POWER SCHEMATIC.....	83
LIST OF REFERENCES.....	85
INITIAL DISTRIBUTION LIST	87

LIST OF FIGURES

Figure 1.	Relay Mirror Experiment Operation [From Ref. 1].....	1
Figure 2.	SDI Relay Mirror Operational Scenario [From Ref. 1].....	2
Figure 3.	Bifocal Relay Mirror Spacecraft.....	3
Figure 4.	Bifocal Relay Mirror Operational Concept.....	4
Figure 5.	Bifocal Relay Mirror Spacecraft Optics [From Ref. 2]	4
Figure 6.	Subsystem Layout.....	8
Figure 7.	Bifocal Relay Mirror Payload Layout.....	9
Figure 8.	TASS Top View.....	9
Figure 9.	TASS Bottom View	10
Figure 10.	GDC Axis System.....	11
Figure 11.	Rate gyro dynamic outputs	12
Figure 12.	Sun Sensor Dynamic Outputs	13
Figure 13.	Reaction Wheel Control Output.....	13
Figure 14.	Control Coordinate System.....	14
Figure 15.	Mass Properties Coordinate System	15
Figure 16.	TASS Power System as Originally Designed.....	16
Figure 17.	Re-design of TASS power system	18
Figure 18.	BRMP Power Upgrade	19
Figure 19.	Video Power Supply Hardware	19
Figure 20.	Reaction Wheel Location.....	20
Figure 21.	Overspeed Control Box.....	21
Figure 22.	Sun Sensor Y-Axis Dynamic Range.....	25
Figure 23.	X _C Axis Sun Sensor Voltage vs. Angle	27
Figure 24.	Y _C Axis Sun Sensor Voltage vs. Angle, 0 to 90 degrees scale.....	28
Figure 25.	Y _C Axis Sun Sensor Voltage vs. Angle, -45 to 45 degrees scale.....	28
Figure 26.	Z _C Axis Sun Sensor Voltage vs. Angle.....	29
Figure 27.	Sun Sensor X _C and Z _C Fields of View	30
Figure 28.	AFRL Electronics Hardware.....	31
Figure 29.	BRMP Operational Concept	32
Figure 30.	Optical Train Diagram	33
Figure 31.	Video Power Supply	34
Figure 32.	Determination of Principal Axes	37
Figure 33.	Raw Rate Gyro Signal Illustrating Noise Level	40
Figure 34.	Raw Rate gyro Signal and 1 st Order Butterworth Filter Output	41
Figure 35.	Raw Rate Gyro Signal and CC Filter Output.....	42
Figure 36.	Sun Sensor Output, Note Quantization in Y _C Axis.....	43
Figure 37.	Filter Comparison	44
Figure 38.	Controller Front End Screen	45
Figure 39.	Single Axis PID Control Implementation.....	47
Figure 40.	TASS Position Data	50
Figure 41.	Filtered Sun Sensor Data in Principal Axes.....	51

Figure 42.	Raw Rate Gyro Data, Control Axis System	52
Figure 43.	Filtered Rate Gyro Data, Principal Axis System	53
Figure 44.	Control Output to Reaction Wheels, Control Axis Frame.....	53
Figure 45.	Photo Of BRMP Operations – Integrated Tracking.....	54
Figure 46.	BRMP With Alignment Tracking Sensor.....	59
Figure 47.	Reactionless Automatic Balancing Unit	61
Figure 48.	Controller Front End.....	67
Figure 49.	Hardware Interface and Data Flow.....	68
Figure 50.	Rate Gyro Filtering and DCM	68
Figure 51.	Commanded Position DCM.....	69
Figure 52.	Sun Sensor Filtering and DCM.....	69
Figure 53.	X_p Axis PID Controller.....	70
Figure 54.	Y_p Axis PID Controller.....	70
Figure 55.	Z_p Axis PID Controller	71
Figure 56.	Reaction DCM	71
Figure 57.	Voltage/Current Clamp Circuit.....	73
Figure 58.	Clamp Circuit Housing – Base	74
Figure 59.	Clamp Circuit Housing – Transistor Restraint.....	75
Figure 60.	Clamp Circuit Housing – Mounting Shield	76
Figure 61.	Terminal Strip Wiring Diagram.....	79
Figure 62.	AFRL Controller Hardware Wiring Diagram.....	80
Figure 63.	Video Power Supply Schematic.....	83

LIST OF TABLES

Table 1.	Power System Signal Summary.....	20
Table 2.	Reaction Wheel Signal Summary	22
Table 3.	Rate Gyro Signal Summary	24
Table 4.	Sun Sensor Signal Summary.....	29
Table 5.	Magnetometer Signal Summary	30
Table 6.	Gains Used For Full System Test	49
Table 7.	Mass Properties – Positions and Dimensions	65
Table 8.	Mass Properties – Moments of Inertia	66
Table 9.	Signal Summary for DAQcard at Memory Location 1000h.....	77
Table 10.	Signal Summary for DAQcard at Memory Location 1200h.....	78
Table 11.	TASS Average Power Requirements.....	81
Table 12.	TASS Maximum Power Requirements.....	82

THIS PAGE INTENTIONALLY LEFT BLANK

ACKNOWLEDGMENTS

The author would like to thank the following people for their invaluable guidance and assistance provided in the completion of this thesis:

Profs. Michael Spencer & Brij Agrawal – For allowing me to freely exercise my skill and imagination in making this piece of equipment operational.

Prof. Barry Leonard – For being the voice of experience and reason throughout my time at NPS.

Mr. Ron Phelps – For his expertise and assistance in circuit design and construction. (And for teaching me how to solder!)

Prof. Roberto Cristi – For his invaluable guidance in signal processing.

Dr. Marcello Romano – For introducing me to the Bifocal Relay Mirror Payload.

And to Corey, for being the most loving and supportive wife and dive buddy a man could hope for.

THIS PAGE INTENTIONALLY LEFT BLANK

I. INTRODUCTION

A. BACKGROUND

1. Bifocal Relay Mirror and DII

During the late 1980s and early 1990s interest in space-based mirrors was expressed for the purpose of furthering the Strategic Defense Initiative (SDI) program, known colloquially then as “Star Wars”. Most notable of these experiments was the Relay Mirror Experiment (RME), which successfully proved the technology involved in targeting a ground-based laser on an orbiting satellite and successfully delivering reflected laser radiation to another ground facility (Figure 1).

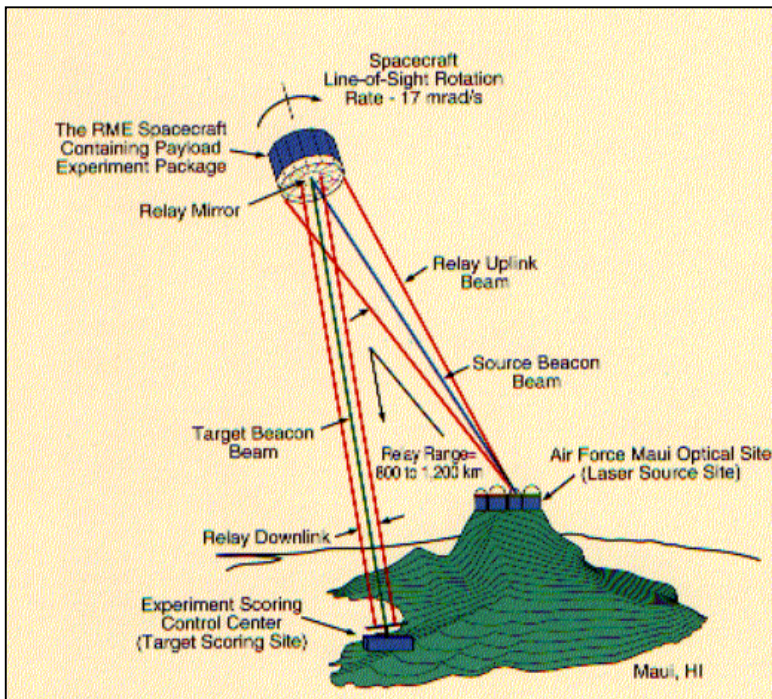


Figure 1. Relay Mirror Experiment Operation [From Ref. 1]

The RME stemmed from the SDI requirement for a space platform capable of reflecting a beam from a cooperative ground based laser to another cooperative space-mirror. This spacecraft was the first step in meeting the challenges particular to this mission, including spacecraft and beam pointing and tracking, and spacecraft jitter control. The RME also demonstrated autonomous spacecraft attitude control, receiving only a telemetry update daily [Ref. 1].

Three lasers were used in the operation of the RME, two beacon lasers and the main relay beam. A beacon laser was originated at both source and target ground sites towards the RME spacecraft. These beams entered an onboard optical train that sensed the orientation of each incoming beam, and slewed the primary mirror to the proper angle to reflect the main beam from the source to the target. The reflected main relay beam and source beacon beam were sensed at the target location. Jitter and accuracy were measured both at the target site and onboard the spacecraft during each encounter.

The tests were successful and the results were significantly better than expected, creating a new benchmark for future systems to be measured against.

The ultimate goals of this system were a space-based anti-ballistic missile system using mirrors to engage the target missiles (Figure 2). However, changes in public policy dictated that the SDIO (now Ballistic Missile Defense Organization (BMDO)) shift its focus away from the space mirror concept. The Air Force continued working the technical challenges of laser acquisition, tracking, and pointing, concentrating its efforts on the Airborne Laser (ABL) system. The ABL system has been highly successful, and much expertise has been gained in the area of jitter control, beam tracking and pointing, and beam forming. Much of this expertise resides at the Air Force Research Laboratory (AFRL) in Albuquerque, New Mexico.

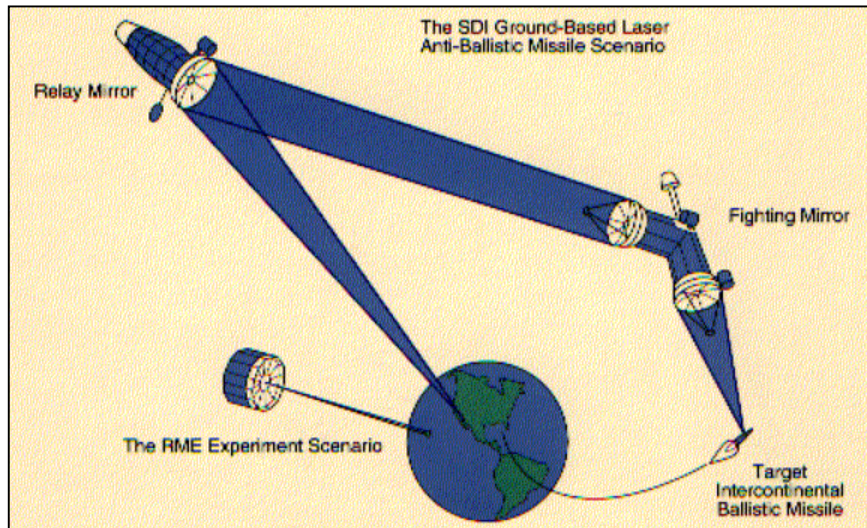


Figure 2. SDI Relay Mirror Operational Scenario [From Ref. 1]

In the late 1990s, a concept study performed by AFRL validated potential missions for a space-based optical relay mirror for imaging and intelligence purposes, incorporating technologies developed in the decade since the RME. In 2000, a preliminary satellite design was completed by a team of Naval Postgraduate School masters students, resulting in the scissors-like Bifocal Relay Mirror spacecraft (Figure 3).

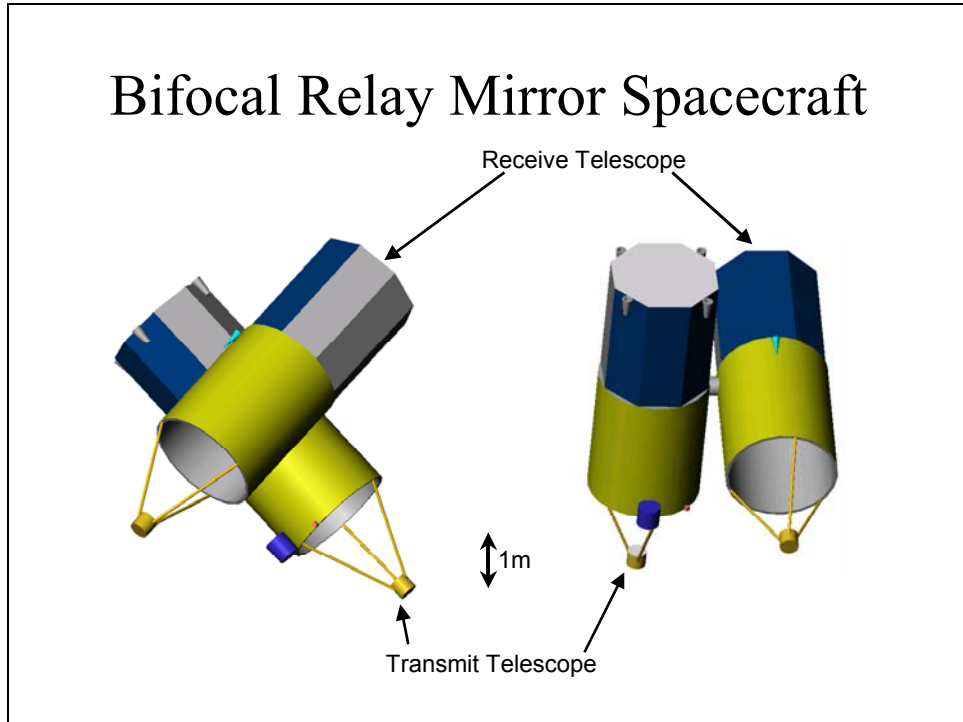


Figure 3. Bifocal Relay Mirror Spacecraft

The Bifocal Relay Mirror spacecraft consists of two optically coupled telescopes used to redirect the light from a ground-based laser to a distant target (Figure 4). A receiver telescope collects the incoming laser energy and channels it through internal relay optics to a transmitter telescope. The transmitter telescope directs the energy against the desired target. The relay optics between the two telescopes includes adaptive optics for correcting wave front aberration and beam steering mirrors (Figure 5).

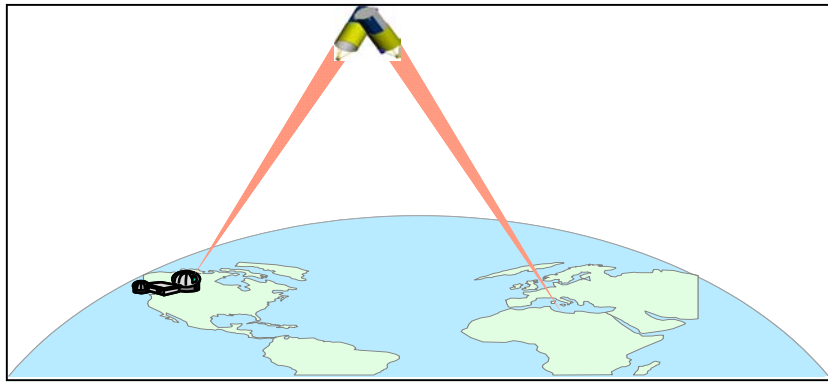


Figure 4. Bifocal Relay Mirror Operational Concept

Bifocal Relay Mirror Spacecraft Optics

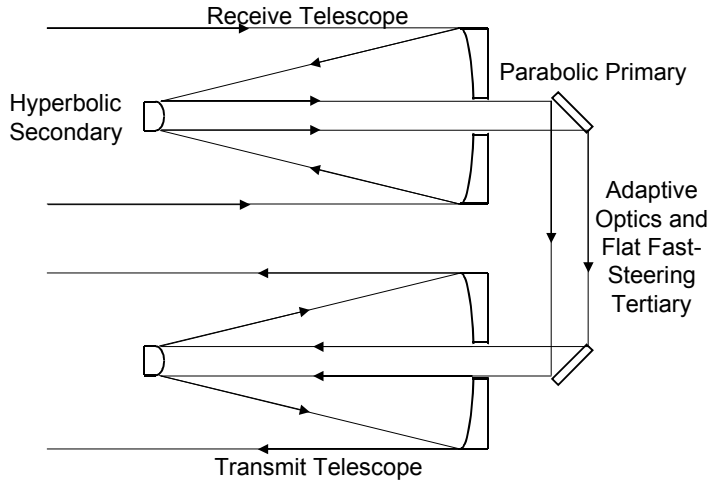


Figure 5. Bifocal Relay Mirror Spacecraft Optics [From Ref. 2]

In December 2000, a proposal was submitted by NPS and AFRL to the National Reconnaissance Office under the Directors Innovation Initiative (DII) [Ref. 3]. The DII program allocates funds to perform research efforts with significant payoff potential for space-based reconnaissance. This contract was awarded to NPS and AFRL in January 2001.

As part of this DII effort, a series of experimental tests were used to demonstrate and validate the integration of the Bifocal Relay Mirror concepts. These experiments provide a test bed to apply the latest technologies to the problems of beam control and tracking. This test bed incorporates spacecraft attitude dynamics and control, onboard jitter reduction and beam control while tracking an uncooperative target. This will prove the latest technologies in this area and provide experimental data useful in constructing a ground-based, multi-body Bifocal Relay Mirror simulator.

2. Spacecraft Research and Design Center

The Spacecraft Research and Design Center (SRDC) at the Naval Postgraduate School consists of four laboratories and a reference library. One of these laboratories, the Spacecraft Attitude Dynamics and Control Laboratory, was the host to this experimental research. The Three Axis Satellite Simulator (TASS) was designed to be one of the focal research areas within the Spacecraft Attitude Dynamics and Control Laboratory. Its first intended payload was the AFRL designed bifocal relay mirror payload.

B. THREE-AXIS SATELLITE SIMULATOR (TASS)

1. Hardware

The TASS comprises a 4-foot in diameter octagonal table supported by a spherical air bearing. This table supports systems analogous to those found on any commercial spacecraft. The attitude control and determination system comprises three orthogonally mounted reaction wheels, three orthogonally mounted rate gyros, a three-axis magnetometer, a three-axis sun sensor, and a three-axis nitrogen thruster system. The command and data handling system comprises a Pentium II laptop computer that interfaces to the table hardware via two data acquisition cards. The table has a trim weighting system to allow for balancing, and several lead-acid batteries act as an onboard power supply.

2. Software

The control software was developed using the MATLAB/SIMULINK software package with Realtime Workshop (a MATLAB toolbox) providing interface capability with the TASS hardware. This interface was accomplished via two National Instruments

DAQcard-1200 PCMIA cards, together providing 16 analog input channels, 4 analog output channels, and 48 digital I/O channels.

3. Bifocal Relay Mirror Payload

The Bifocal Relay Mirror Payload (BRMP) consists of several components spread around the TASS. The optical train is mounted on an aluminum plate, and includes the fast steering mirror. A video camera, used for target tracking, is mounted coincident to the optical train. There are three electronics housings that include an RF signal demodulator, fast steering mirror controller, and a photodiode sensor decoder. Two commercial RF transmitter/receivers are used to transmit video signals to a desktop computer for image processing, and to receive beam steering instructions.

C. SCOPE OF THESIS

This thesis comprises the work involved in taking the TASS from initial delivery through full integrated testing with the Bifocal Relay Mirror Payload (BRMP). This process comprised several simultaneous areas of research, experimentation, and development.

Following the TASS delivery, the hardware/software interface required characterization, and the BRMP was integrated onto the TASS structure. The mass properties of the table required analysis and experimental validation, and calibration curves for the sun sensors were constructed. The power system required redesign to provide adequate capacity at several voltages, and the reaction wheel control system required a safety circuit to prevent damage. Several sensors proved to be noisy, requiring the development of signal processing algorithms to provide smooth data to the control laws. A PID controller was implemented, and direction cosine matrices were used to align the principal axes with the control axes. This development concluded with a successful test of the TASS and the BRMP. The lessons learned during this process were investigated as topics of future research and development.

II. HARDWARE DEVELOPMENT

The Three-Axis Satellite Simulator consists of several subsystems that act together to simulate satellite functions and attitude dynamics. This chapter outlines each subsystem in its function, physical location, and operation, as well as pointing out any modifications or outstanding deficiencies encountered during the development phase. Mass properties and reference frames are also discussed. Specifically, Section A discusses the general layout of the TASS, Section B covers coordinate systems related to the platform and control hardware, Section C covers the power system, Section D the reaction wheels, and Sections E through G discuss attitude determination sensors. Finally, Section H discusses the Bifocal Relay Mirror Payload (BRMP).

A. OVERVIEW

The TASS was constructed by Guidance Dynamics Corporation (GDC) and delivered to NPS in the early months of 2001 [Ref. 4, 5]. The base structure is an octagonal aluminum plate, .375" thick, supported by several aluminum stiffening bars on the bottom side. A ten-inch diameter spherical air bearing is rigidly attached to the underside in the center of the plate. This air bearing sits in an air-bearing cup, which provides a smooth surface for the bearing to rest in when air is not applied to the cup. When air is applied to the cup, it raises the table 3/8" to a free-floating position.

The TASS also has four balancing legs, four ballast weights, and a three axis fine balance weight system on the underside. The balancing legs are adjustable up and down for changing the center of mass in the vertical direction. Small weight rings that fit around these legs provide the capability for gross balance adjustment. The ballast weights offset the large mass of equipment on the top surface of the table. The fine balancing weights allow for minute adjustment of the center of mass in all three axes.

Subsystems on the table include three orthogonally mounted reaction wheels, three orthogonally mounted rate gyros, a three-axis sun sensor, a three-axis magnetometer, a laptop computer, three lead-acid batteries, and a thruster system of two

nitrogen propellant tanks and four thruster blocks providing three-axis control. Figure 6 outlines the locations of these components.

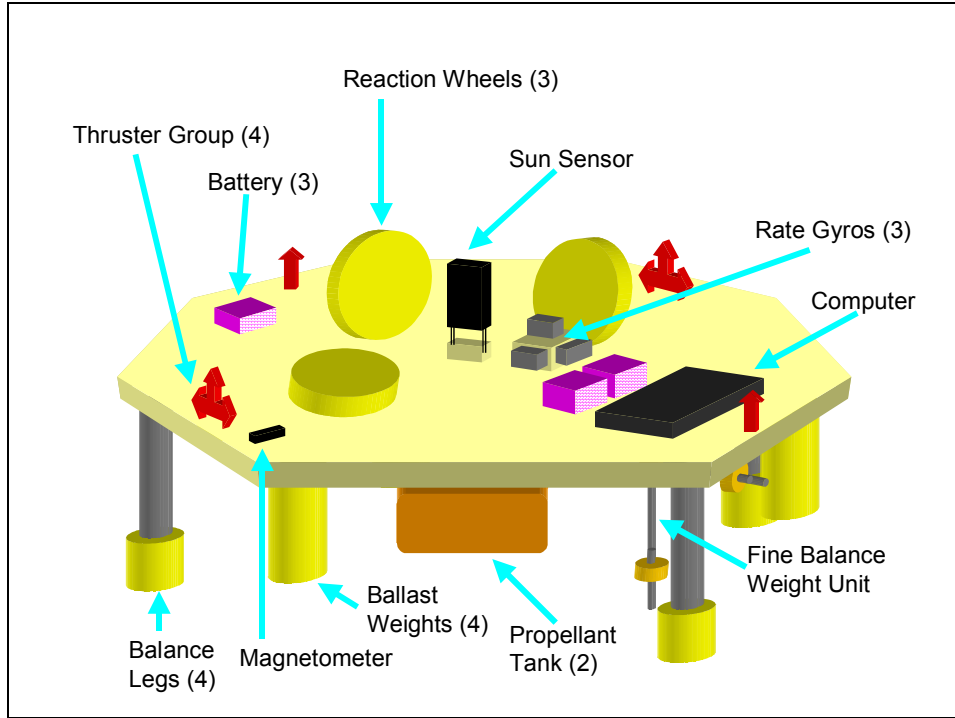


Figure 6. Subsystem Layout

The BRM payload consists of three electronics boxes for signal decoding, laser position determination, and fast steering mirror positioning. These boxes are mounted on an aluminum plate on the table surface above one of the propellant tanks. The optical train, which includes the fast steering mirror, is on a similar aluminum plate on the table surface above the other propulsion tank. A digital video camera is mounted alongside the optical train. The receiver, transmitter, and video power supply are located in available space along the edge of the table. (Figure 7)

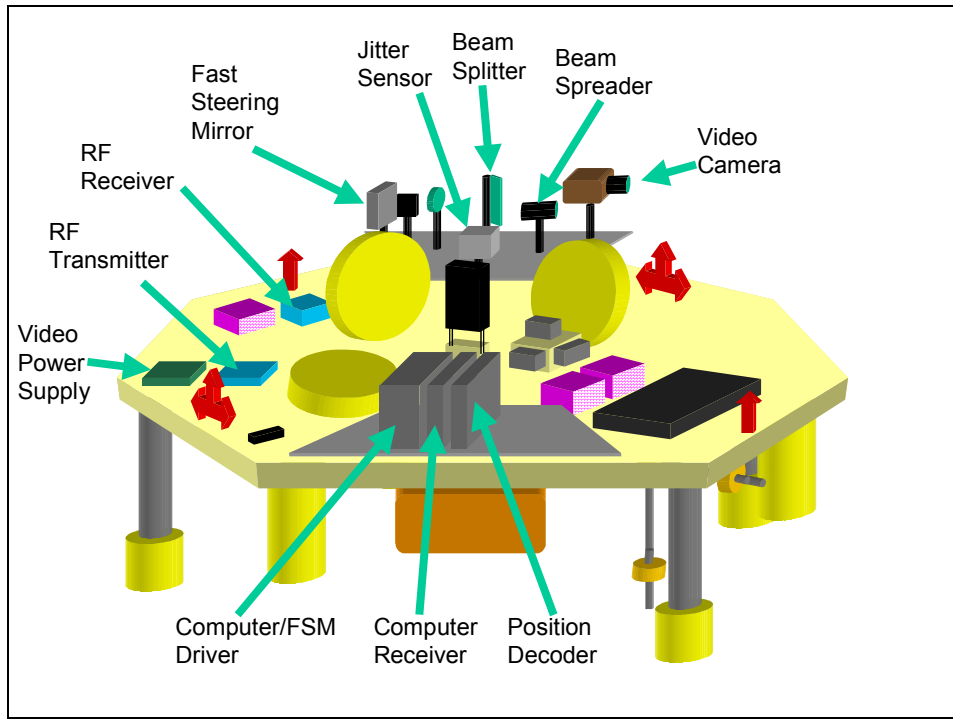


Figure 7. Bifocal Relay Mirror Payload Layout

Figures 8 and 9 are photographs of the TASS from above and below. They show the physical realities portrayed in Figures 6 and 7.

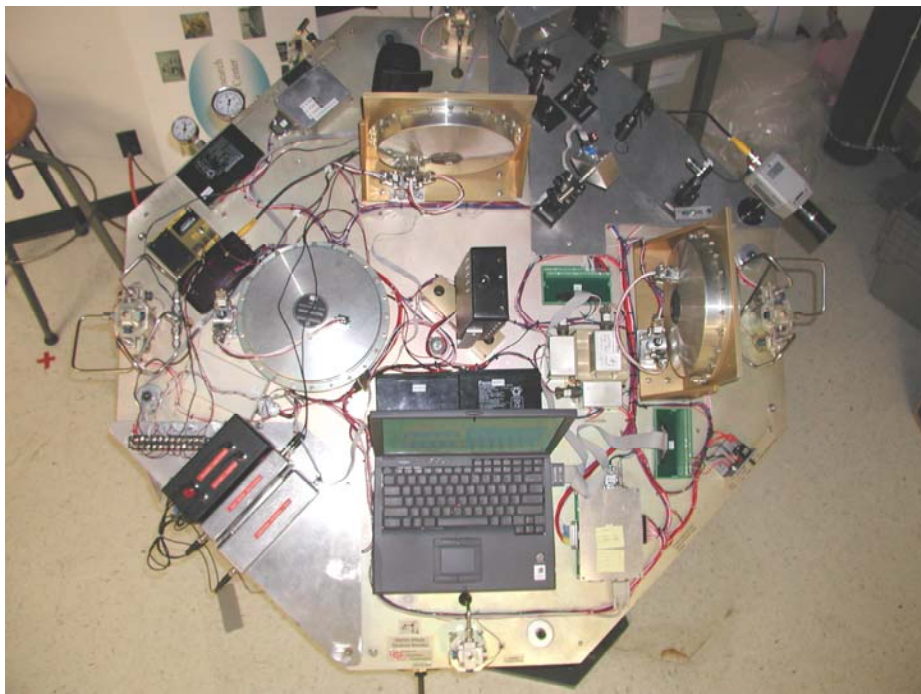


Figure 8. TASS Top View

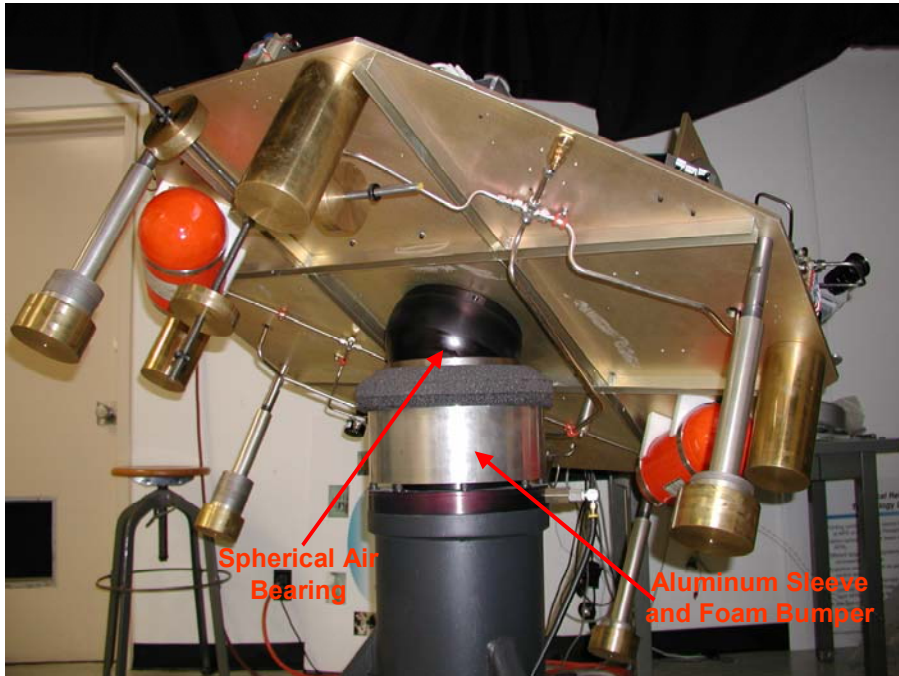


Figure 9. TASS Bottom View

A bumper system was provided by GDC to prevent the table from falling out of the air-bearing cup. This bumper is an aluminum cylindrical sleeve designed to fit around the air-bearing cup with an angled ring of foam around the top edge. When this ring is fully installed, it interferes with the airflow around the air bearing, and creates a small but noticeable effect on the TASS, making it extremely difficult if not impossible to balance or control the table. Due to this effect, and the extreme difficulty involved in tipping the TASS out of the air bearing, this bumper was unbolted and lowered to its current position (Figure 9).

B. REFERENCE FRAMES AND AXES

1. GDC Axes

The TASS was delivered with a labeled axis system and a control program designed to operate around these axes. The operation of this program about these axes was demonstrated at time of delivery, however this demonstrated control was focused around thruster-based control, with a lightly damped demonstration of reaction wheel control. The BRMP requires fine attitude control, and it was decided that a reaction-wheel based control law would be implemented to meet the payload requirements. Not

using the thrusters also eliminates the effect of mass loss due to propellant expulsion, and its subsequent effects on mass properties. The axis system chosen by GDC was a left-handed coordinate system. (Figure 10)

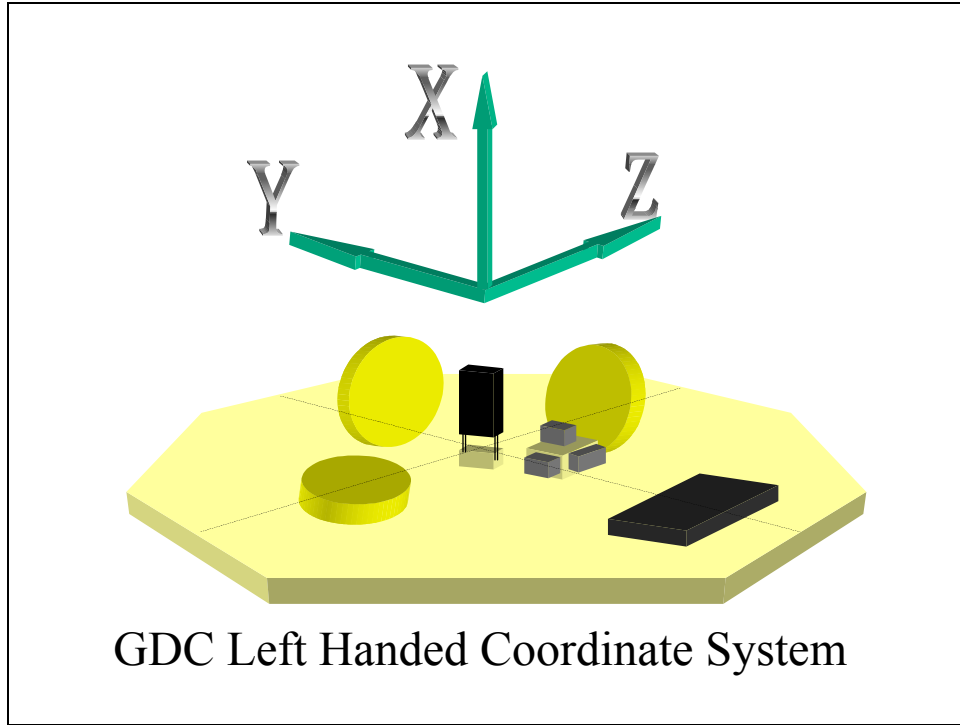


Figure 10. GDC Axis System

2. Control Axes

It is desirable to use a right-handed coordinate system for system operation, to align analysis and control law development with industry and educational standards. In order to facilitate the logical development of a right-handed coordinate system for the TASS, an analysis of the existing sensor outputs and command inputs was undertaken.

Sensor inputs to the computer are via two National Instruments DAQcard-1200 PCMIA cards (DAQcard(s)) at memory locations 1000h and 1200h. Each card contains eight $\pm 5V$ analog inputs, two $\pm 5V$ analog outputs, and 24 digital I/O ports. Figures 11 and 12 identify the DAQcard channels related to the rate gyros and sun sensor respectively. The orthogonal axis systems indicate the positive coordinate frame measured by the sensor as the table is rotated in the indicated direction. Figure 11 also illustrates the axes formed by the three rate gyros when the table is rotated to provide positive outputs from each gyro.

Figure 12 indicates the sun and star positioned over the TASS for attitude determination. Both lights are hung from the ceiling five feet above the TASS, connected to a rigid aluminum bar. Both lights are the same wattage. In the Figure, the larger star is located directly above the sun sensor and is used for roll and pitch determination. The second bulb is placed along the width axis of the sun sensor, determining the zero position of the yaw axis.

Figure 13 indicates the direction the TASS will move if a positive voltage is applied to the control input of each reaction wheel.

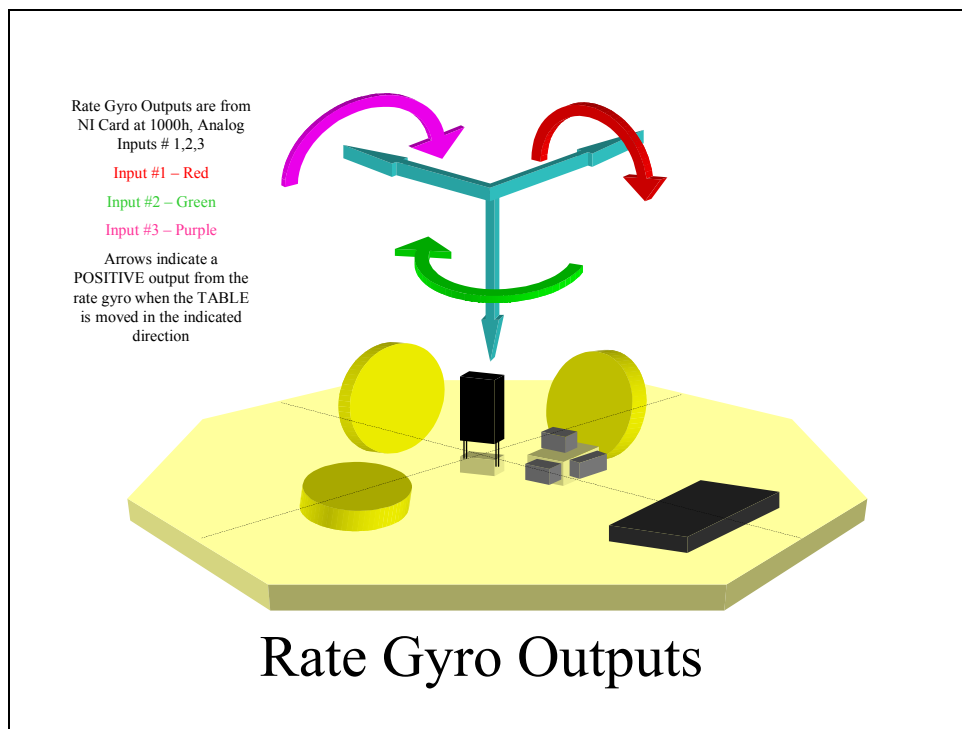


Figure 11. Rate gyro dynamic outputs

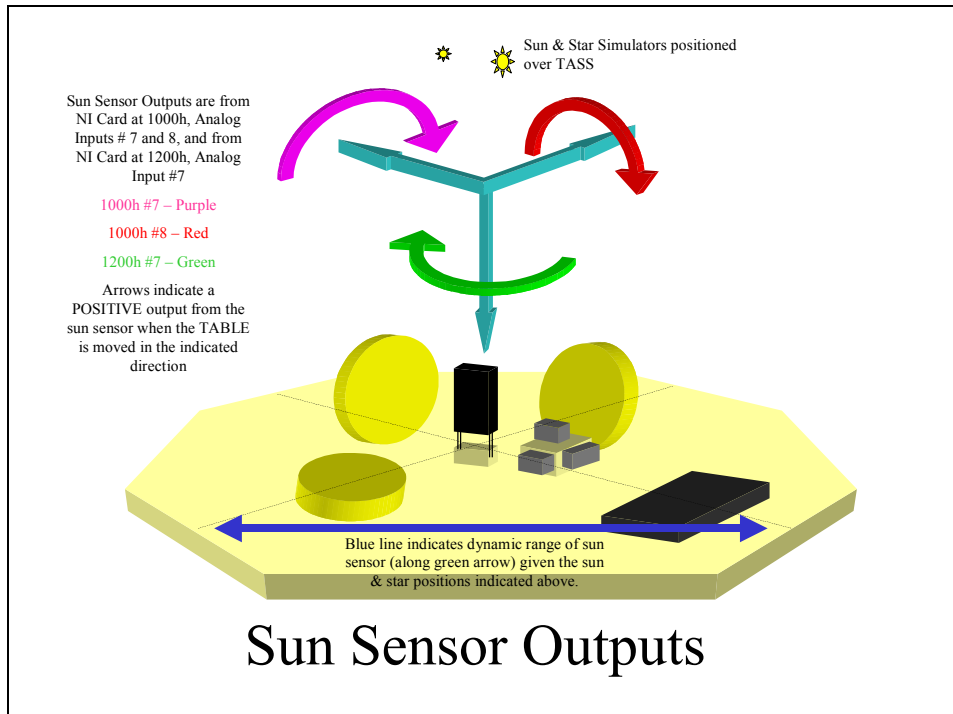


Figure 12. Sun Sensor Dynamic Outputs

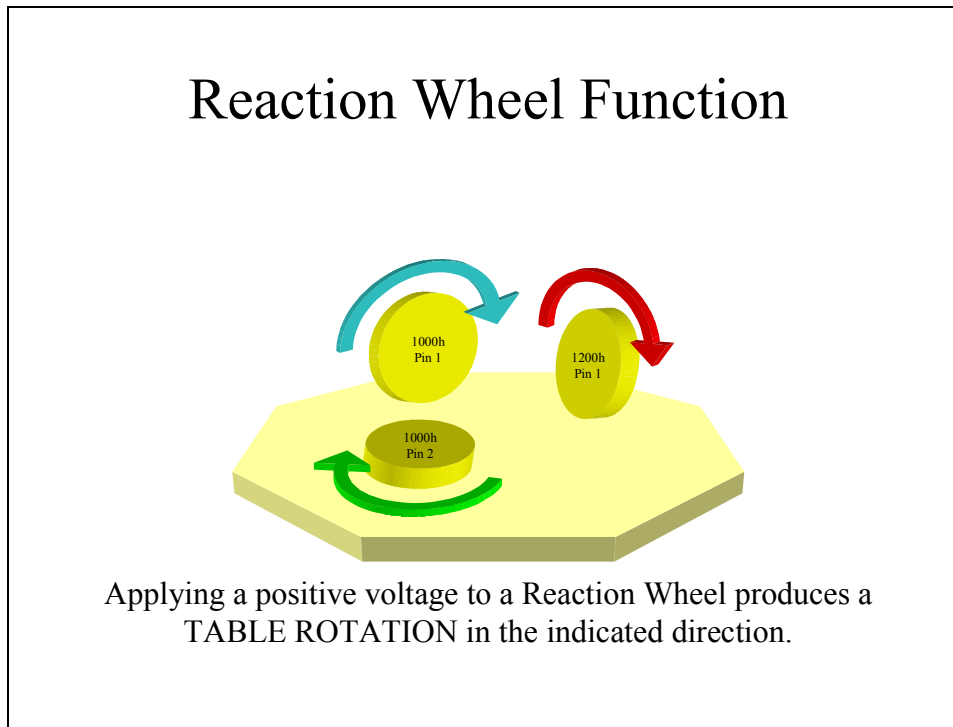


Figure 13. Reaction Wheel Control Output

Based on the directions associated with positive sensor outputs, a right-handed control axis system was created and adopted as the standard system for all future table development (Figure 14). This axis system is referred to as the ‘Control Axes’, and a subscript of ‘C’ denotes this axis (X_C , Y_C , Z_C).

The use of roll, pitch, and yaw are frequently associated with the attitude control of spacecraft and aircraft. For the purposes of the TASS it is useful to think of the user ‘flying’ the simulator from the location of the computer. Using this as a reference, roll is associated with motion about the Z_C axis, pitch is associated with motion about the X_C axis, and yaw is associated with motion about the Y_C axis.

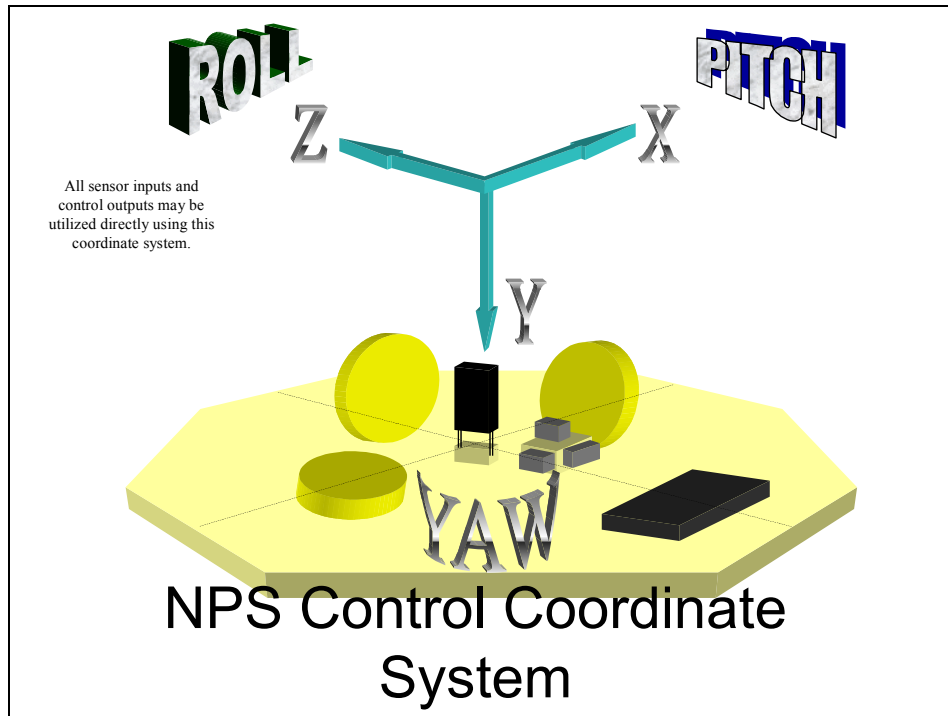


Figure 14. Control Coordinate System

3. Principal Axes

The TASS was originally constructed to have its principal axes coincident with the GDC axes. However the addition of ballasting weights, the bifocal relay mirror payload, and shifting the sun sensor location had the effect of changing the principal axes of the TASS. Any reference to the principal axis frame will be subscripted with a P (X_P ,

Y_P , Z_P). The determination of the principal axes will be discussed in the Mass Properties section (Section I).

4. Mass Properties Axes

Mass properties of the TASS were calculated using a right-handed coordinate system based at the center of rotation (and thus the desired center of mass) that is roughly 3 inches below the table surface. The XY plane is parallel to the surface of the table, with the X-axis pointing towards the laptop computer, the Z-axis perpendicular to the table surface pointing towards the ceiling, and the Y-axis forming a right-handed system as shown in Figure 15. Any reference to the mass properties frame will be subscripted with an M (X_M , Y_M , Z_M).

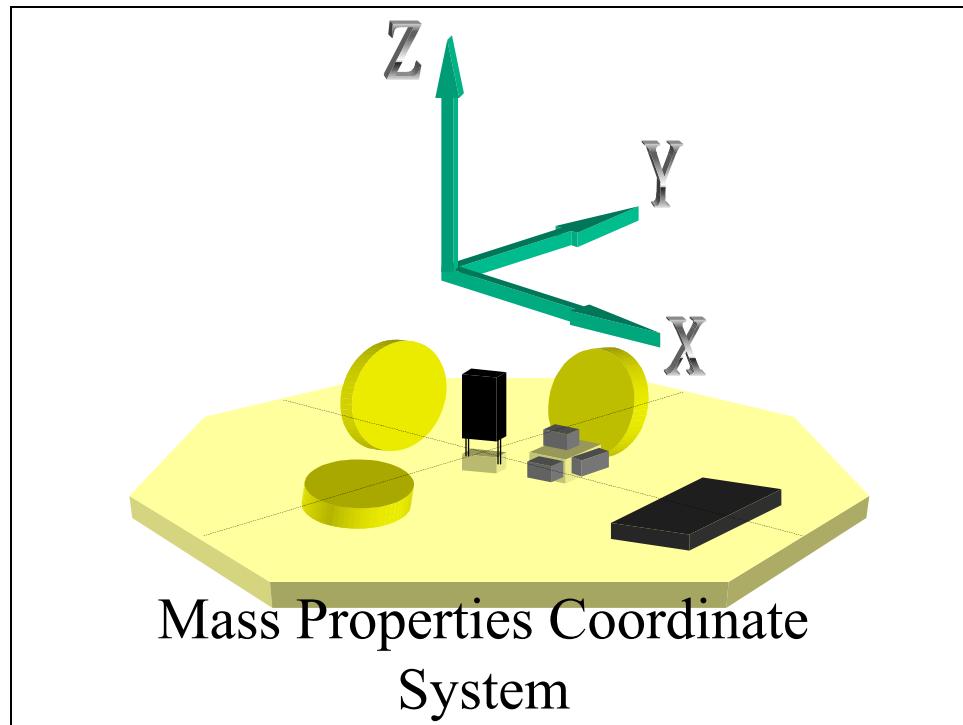


Figure 15. Mass Properties Coordinate System

C. POWER SYSTEM

Power is supplied to the TASS components at two voltages, 18VDC and 28VDC. The reaction wheels require 18VDC, while 28VDC powers all other TASS subsystems. This power is stored in three lead-acid batteries, two 12V at 7.2 Ah, and one 6V at 7.2 Ah. These batteries are connected in series, in a 12-6-12 sequence (Figure 16).

Original TASS Power System

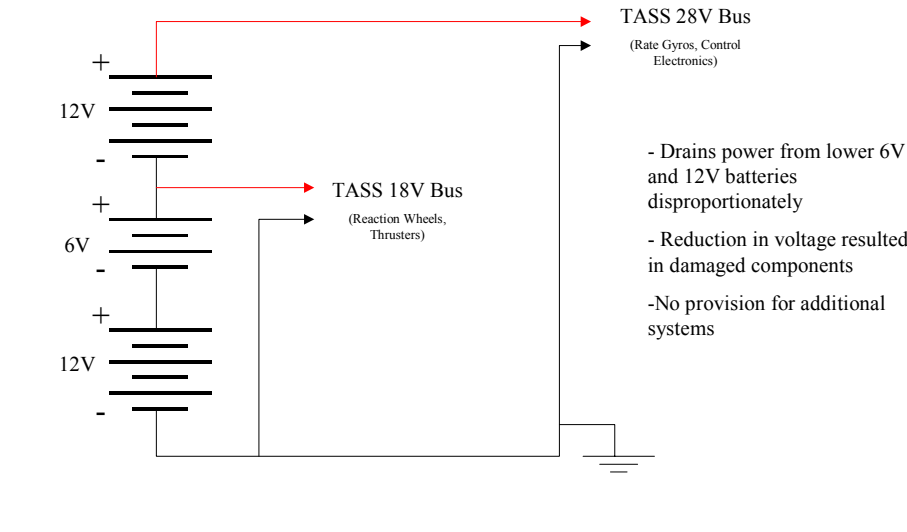


Figure 16. TASS Power System as Originally Designed

1. Original Power System Design

There are several problems with this power system as designed. First, the system draws power disproportionately from two of the three batteries (the two providing 18V to the reaction wheels.) Secondly, the system voltage is unregulated. As the lead-acid batteries discharge, their output voltages decrease thereby decreasing the total bus voltage. This reduced voltage can lead to excessively high currents, damaging system components (This is extensively discussed in the reaction wheel section).

Lastly, there are several issues with the capacities of the batteries. The overall system capacity is not sufficient to conduct full operations for more than 30 minutes if reaction wheel usage is limited. This is not enough time to conduct meaningful testing, given the 12-18 hour battery recharge time.

The incorporation of the bifocal relay mirror payload added a level of complexity to the power requirements. The bifocal relay mirror payload requires $\pm 12\text{VDC}$ for the fast steering mirror and supporting computer hardware, and $+12\text{VDC}$ for the video camera and two RF transceivers.

- Drains power from lower 6V and 12V batteries disproportionately
- Reduction in voltage resulted in damaged components
- No provision for additional systems

2. Battery Voltage and Capacity

The solution to the first two battery issues, disproportionate battery drainage and an unregulated supply voltage, can only be corrected by redesigning the power system. The third problem, that of limited capacity, can be dealt with by replacing the batteries.

A two-phase upgrade plan was developed to meet these three issues. Phase one included a power analysis of TASS load (Appendix F) and a survey of available space on the table surface. Based on these results, it was decided to replace the two 12V 7.2 Ah cells and the 6V 7.2 Ah cell with cells of higher capacity. Two Hawker Genesis batteries at 12V 26 Ah and a Cyclon 3-BC 6V 25 Ah cell would be mounted on the table. This replacement would allow for longer test periods.

Phase two involves the redesign of the TASS power system to provide a robust, stable power source for all system loads. This is accomplished via a large, conduction cooled DC-DC converter produced by Vicor. This converter delivers 300W of power at 18VDC to drive the reaction wheels, and 200W of power at 28VDC to provide power for the rest of the TASS components. The DC-DC converter provides stable output voltage over a wide range of input voltages at greater than 80% efficiency.

The batteries driving this DC-DC converter are four Hawker Genesis EP batteries at 12V, 26Ah apiece. These batteries are connected in series to provide a 48V potential. The schematic for the Phase two power system is shown in Figure 17. Although equipment has been ordered to implement Phase one and two, neither upgrade has been completed.

Phase 2 Power System Design

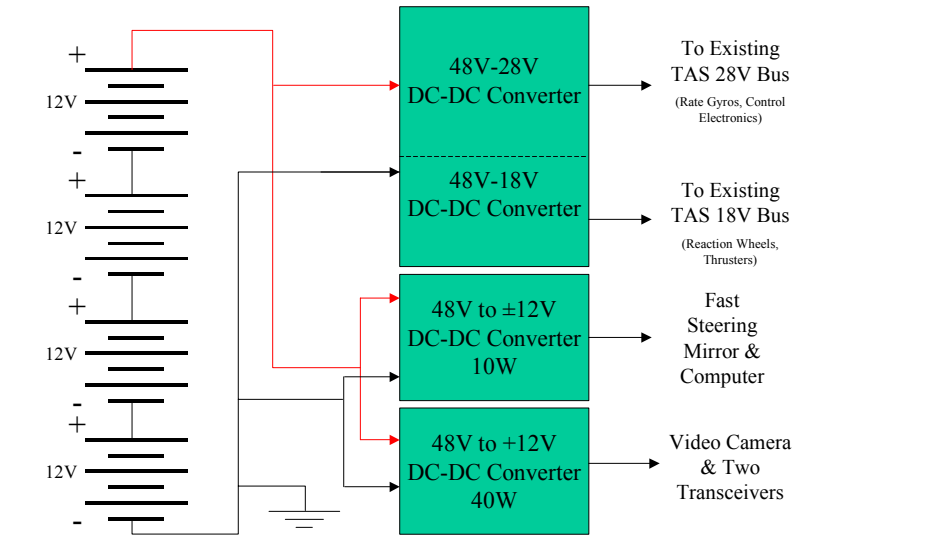


Figure 17. Re-design of TASS power system

3. Video-Capable Power System Modification

Incorporating the bifocal relay mirror payload required the addition of a video power supply unit. Based on the power analysis conducted (Appendix F), the $\pm 12\text{VDC}$ loads require 4.8 Watts, and the $+12\text{VDC}$ loads require 10.8 Watts. Two DC-DC converters were chosen for this task, one converter producing $\pm 12\text{VDC}$ with a maximum power output of 10 Watts, the other producing $+12\text{VDC}$ with a maximum power output of 40 Watts (Figures 18 & 19). These converters were chosen to provide additional capacity for future TASS upgrades, and are designed to accept a wide range of input voltages (18-72V) to allow operation after the Phase 2 power system upgrade is implemented.

Video Power Upgrade

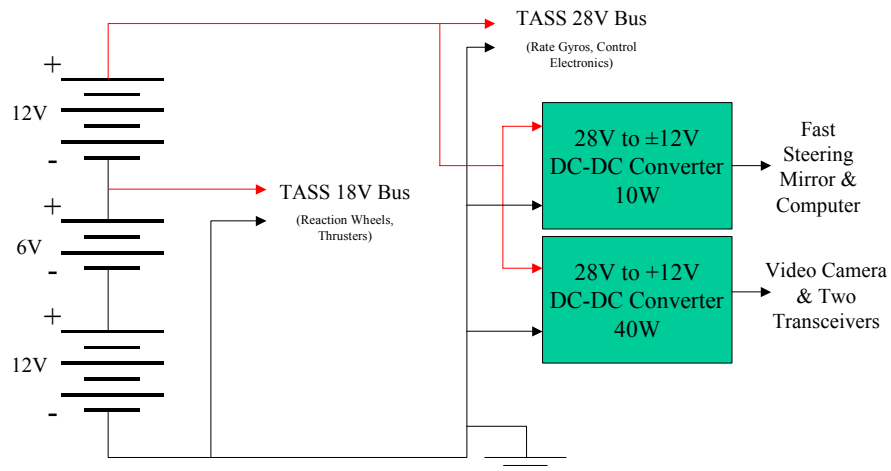


Figure 18. BRMP Power Upgrade

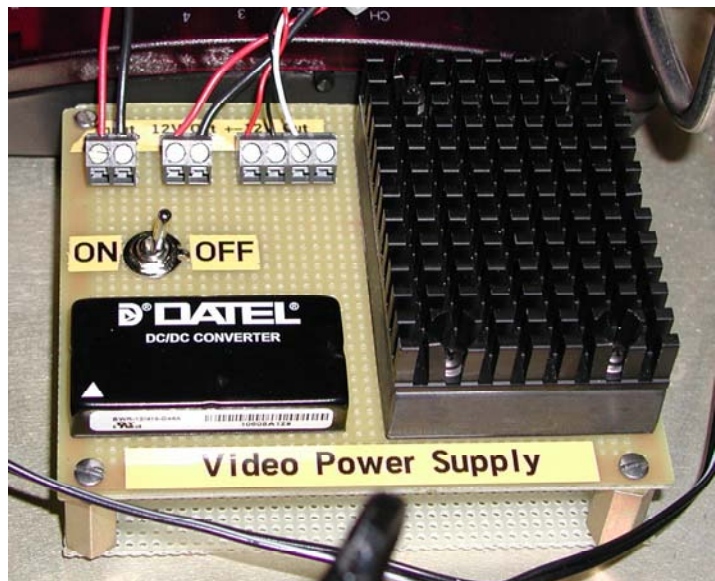


Figure 19. Video Power Supply Hardware

Following the failure of a reaction wheel due to low battery voltage, a lead was connected from the battery to an analog input on one of the DAQcards, providing a means of monitoring battery voltage during testing (Table 1). The signal provided to the

DAQcard is one-tenth of the actual battery voltage due to voltage limitations ($\pm 5V$) on the DAQcard.

Analog Outputs from Power System		
Signal Description	Signal Location	Notes
Battery Bus Voltage	1200h Pin 8	Signal is Voltage/10

Table 1. Power System Signal Summary

D. REACTION WHEELS

The TASS has three Ball Aerospace 20.3 Nms reaction wheels mounted on the top surface in a mutually orthogonal configuration. These reaction wheels provide primary fine pointing attitude control capability to the TASS and are shown in Figure 20.



Figure 20. Reaction Wheel Location

1. Reaction Wheel Commanding and Overspeed

The reaction wheels are powered from an 18VDC power supply, with each wheel being commanded via a ± 2 VDC command signal, indicating direction and magnitude of the desired change in wheel rotation. The command signal is a rate command, meaning

that, for example, a 1V command signal will cause the wheel to continuously accelerate at half (1V/2V) its rated acceleration.

The reaction wheels are rated to a maximum speed of 2500 rpm in either direction, making speed control a vital concern in order not to cause damage to the wheels. Each reaction wheel has three Hall sensor outputs, which provide a TTL signal that can be decoded to provide wheel speed and direction. In order to prevent a wheel overspeed situation, GDC designed a proprietary box that utilizes two of these three Hall signals to determine wheel speed only (Figure 21). If wheel speed exceeds 2000 rpm, a warning light associated with that particular wheel flashes, warning the user of the situation. If the speed exceeds 2200 rpm the flashing light will turn solid, and the wheel command signal will be disabled until the speed falls below 2200 rpm. This speed signal is also transmitted to the laptop computer. The reaction wheel interface signals are given in Table 2.

Overspeed Control Box



Figure 21. Overspeed Control Box

Analog Outputs from Reaction Wheels		
<u>Signal Description</u>	<u>Signal Location</u>	<u>Notes</u>
X _C Reaction Wheel Speed	1200h Pin 3	
Y _C Reaction Wheel Speed	1200h Pin 1	
Z _C Reaction Wheel Speed	1200h Pin 2	
X _C Reaction Wheel Torque Feedback	1200h Pin 6	
Y _C Reaction Wheel Torque Feedback	1200h Pin 4	
Z _C Reaction Wheel Torque Feedback	1200h Pin 5	
Analog Inputs to Reaction Wheels		
<u>Signal Description</u>	<u>Signal Location</u>	<u>Notes</u>
X _C Command Signal	1200h Pin 1	Limit to ± 2 VDC
Y _C Command Signal	1000h Pin 2	Limit to ± 2 VDC
Z _C Command Signal	1000h Pin 1	Limit to ± 2 VDC

Table 2. Reaction Wheel Signal Summary

2. Failure and Troubleshooting Reaction Wheel #012

During initial control law testing in April 2001 a grinding, clicking noise was heard emanating from Reaction Wheel S/N 012 (Z_C axis). Subsequent to this noise the wheel failed to respond to commands. Ball Aerospace was contacted for troubleshooting assistance, and it was determined that the fault lay in the wheel itself, not the control wiring leading to it. The wheel was returned to Ball Aerospace for further troubleshooting and refurbishment.

The initial working theory for the failure was as follows: As a reaction wheel is accelerated, electrical power is transferred from the battery into kinetic energy in the wheel. When the wheel is subsequently decelerated, this kinetic energy is transferred

back to electrical energy. The assumption made by GDC was that the batteries would be able to absorb this energy generated by a wheel decelerating at the maximum rate. The initial failure theory was that the battery had been unable to accept this electrical energy, leading to a momentary increase in bus voltage and damage to the wheel circuitry.

However, testing by Ball Aerospace proved that it was not high voltage, but low voltage that caused the failure of the wheel. The problem occurred near the end of a testing session, when battery voltage (for which there was no means of monitoring at the time) was very low. Given the basic electrical equation:

$$\text{Power} = \text{Voltage} \times \text{Current}$$

If a $\pm 2\text{V}$ signal was commanded of a wheel, the wheel would attempt to draw the requisite power to accomplish the task. Since voltage was low, the current would be much higher. It was this high current that damaged the FETs inside the reaction wheel rendering it inoperative.

3. Voltage/Current Clamp Development

Several changes to the table design came about because of this failure. Most importantly, a circuit was designed to protect the wheels from damage during operation. The circuit serves as protection against both high current (via a 5A quick-blow fuse) and high voltage (via a Darlington voltage clamp circuit.) This circuit and its accompanying hardware are outlined in Appendix C.

The completed voltage clamps were mounted next to each reaction wheel and the existing wiring harness was plugged into the voltage clamp. A short length of cable was manufactured to connect the voltage clamp to the reaction wheel. The system was successfully bench tested prior to installation, and then operationally proven on two occasions when the 18V nominal supply to the reaction wheels dropped to near 13 V. On these two instances, the protective 5A fuses blew, protecting the reaction wheel from a high current condition.

Operational constraints were also added for the protection of the wheels. By monitoring bus voltage during wheel operation, the low voltage condition that leads to wheel damage can be avoided by not allowing table bus voltage to drop below 25V. This was enabled by placing a lead carrying the main battery bus voltage (voltage/10 to meet

the DAQ-card operational limits) into an open analog input port on the National Instruments DAQ-1200 cards. This allows for real-time monitoring of voltage while the TASS is running.

E. RATE GYROS

The TASS has three Humphrey rate gyros mounted on the top surface in a mutually orthogonal configuration. These rate gyros provide rate data to the TASS. The signals to the laptop are summarized in Table 3.

Analog Outputs from Rate Gyros		
<u>Signal Description</u>	<u>Signal Location</u>	<u>Notes</u>
X _C Rate	1000h Pin 1	Noisy signal ($\pm 0.01V$)
Y _C Rate	1000h Pin 2	Noisy signal ($\pm 0.01V$)
Z _C Rate	1000h Pin 3	Noisy signal ($\pm 0.01V$)

Table 3. Rate Gyro Signal Summary

The output signals of these rate gyros are noisy compared to the signal generated at the low angular rates experienced by the table during normal operation. Additionally the gyros have a significant bias, and this bias is not constant from day to day. These factors led to the implementation of two filters in order to provide accurate data. This signal processing is detailed in Chapter III.

F. SUN SENSORS

1. Original Sun Sensor Design

The TASS initially had a two-axis sun sensor mounted to the left-hand side of the laptop computer on the table top. During subsequent testing, it was determined insufficient data existed to stabilize the TASS using only sun sensor and rate gyro data alone. Some initial success was made using the magnetometer to provide a third axis of position information, but it was deemed insufficient given the precise pointing accuracy required by the relay mirror payload.

2. Three-Axis Sun Sensor Modification

The sun sensor was then removed and modified by GDC to incorporate a third axis of information. The sun sensor was re-mounted in the center of the table facing the ceiling. A 12 foot blackout canopy was built 5 feet above the table, and two lights roughly one foot apart were placed in the center of this canopy to simulate the sun and a single star. The sun sensor used one of these lights to provide roll and pitch position information, and the position of the second light relative to the first light to provide yaw information. The exact algorithms by which these calculations are performed are proprietary to GDC and not provided to NPS.

The dynamic range of the yaw axis is shown in Figure 22. The ‘main’ bulb is placed directly over the sun sensor, and is used to determine the pitch and roll of the table. The second bulb is placed along the wide dimension of the sun sensor, and determines the zero point of the yaw axis.

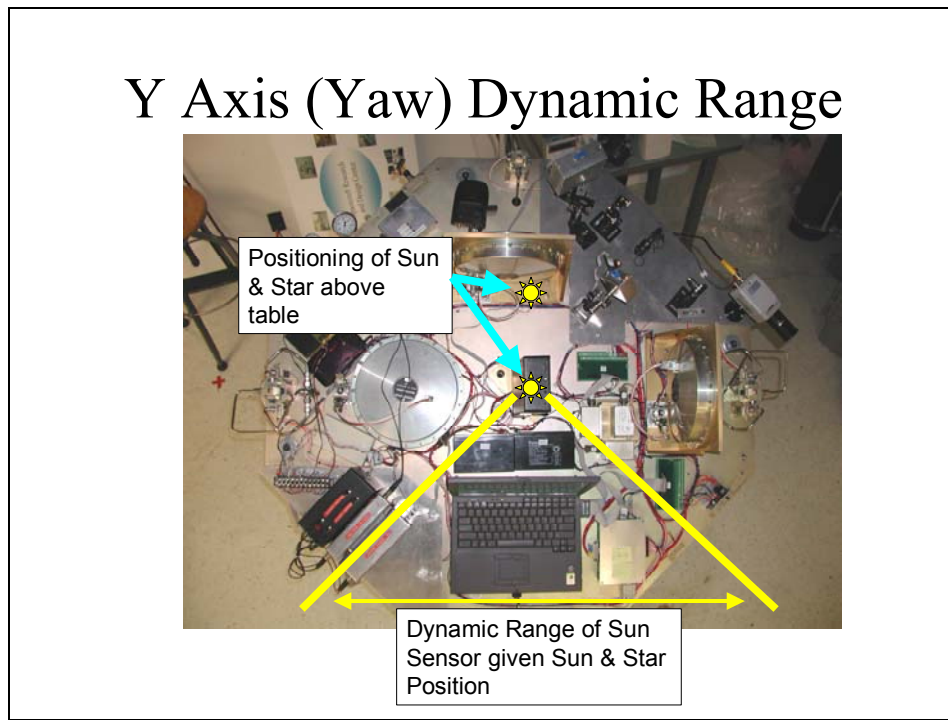


Figure 22. Sun Sensor Y-Axis Dynamic Range

3. Angular Calibration of Sun Sensor

The outputs of the sun sensor are a linear signal from -5 volts to $+5$ volts directly proportional to the angular displacement. Once this new sensor was installed, the slope

and intercept of the linear equation describing angular position were determined in order to transform the voltage signal to an angular measurement in degrees.

For the X_C and Z_C -axes this was accomplished by fixing a laser on the table perpendicular the axis to be measured. The table was floated and leveled using a bubble level, and the laser beam position was marked on the wall next to the TASS. This served as the ‘zero’ position for the axis. Measurements were marked on the wall in inches above and below this zero position (typically in 2 or 5 inch increments), and the distance from the center of rotation to the wall was measured. The table was then rotated so as to put the laser beam on each of the marks on the wall and the corresponding voltage recorded.

Once this data was collected for the X and Z axes the angles to each mark on the wall were calculated using trigonometric equations, and the voltage data fit to the angular data using a short Matlab routine. (Appendix C)

A similar process was used to measure angular data for the Y axis, but it was a bit more involved. The Y_C axis of the sun sensor, as previously stated, uses the position of the two ceiling lights relative to each other to determine the table’s position. This algorithm only operates over roughly a 90 degree arc, beyond which angular readings from the Y axis sun sensor become meaningless.

In order to determine voltage readings over the range of the sensor, the TASS was first floated on the air bearing and rotated until the sun sensor reached an output limit ($\pm 5V$). A laser was then secured to the table surface perpendicular to the edge of the table and on an imaginary line between the center of table rotation and perpendicular to the wall. The point where the laser appeared on the wall was marked, and a voltage reading taken. This process was repeated while rotating the table until we reached the other limit of the sensor. Following this data collection, the distance was measured between the center of table rotation and each wall, and the distance between points on the walls in order to construct triangles and determine the represented angles.

A program was written in Matlab to find the function to describe the relationship between voltage and angle. As expected, a linear relationship best describes the output of the sun sensor in each axis. These relationships are shown below, with actual data points

shown as blue circles, and the green line being the best fit curve. Two graphs are shown for the Y-axis, one for representing the Y-axis from 0 to 90 degrees, and the other for representing the Y axis from -45 to 45 degrees. (Figures 23, 24, 25, and 26)

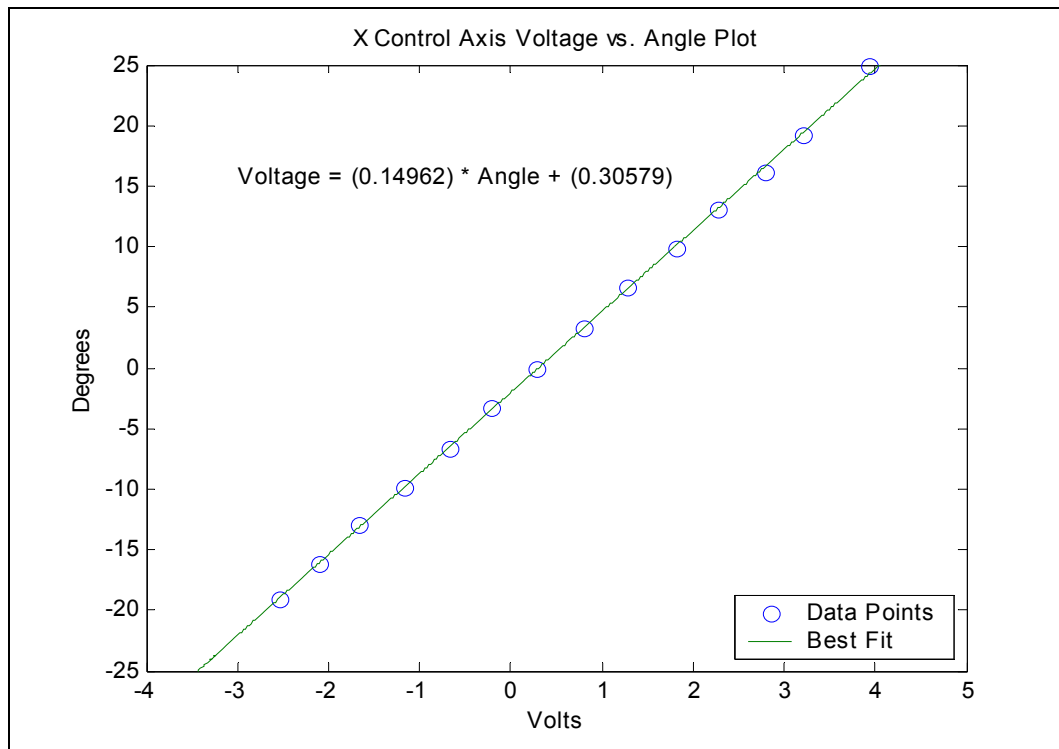


Figure 23. X_C Axis Sun Sensor Voltage vs. Angle

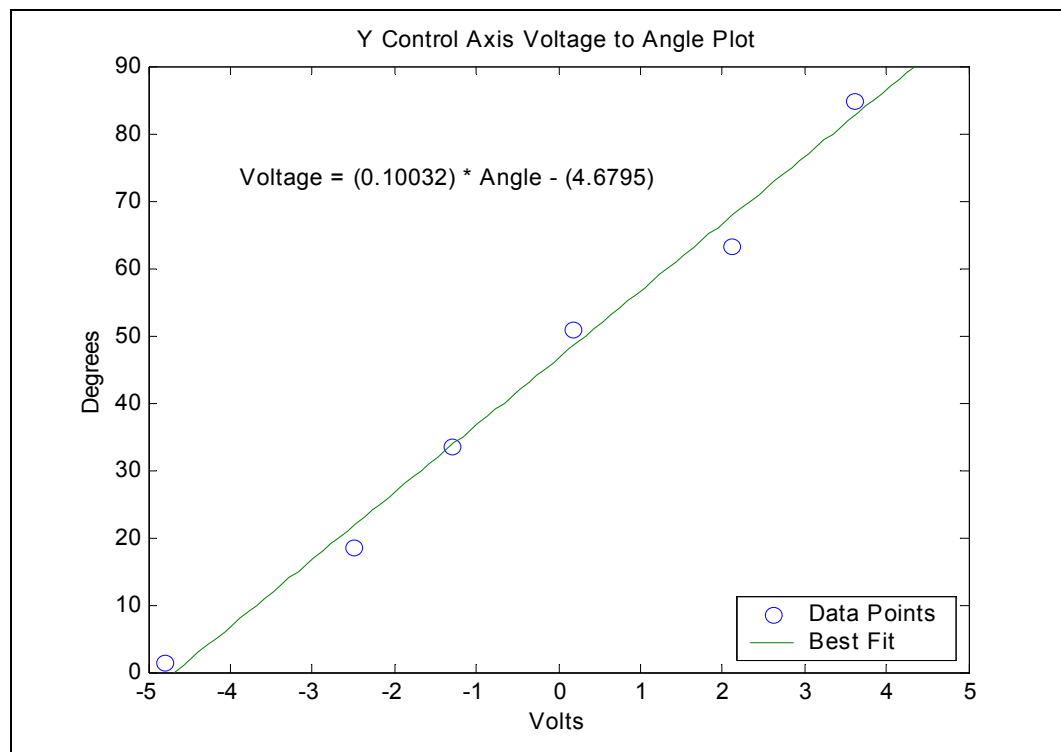


Figure 24. Y_C Axis Sun Sensor Voltage vs. Angle, 0 to 90 degrees scale

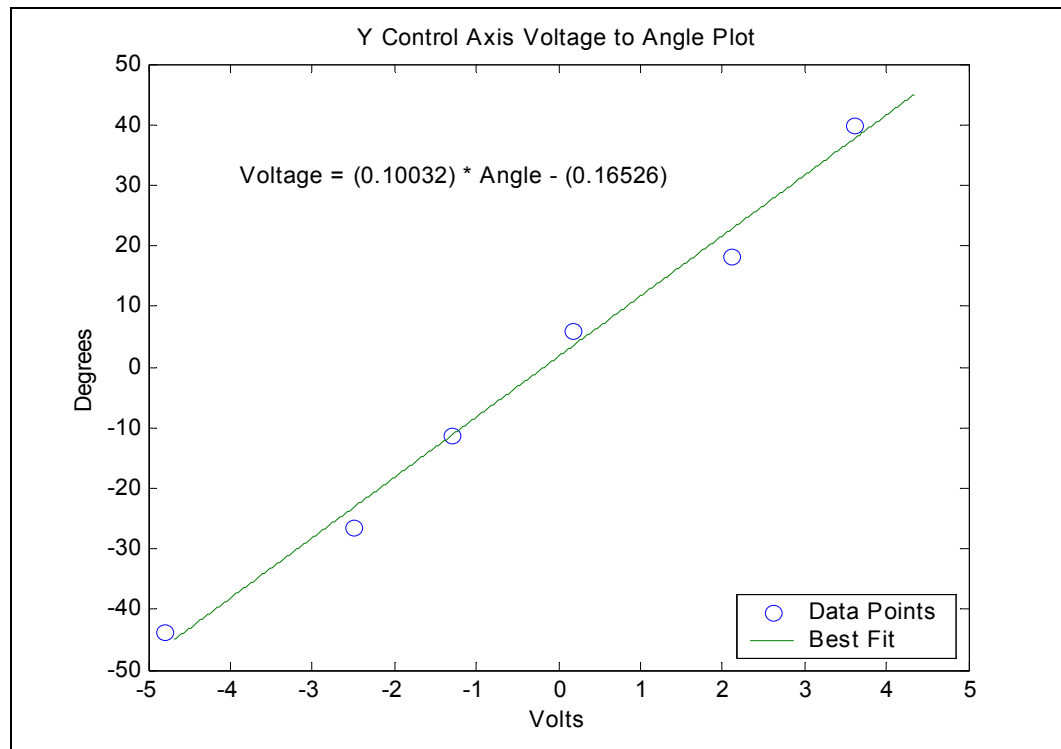


Figure 25. Y_C Axis Sun Sensor Voltage vs. Angle, -45 to 45 degrees scale

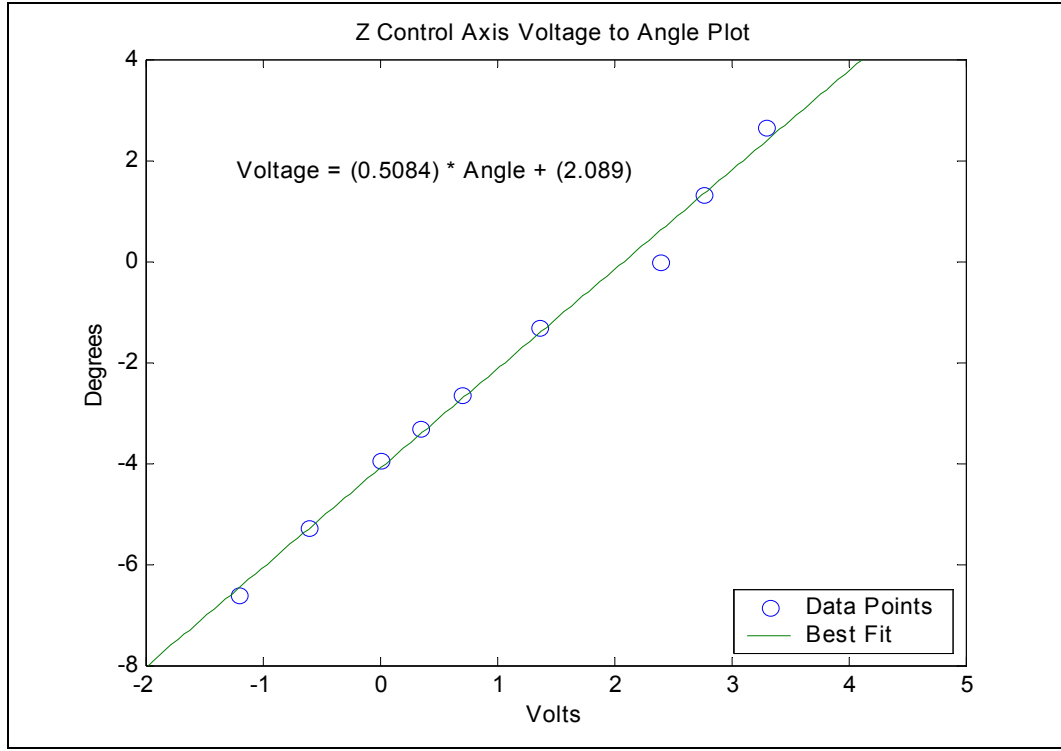


Figure 26. Z_C Axis Sun Sensor Voltage vs. Angle

The data points at the limits in each axis represent the maximum achievable output in that axis, and are therefore indicative of the maximum field of view (FOV) in each axis. It can be seen that the X_C axis has a FOV of 44° , Y_C of 82° , and Z_C of 9° . The X_C and Y_C axes are roughly centered on zero, while the Z_C axis is significantly offset from the zero position. This is due to the physical positioning of the sun sensor on the table. Table 4 summarizes the sun sensor data, and Figure 27 shows the X_C and Z_C fields of view with respect to the sun sensor.

Analog Outputs from Sun Sensor		
<u>Signal Description</u>	<u>Signal Location</u>	<u>Notes</u>
X_C Position	1000h Pin 8	FOV $+25^\circ$ to -19°
Y_C Position	1200h Pin 7	FOV $\pm 45^\circ$
Z_C Position	1000h Pin 7	FOV $+2^\circ$ to -7°

Table 4. Sun Sensor Signal Summary

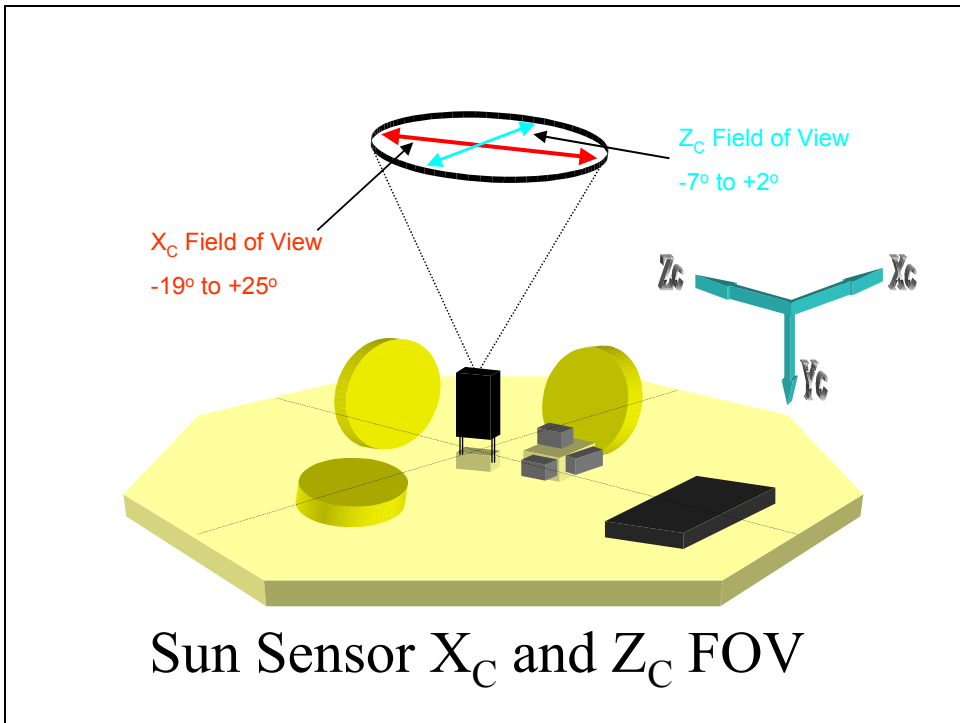


Figure 27. Sun Sensor X_C and Z_C Fields of View

G. MAGNETOMETER

A Humphrey three-axis magnetometer is mounted on the top surface of the table at a 45-degree angle offset about the Y_C axis. The alignment of the magnetometer with any axis system was not taken into consideration at time of construction, and no attempt to change the position has been undertaken since the magnetometer is not currently being used. If its use were desired in the future, a coordinate transformation would be needed to align it with the control axis system. The signal descriptions in Table 5 have no coordinate system associated with them as a result.

Analog Outputs from Magnetometer		
<u>Signal Description</u>	<u>Signal Location</u>	<u>Notes</u>
X Position	1000h Pin 4	DCM required for use
Y Position	1000h Pin 5	DCM required for use
Z Position	1000h Pin 6	DCM required for use

Table 5. Magnetometer Signal Summary

H. VIDEO SYSTEM

The BRMP was developed and tested independently in Albuquerque, New Mexico by Air Force Research Laboratory. This hardware consists of three electronics boxes for signal reception, beam position decoding, and the fast steering mirror (FSM) controller. A picture of the electronics hardware is contained in Figure 28.



Figure 28. AFRL Electronics Hardware

The operational concept of the BRMP is outlined in Figure 29. A red bench-top laser is aimed at the payload, which directs the laser at the FSM and then through a beam spreader to the target on a wall in the lab. Onboard the platform, the laser beam passes through a splitter, and high-frequency jitter is sensed and removed with a closed loop controller to the FSM. The video camera sends an image of the target to the control computer (located off the floating platform), which processes the image and sends fast steering mirror commands back to the floating platform to drive the red laser beam towards the green laser target.

BRMP Operational Concept

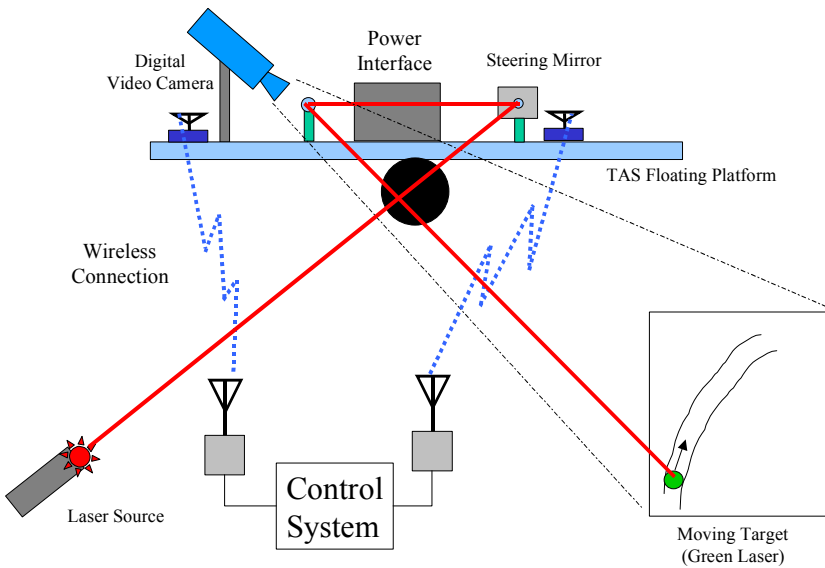


Figure 29. BRMP Operational Concept

The optical train consists of a primary mirror, the FSM, a lens, a variable beam splitter, a jitter sensor, and a beam spreader. A video camera is mounted adjacent to the optical train to provide feedback for beam targeting and steering. A diagram of the optical train is contained in Figure 30. The beam spreader is an inverted microscope lens, amplifying small motions of the FSM into larger motions on the target (A map of the world, hung on a wall ten feet away).

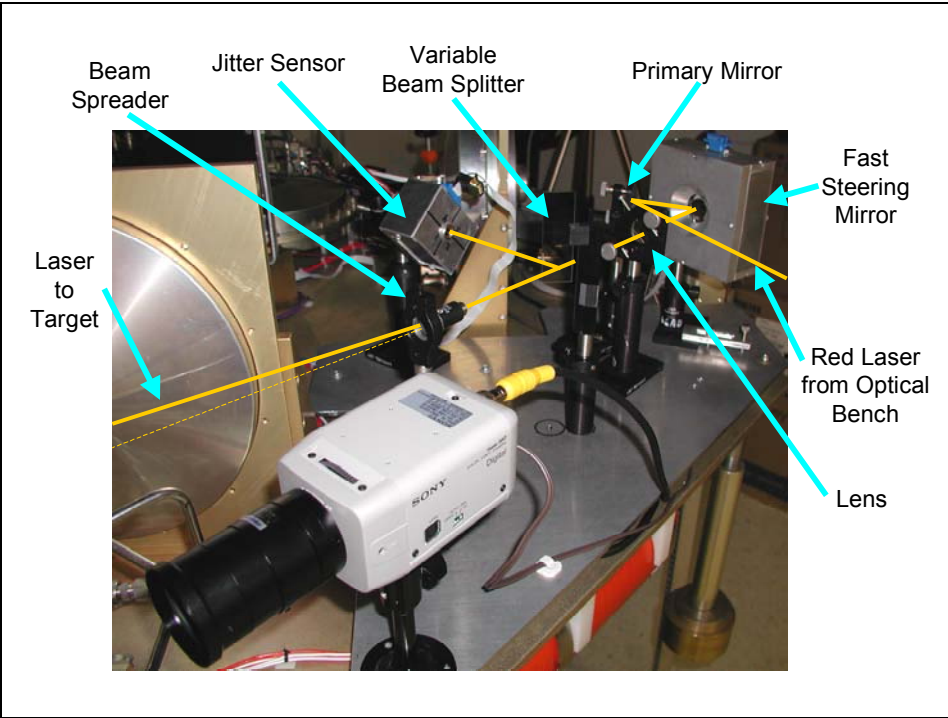


Figure 30. Optical Train Diagram

A radio frequency (RF) transmitter/receiver transmits the video camera signals to a desktop computer for image processing, and another transmitter/receiver receives commands from the desktop computer to drive the FSM.

Integrating the BRMP onto the TASS presented some challenges. Besides the obvious changes in the mass properties of the table, providing power to the BRMP was a major issue. During the design process, it was thought that power could be brought to BRMP components by way of a lightweight umbilical. However, subsequent testing indicated that even the smallest disturbance in the mass characteristics of the table had a serious impact on its operation. This ruled out any sort of umbilical during table operation.

A power requirements analysis of AFRL components was conducted, and is outlined in Appendix F. The analysis determined that 10.8 Watts were required at 12VDC, and 4.8 Watts were required at ± 12 VDC. Based on these requirements, two DC-DC converters were chosen, and a video power supply was built and installed on the table (Figure 31). The schematic of this video power supply can be found in Appendix C.

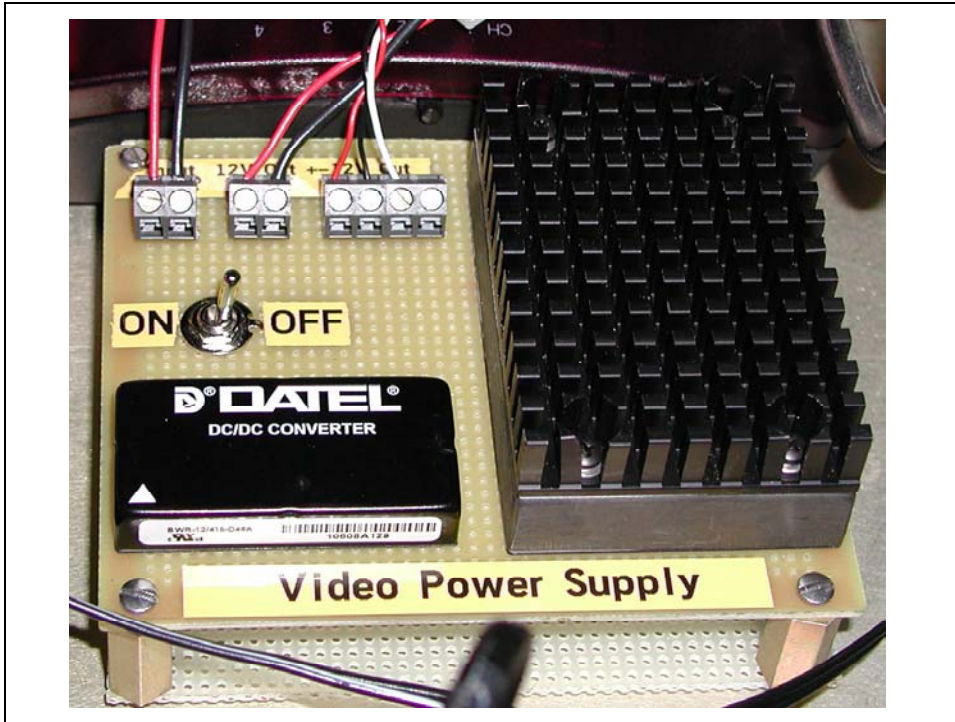


Figure 31. Video Power Supply

Prior to table operations, the optical system is aligned with the table at rest (i.e. not floating). When the table is floated, it rises $\sim .375''$. As the primary mirror is only 1" in diameter, this can move the aim point of the bench top laser from mirror center to almost the primary mirror edge! A means of raising the laser on the optical bench was required.

A scissors-type lifting jack was obtained and mounted to the optics bench. It provided some level of control of laser level, but was plagued by the fact that it did not maintain a constant position while being raised and lowered. Future versions of the TASS should include a precision lift under the laser to alleviate this problem.

I. MASS PROPERTIES

1. Background

The TASS was delivered with a basic mass properties spreadsheet that contained a significant number of inaccuracies and omissions. This spreadsheet was discarded and a new spreadsheet was created to determine the mass properties of the table. Mass data was collected for this spreadsheet from technical data, where available. In the case of

custom-built parts, masses were estimated based on material density and geometry. Where possible, parts were removed from the table and weighed.

Position data was measured using a tape measure. The center of the table top is located at a bolt that holds the spherical air bearing in place. This bolt provided a reference point for measuring in the X_M and Y_M axes. The top of the table is approximately 3 inches above the center of rotation (and desired center of mass), and acted as a reference point for measuring in the Z_M direction.

Only basic geometric shapes were utilized in calculating moments of inertia, comprising rectangular boxes and cylinders. The hemispherical air bearing moments of inertia were provided by the manufacturer, and entered directly. If an object on the table was of a shape more complex than a cylinder or box, it was entered as an object of equivalent size, shape, and mass.

2. Mass

The initial mass estimate of the TASS by GDC was 386 pounds, and the secondary mass estimate (after re-engineering the sun sensor) was 503 pounds. Neither of these estimates contained an accurate breakdown of TASS components or their masses.

The NPS mass properties spreadsheet indicates a mass of 430 pounds. However no empirical verification of the overall TASS mass had been accomplished to provide verification of any results. Two large Toledo scales provided the solution to this problem. The scales were placed under two opposing balancing legs, and the TASS was floated. Wooden spacers were placed between the balancing legs and the scales, and the balancing legs were extended to provide a tight fit. Air was then removed from the air bearing, and the table settled down on the balancing legs, fully supported via the spacers on the two scales.

The TASS mass was determined to be 421 pounds. This number is independent of any weights on the balancing legs, and represents the TASS base structure with the BRMP and its supporting systems installed. This validated the NPS mass model to within three percent, and allowed use of this accurate mass in the determination of principal axes and moments of inertia.

3. Moments of Inertia and Principal Axes

The development of moments of inertia for the table was desired as a basis for future system modeling. The moments of inertia were calculated for each component on the table, then each components MOI was translated into the mass properties frame via the parallel axis theorem.

The moments of inertia of the TASS (in the mass properties frame) were calculated to be:

$$\begin{aligned} I_{xx} &= 21.57 \text{lb} \cdot \text{in}^2 = 29.24 \text{kg} \cdot \text{m}^2 \\ I_{yy} &= 21.44 \text{lb} \cdot \text{in}^2 = 29.07 \text{kg} \cdot \text{m}^2 \\ I_{zz} &= 33.19 \text{lb} \cdot \text{in}^2 = 45.01 \text{kg} \cdot \text{m}^2 \end{aligned}$$

The TASS was delivered with the original control axes aligned with the principal axes. The addition of the BRMP modified the principal axes of the table such that use of the original control program was impossible.

Following extensive testing of the TASS, it was noted that the table was extremely difficult to control, and that its instability resembled the nutation inherent with motion about a non-principal axis. [Ref. 6]

In order to determine the principal axes, the TASS was first finely balanced, then one pound weights were fitted to the bottom of each balancing leg. This had the overall effect of lowering the center of mass of the table a fixed, calculable amount below the center of rotation. This known distance was coupled with the tables' pendulum period and mass to determine the moment of inertia.

An object can only oscillate about an axis without nutation if that axis is a principal axis. The pendulum testing was accomplished by floating the table and depressing one side until it reached the limit of the air bearing. The table was then smoothly released to impart no external force. The table then entered a pendulum-like state, with the air bearing and air friction on the table itself providing a small amount of damping. If nutation was observed after a short period of time, the table was clearly not oscillating about a principal axis. This process was repeated at intervals ($\sim 5^\circ$) around the table, until no nutation was observed.

Two axes were discovered to meet these criteria on the table approximately 90 degrees apart. This indicates that the Y_C axis is coincident with the Y_P axis, and that the control axes and principal axes are coupled by a single rotation about the Y -axis. (Figure 32) This fact was incorporated into the control laws, and is discussed at length in Chapter III.

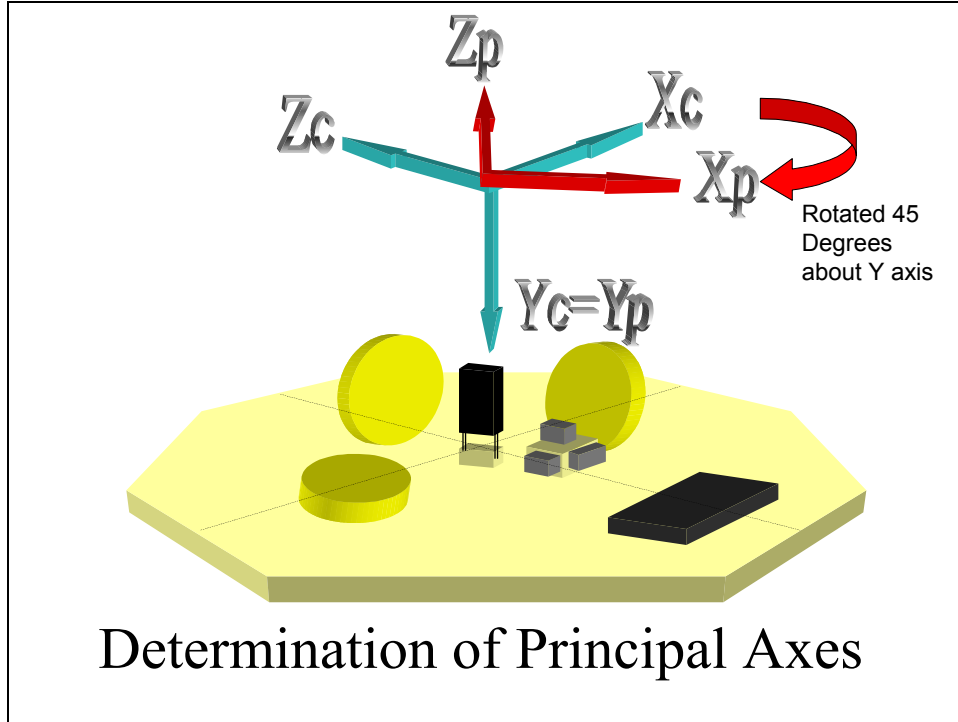


Figure 32. Determination of Principal Axes

The periods of nutation about these two axes were $T_x = 13.51$ seconds, and $T_z = 13.16$ seconds. The mass added was 4 pounds, 15 inches below the center of rotation. The pendulum equation is:

$$T = 2\pi \sqrt{\frac{I}{mg\ell}}$$

where T is the period, I is the moment of inertia, m is the mass, g is the acceleration due to gravity, and ℓ is the distance between the center of mass and center of rotation. Based on this data, the empirically derived moments of inertia about the X_P and Z_P axes are

$$I_{xx} = 31.3 \text{ kg} \cdot \text{m}^2$$

$$I_{zz} = 29.7 \text{ kg} \cdot \text{m}^2$$

These are very close to the values of 29.2 kgm^2 and 29.1 kgm^2 analytically derived in the spreadsheet, validating the mass properties model.

4. Balancing

A key difficulty in table operation was the fine balancing of the TASS. The slightest change on the table such as a yellow sticky note, a wire slightly shifted, provided sufficient change in the tables' balance to cause it to drift from a neutrally balanced state to an out-of-balance state. Small errors in balance were overcome with reaction wheel inputs (until the wheels saturate), but without momentum dumping this control only lasts for a short time.

Table balance was achieved by first lowering the balance legs until the table was decidedly stable (center of mass lower than center of rotation). The table was leveled by adding weights around the balance legs (for coarse adjustments) and the fine balance weights for fine adjustments. The balance legs are incrementally raised and the table leveled until the center of mass is at the center of rotation. This condition can be recognized when the table is stable no matter what attitude it is placed in. If the balance legs are raised too far, the table will become unstable and will always fall no matter what the initial attitude is. Table balance was maintained between data runs by simply not modifying the table in any way.

III. SOFTWARE DEVELOPMENT & SIGNAL PROCESSING

The Matlab software package was used to interface with the National Instruments cards in order to process inputs from the table and provide appropriate command signals back to the table. This chapter will review the specifics of the I/O cards and the software packages used, and show how the control laws were implemented. The signal processing required making these input signals useable, and diagnostic programs will also be discussed.

Section A provides a brief summary of the interface cards used to share signals with the TASS, Section B provides a brief description of the software packages used for control, interface, and analysis. Section C details the signal processing methods and filters utilized to refine the sensor data collected, and Section D concludes the chapter with a description of the TASS controller and its development.

A. INTERFACE CARDS

Sensor inputs to the computer and control outputs from the computer are via two National Instruments DAQcard-1200 PCMIA cards (DAQcard(s)) at memory locations 1000h and 1200h. Each card contains eight $\pm 5V$ analog inputs, two $\pm 5V$ analog outputs, and 24 digital I/O ports. The inputs and outputs to each card are summarized in Appendix D.

B. MATLAB/SIMULINK/REALTIME WORKSHOP INTEGRATION

The Matlab package Real-time Workshop allows the computer to directly interface with the DAQcards. This interface is accomplished via SIMULINK, another Matlab package that offers graphical manipulation of signals and systems.

When a signal needs to be accessed, a graphical icon representing the DAQcard is created, and the signal type and number is specified, along with the sampling rate. The software and hardware were designed to sample every .04 seconds, or 25 samples per second.

C. SIGNAL PROCESSING

During the initial development of the control laws it was discovered that poor signal quality from the sensors was significantly degrading the controllability of the TASS. In order to achieve adequate performance, signal processing was required in order to extract the signal data.

1. Rate Gyros

The signal generated by the rate gyros has two characteristics that make it difficult to utilize. First, the gyro is noisy, and this noise is significant at the near-zero rates encountered during normal operation. Second, the gyro experiences a bias that slowly varies during operation, and varies widely day-to-day (i.e. between on-off-on cycles). Figure 33 shows a sample of the rate gyro raw data, demonstrating the ± 0.01 Volt noise and DC offset.

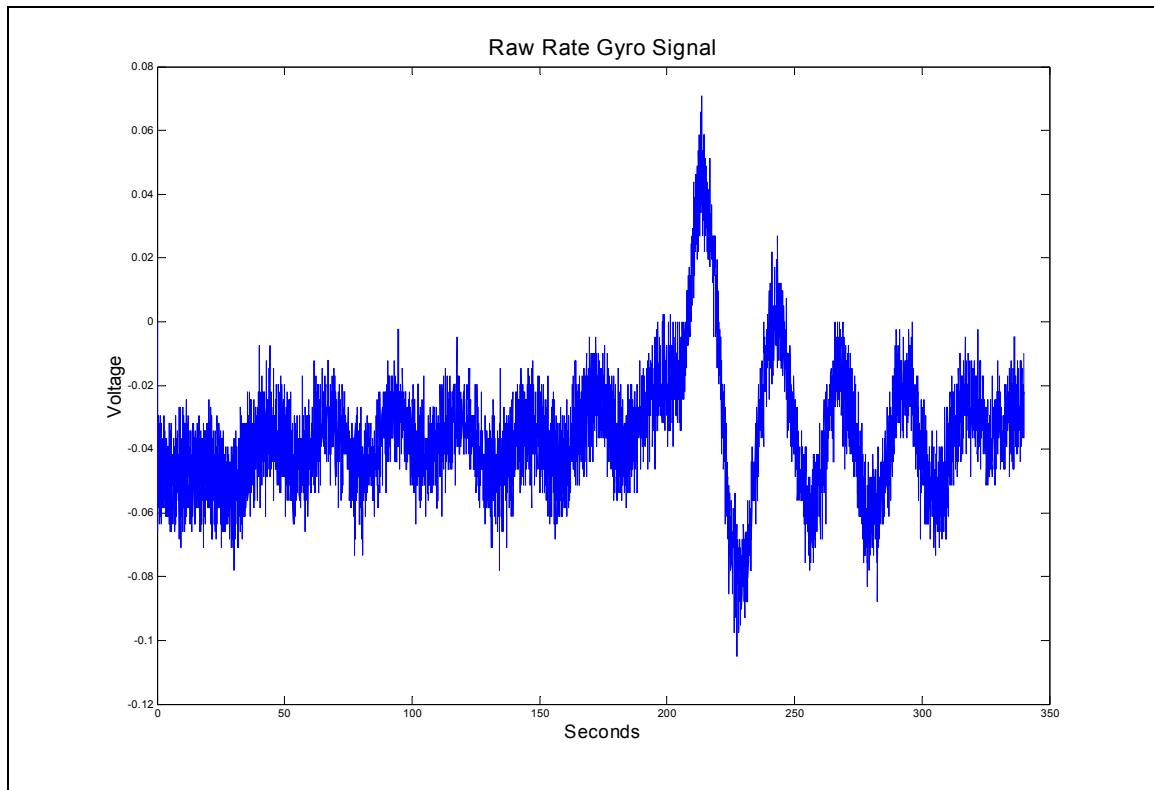


Figure 33. Raw Rate Gyro Signal Illustrating Noise Level

Several low-pass filters were considered to remove the high-frequency noise in the gyro signal. The noise was eliminated using a low-pass Butterworth filter [Ref.7].

This filter was chosen for its simplicity and minimal time delay imposed upon the signal (Figure 34).

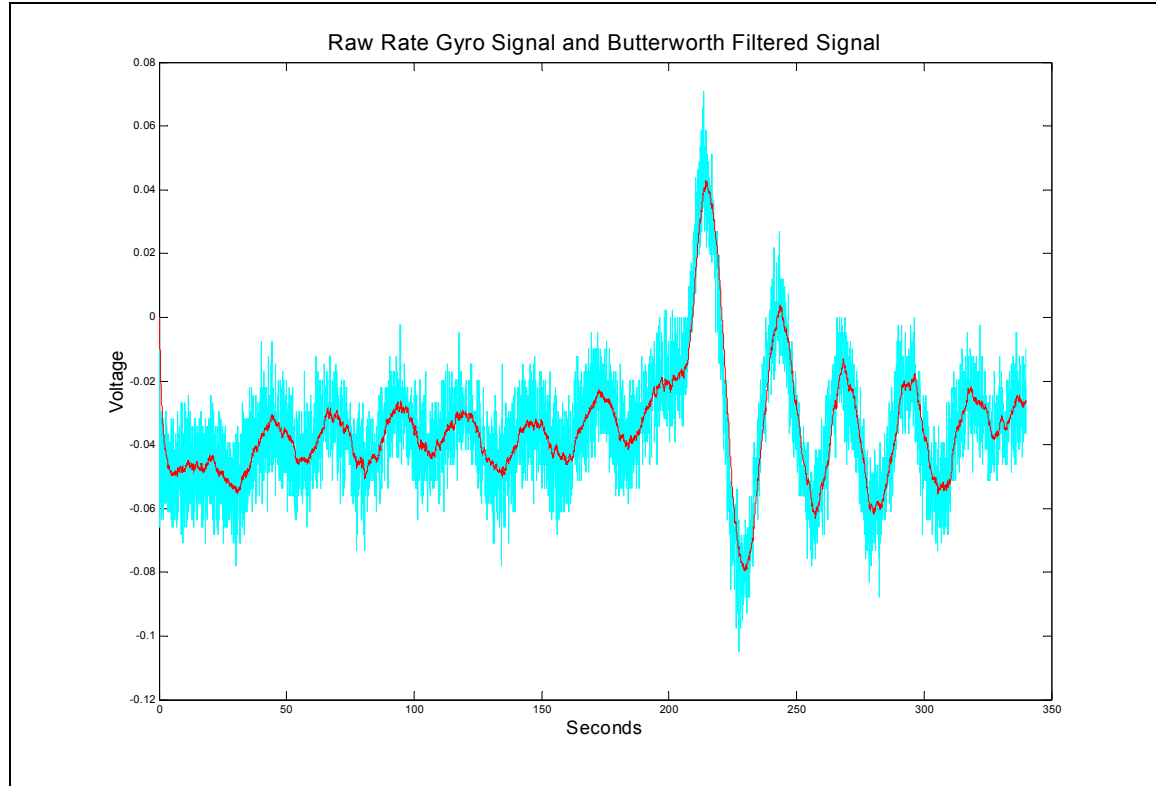


Figure 34. Raw Rate gyro Signal and 1st Order Butterworth Filter Output

The variable bias was eliminated using a digital filter suggested by Professor Roberto Cristi. The filter is characterized by the equations:

$$y(n) = ay(n-1) + b[x(n) - x(n-1)]$$

$$0 < a < 1$$

$$b = \frac{1+a}{2}$$

This digital filter is based on the assumption that the rate will always oscillate about zero. It will produce erroneous results if used while slewing the TASS through large angles, or if there is a significant balancing bias on the table with 'loose' position gains. The combination of the Butterworth filter and the above digital filter is referred to as the 'CC Filter' ('CC' refers to 'Cristi-Chernesky').

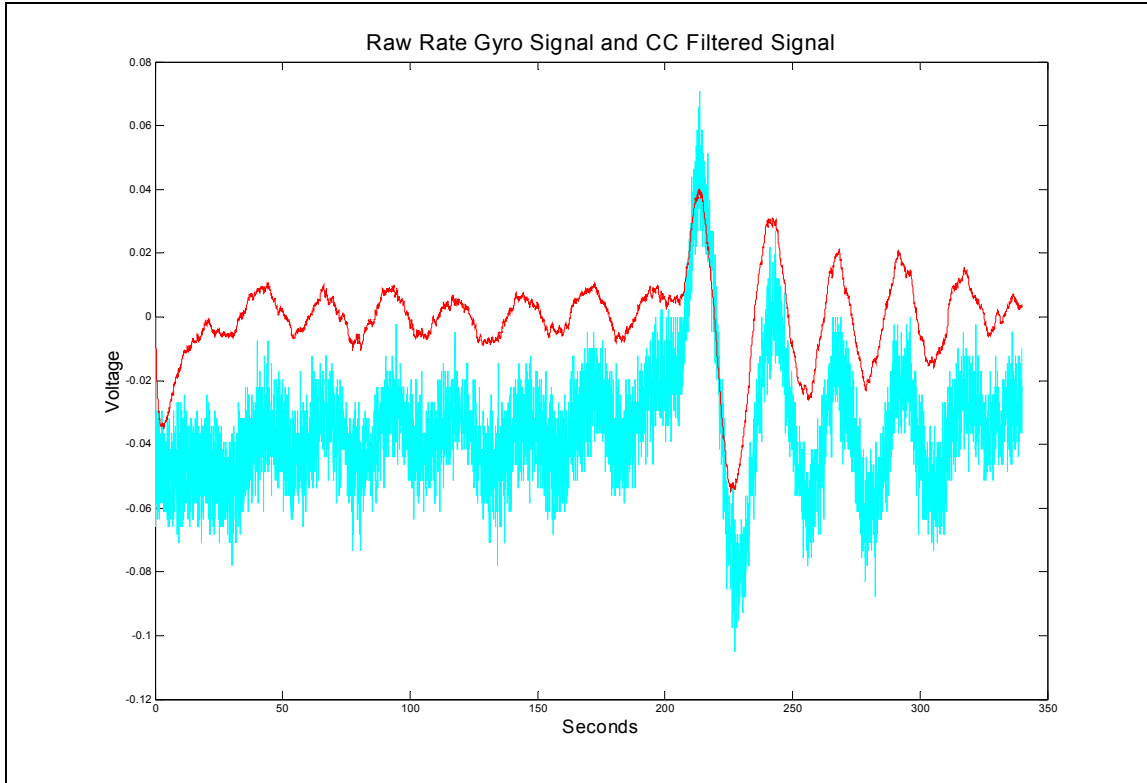


Figure 35. Raw Rate Gyro Signal and CC Filter Output

A value of $a=0.99$ was chosen to minimize the data (amplitude) loss resulting from the digital filter. The consequence of this robust response is a 15-20 second time period required for the filter to initially zero out the gyro bias, as shown in Figure 35. As the value of a gets larger less of the signal (vice noise) is filtered out, but at the cost of a longer time response.

2. Sun Sensor

As discussed in the hardware section, the sun sensor has a stable, linear response for any given position of the sun/star constellation. However, the signals from the sun sensor also have a quantization, or graininess, in their response. This quantized signal can be seen on all three axes, but is most pronounced on the Y_C -axis, which has the widest field of view (Figure 36). The particulars of why this quantization occurs are unknown due to the proprietary nature of the sun sensor. GDC has confirmed that the output of the sun sensor is consistent with proper sensor operation.

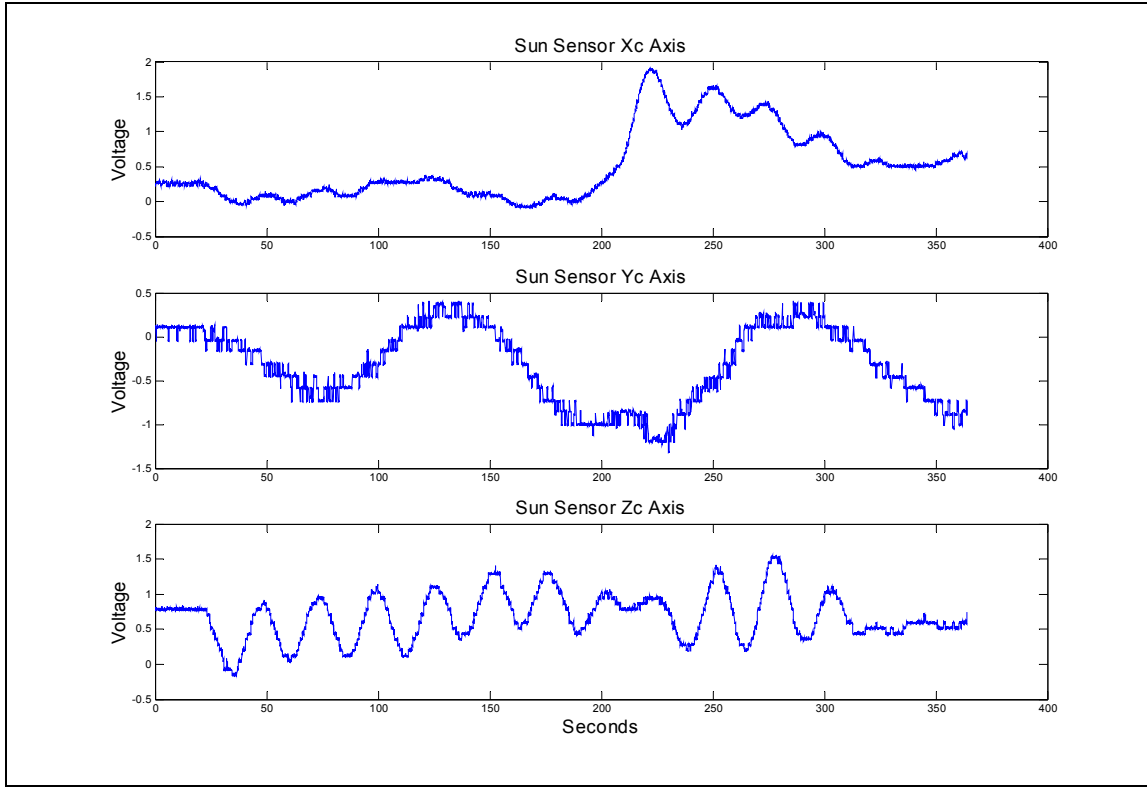


Figure 36. Sun Sensor Output, Note Quantization in Y_C Axis

After testing several filter designs, a Butterworth filter [Ref. 7] was chosen to smooth the sun sensor data. Care was taken in selecting the order of the filter, as higher order filters had a significant time delay associated with them. Figure 37 illustrates the effect of increased filter order on time delay over a short signal interval.

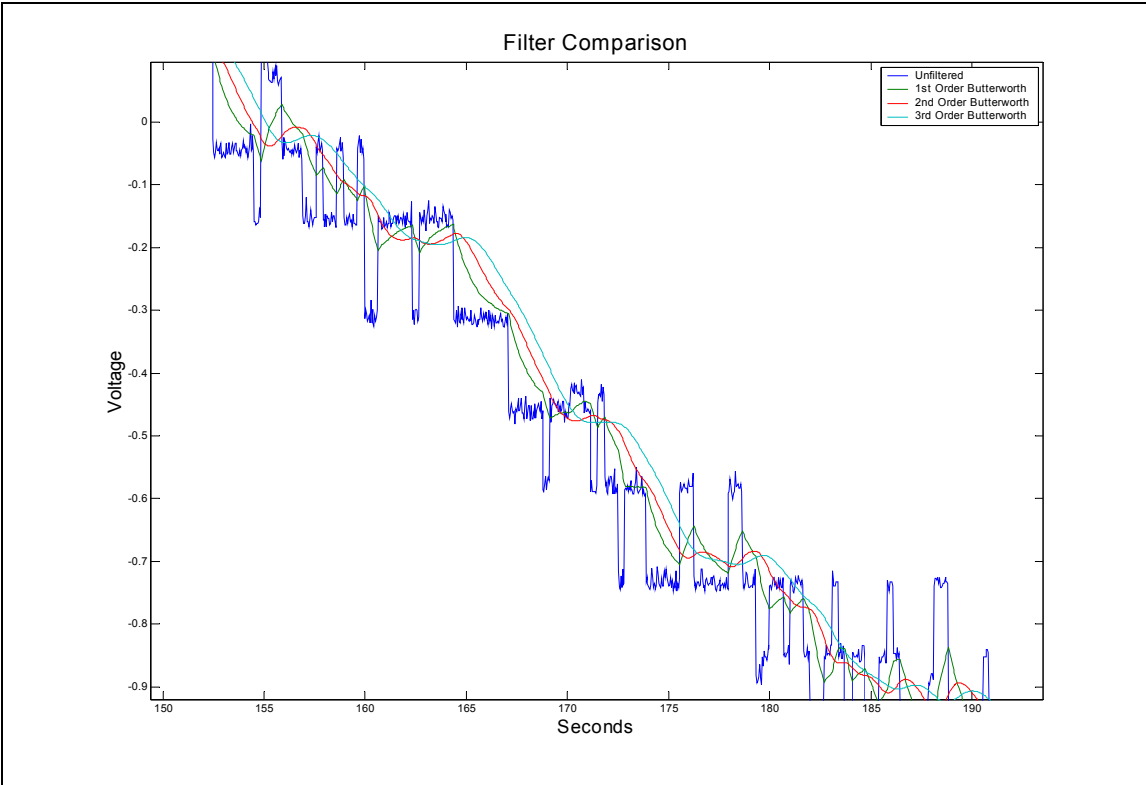


Figure 37. Filter Comparison

It was experimentally determined that a time delay of greater than roughly 0.5 seconds produced unacceptable controllability given a slight off-balance table condition. A first-order filter was chosen based on this data.

D. CONTROLLER DEVELOPMENT

The initial controller provided with the TASS at delivery was optimized for thruster control, utilizing a Proportional-Derivative (PD) controller. This provided acceptable attitude control with the higher-torque thruster system, but marginal performance when using only the reaction wheel system. This PD system was used as a basis for the initial reaction wheel only controller. The simulation was altered to provide a user-friendly front screen (Figure 38) including all user inputs. Several major refinements were required during the evolution of the controller.

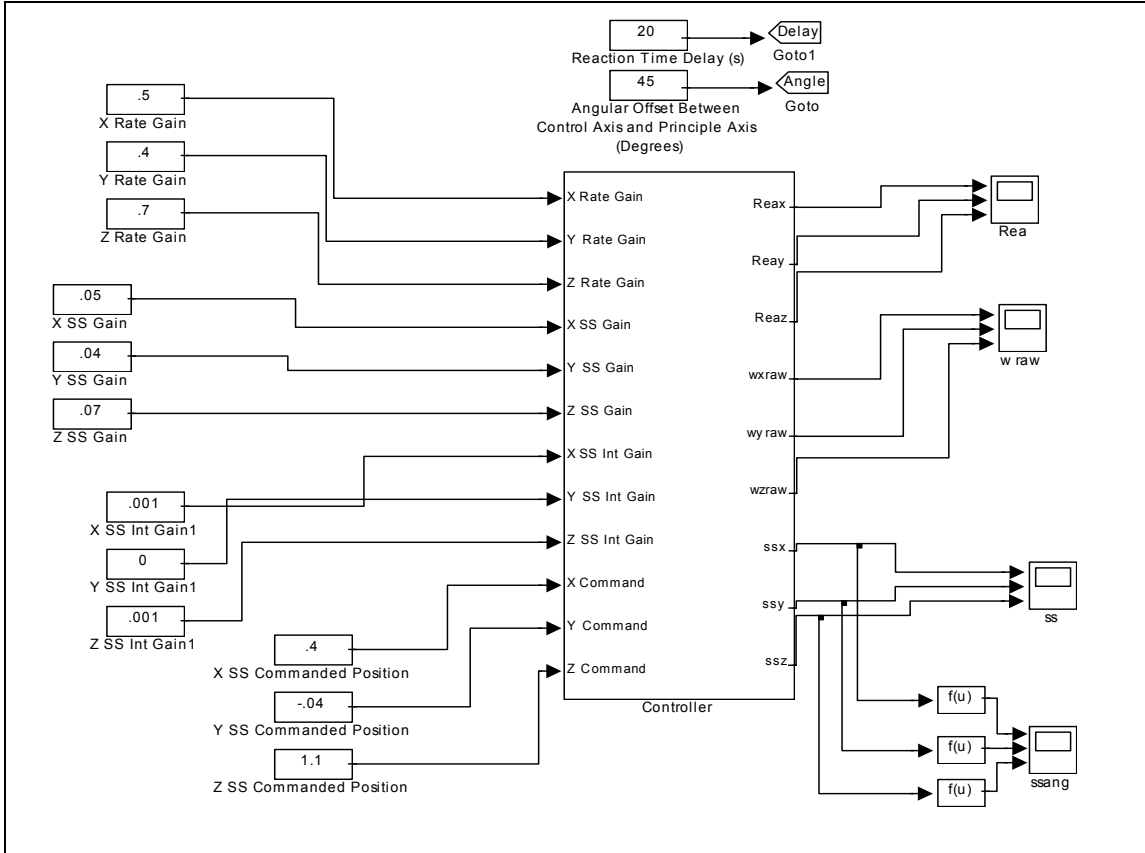


Figure 38. Controller Front End Screen

The first of these refinements was the incorporation of integral control to the control law [Ref. 8]. This was a result of the difficulties in fine balancing the table. It was recognized that the table was extremely difficult to ‘perfectly’ balance, and the PD controller allowed the TASS to stabilize away from the intended commanded position (A function of the constant, imbalance-related bias). This large position error was inconsistent with the accuracy required for laser alignment with the primary mirror. The PID controller eliminates this large steady-state error due to slight table imbalance.

Another refinement was a result of the principal axis offset. The control axes are offset from the principal axes by 45 degrees. Attempting to control around a non-principal axis results in wild nutation [Ref. 6, 9]. It was not feasible to detach all control hardware and offset it by 45 degrees. This was cost (and space) prohibitive, and this act would change the principal axes itself.

Instead a software solution was created. All input signals from sun sensors and rate gyros were multiplied by a direction cosine matrix (DCM) to shift from the control

axis system to the principal axis system. These signals can then be passed through a PID controller, and the outputs passed through the inverse DCM to shift the output signal into the control coordinate frame. These output signals are then sent to the reaction wheels. This allows for independent control around each principal axis, while retaining the hardware configuration on the table. This also allows for future modifications to the TASS that may alter the location of the principal axes. The DCM is shown below, with α being the offset angle around the Y_C -axis. It should be noted that the DCM implementation assumes that the Y_C axis is coincident with the Y_P axis.

$${}^P C {}^C = \begin{bmatrix} \cos \alpha & 0 & -\sin \alpha \\ 0 & 1 & 0 \\ \sin \alpha & 0 & \cos \alpha \end{bmatrix}$$

The final issue in controller development is the time delay associated with the CC filter. Roughly 20 seconds is required for the current filter to zero out the variable bias in the rate gyros. A time delay is implemented which prevents control output to the reaction wheels for the specified time, and blocks any accumulation of integral control signal. Operationally, the TASS is grounded during these initial 20 seconds, ensuring the rates are drawn to zero bias at the beginning of operation.

The final control law for each principal axis follows the following equation, and is pictured in Figure 39. The saturation block is used to limit the control output to $\pm 1V$, in order to conserve battery capacity.

$$\text{Reaction} = K_P(\text{Commanded Position} - \text{Sun Sensor}) - K_D(\text{Rate Gyro})$$

$$- \int K_I(\text{Sun Sensor} - \text{Commanded Position})$$

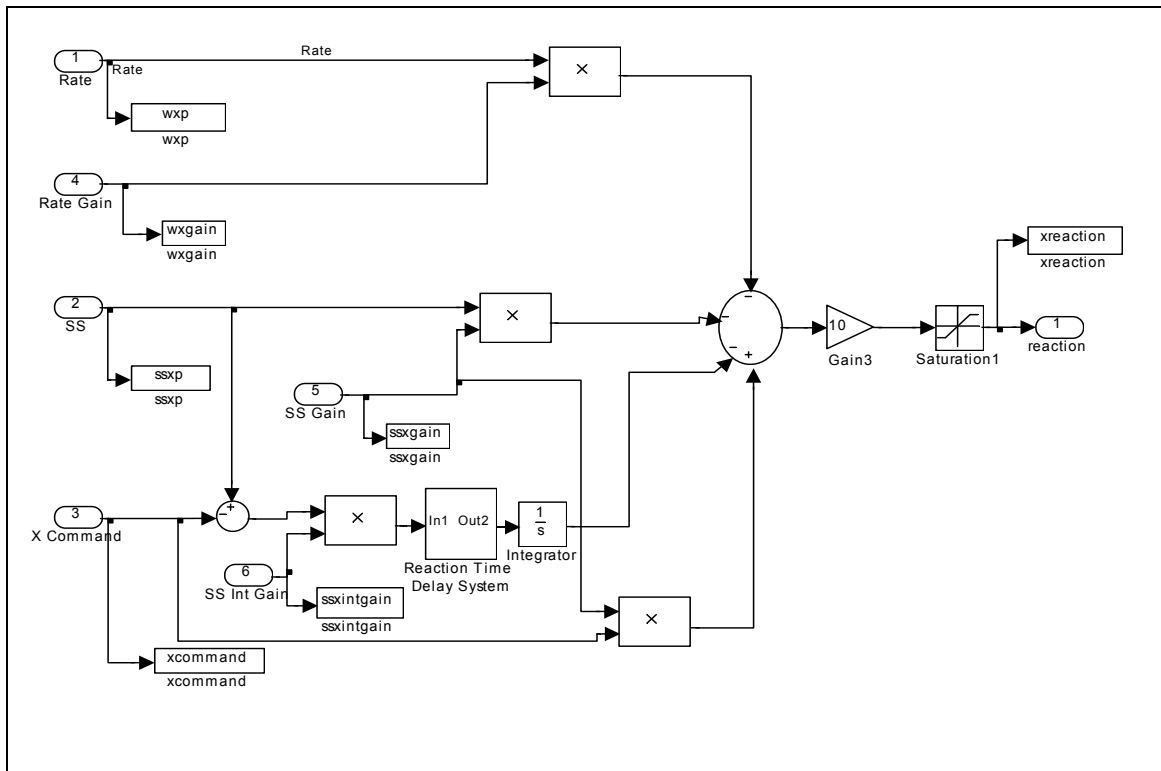


Figure 39. Single Axis PID Control Implementation

THIS PAGE INTENTIONALLY LEFT BLANK

IV. SYSTEM ANALYSIS

Full system testing of the TASS was performed on 03 November 2001. This test included table operation holding a pre-defined attitude, and laser operations including pattern drawing and target tracking. This chapter presents the sensor inputs and control outputs associated with this successful test, as well as photos taken from the test run video.

A. RESULTS

The TASS was well balanced for this test, and the batteries were in a state of full charge. All systems had been tested the day prior, and the TASS sun sensor position was from the previous days operations. The bench-top laser had not been moved or disturbed.

The gains used for this test were as follows:

	Position Gain (Sun Sensor)	Integral Gain (Sun Sensor)	Rate Gain (Rate Gyro)
X _P Axis	0.5	0.05	0.001
Y _P Axis	0.4	0.03	0
Z _P Axis	0.7	0.04	0.001

Table 6. Gains Used For Full System Test

It should be noted that the gains listed here, as in the SIMULINK diagram, refer to principal axis gains.

The position of the table as measured by the sun sensors is shown in Figure 40. The scales on all three axes is from -3° to 3° , clearly showing the quantization in each axis. The red lines indicate the commanded position.

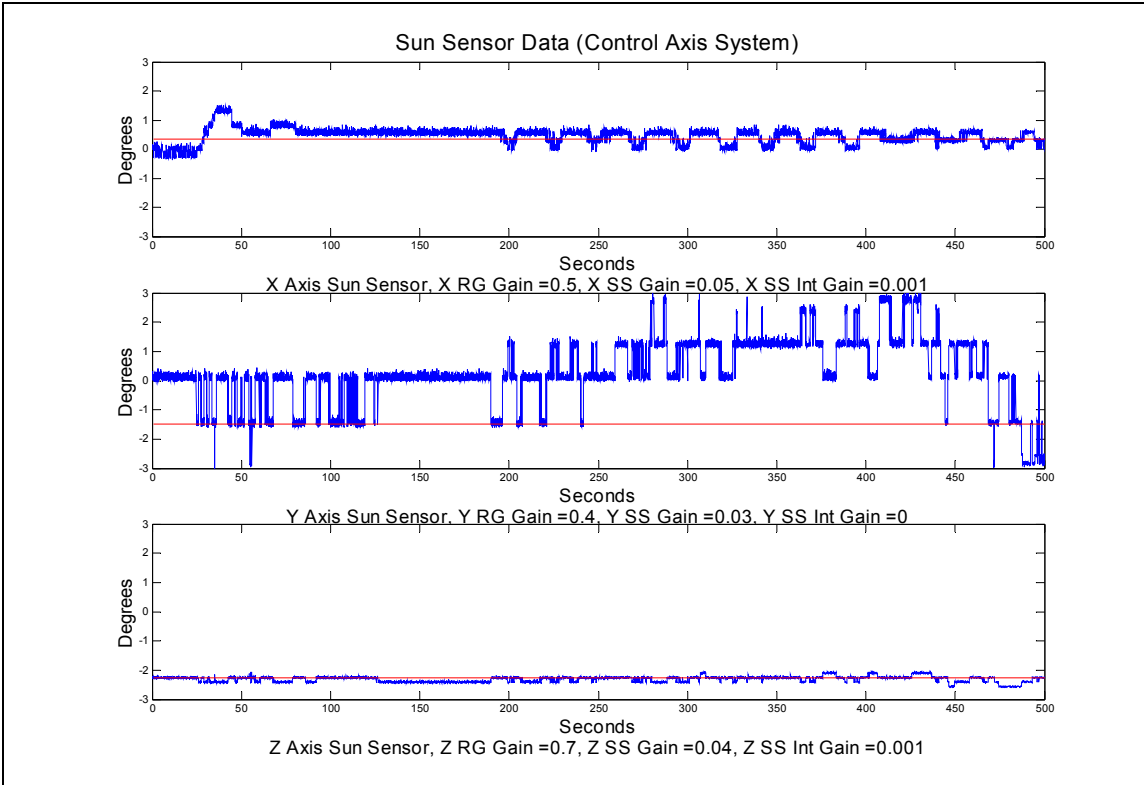


Figure 40. TASS Position Data

The X_C and Z_C axes were very well controlled around the commanded position, however the Y_C axis was not. The table drifted a significant distance away from the commanded position before correcting. This loose control was required due to the poor sensor quality. If higher position gains were used, the TASS fluctuated around the commanded position. This axis was also the axis of the highest moment of inertia, and thus the reaction wheel had the least control authority.

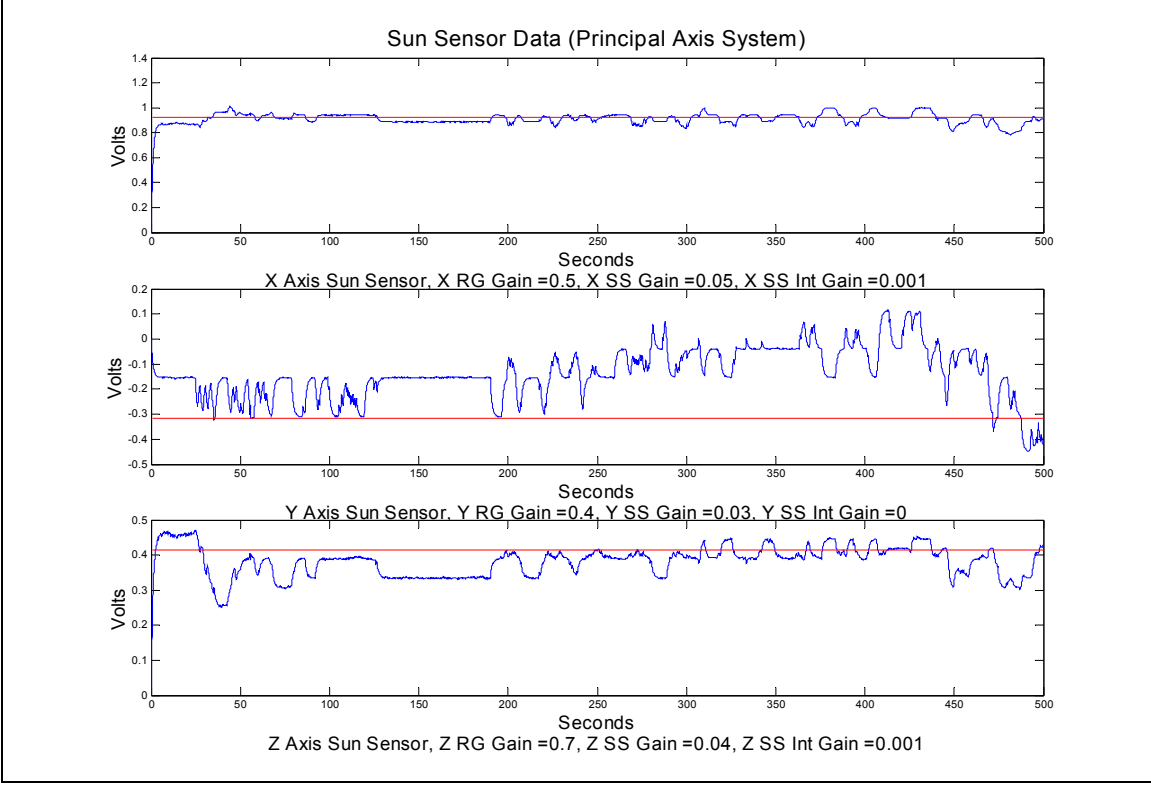


Figure 41. Filtered Sun Sensor Data in Principal Axes

Figure 41 is the filtered data being fed into the control law from the sun sensors. This data had been through a DCM to align it with the principal axes, and filtered using a first order Butterworth filter. The vertical axes here are in volts, vice degrees. This figure illustrates that although the first order Butterworth filter helps smooth the Y_p -axis data, the signal is still very jagged.

Figure 42 shows the raw rate gyro signal in the control axis frame, and Figure 43 shows the filtered signals in the principal axis frame. The improvement in signal quality is obvious. The spike in the raw data at time 20s is due to the TASS lifting off the air bearing. The control output to the reaction wheels is shown in Figure 44. The flat portion for the first 20 seconds is the time delay in the SIMULINK model blocking any control output during the time delay period. The laser testing proceeded normally from time 20s to 250s, when the TASS drifted out of tolerance in the Y_C axis. At this time the bench-top laser was no longer striking the primary mirror, and did not re-acquire until time 480s. At time 480s the table had a large positive rate, and acquisition lasted only a few seconds before the table went out of tolerance again. The period between 20s and

250s allowed sufficient time to test the optical train in all modes. Target tracking was accomplished, with the red laser successfully tracking the green laser (Figure 45). The ‘Draw Square’ and ‘Draw Expanding Circle’ features were also tested, indicating proper function of the FSM and associated electronics.

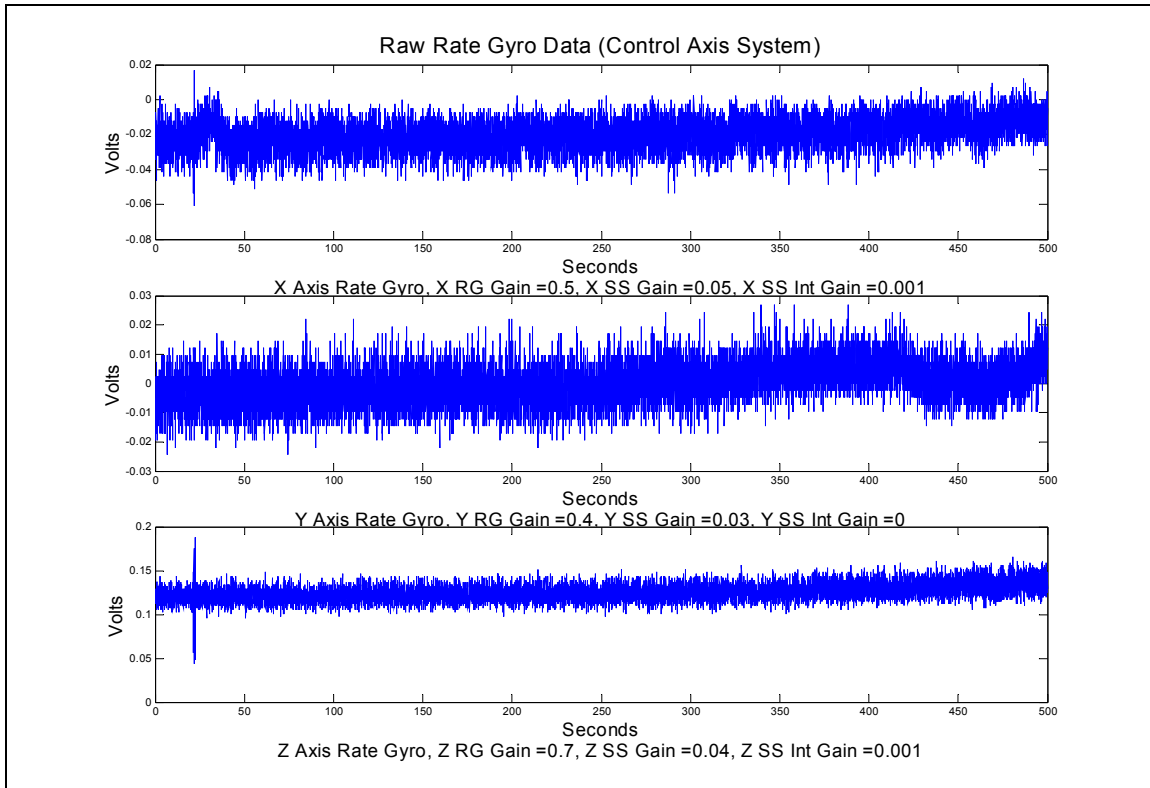


Figure 42. Raw Rate Gyro Data, Control Axis System

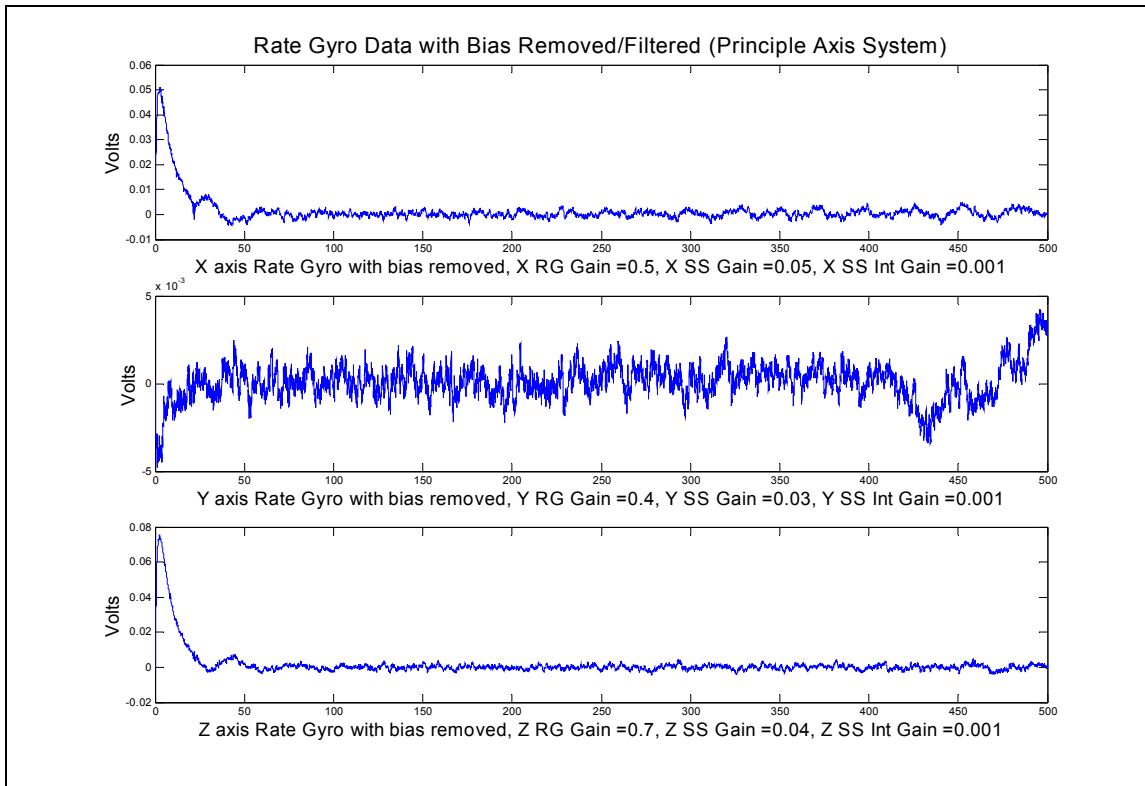


Figure 43. Filtered Rate Gyro Data, Principal Axis System

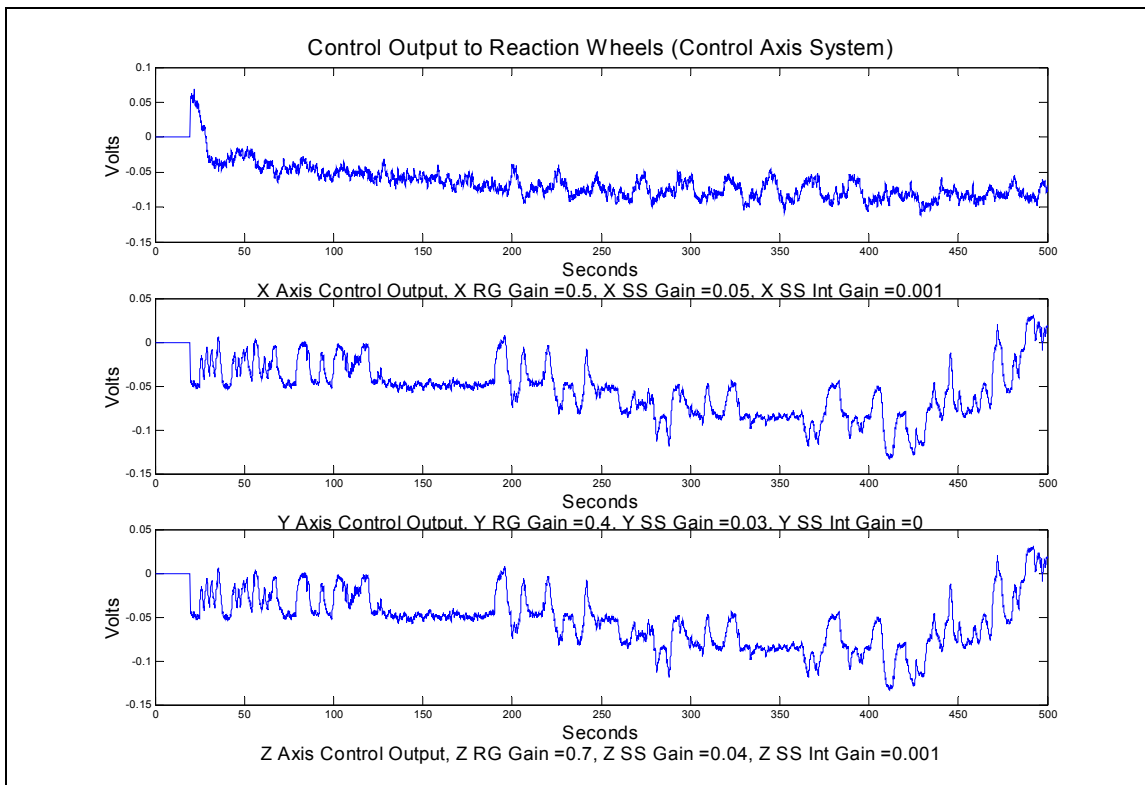


Figure 44. Control Output to Reaction Wheels, Control Axis Frame



Figure 45. Photo Of BRMP Operations – Integrated Tracking

V. FUTURE SENSORS AND SYSTEMS

The TASS is not a static piece of hardware. Indeed, it has been “designed to be redesigned”, capable of adding payloads to suit the needs of the department. Even now, a redesign of the table is in the works. Changes currently include shifting from an onboard laptop to an RF controlled computer, and the addition of an optics bench board on top of the TASS to assist in further BRMP testing.

The experimentation and research performed with the TASS offers insight into what areas can be further improved. Three areas requiring significant improvement are outlined here, with possible solutions outlined.

First, an improvement in sensor accuracy is required in order to allow for continuous TASS/BRMP operation. The sun sensor utilized on the existing TASS does not have adequate resolution to control the table to the required tolerance.

Second, the means of calculating mass properties of the TASS needs to be improved. Steps in this direction would lead to a more precise determination of principal axes, and could lead to the incorporation of a device to automatically place the table in balance.

Lastly, the TASS must be characterized and modeled to allow for offline determination of optimal gains, and to allow for offline testing of alternative methods of control.

A. SENSOR IMPROVEMENTS

1. Sensor Requirements

The current BRMP has a 1” diameter primary mirror. This mirror is located 20” from the center of rotation of the table, and seven inches above the plane of the table. This positioning, almost at the edge of the table, makes it extremely sensitive to deviation in the Y_C axis. If a triangle is formed from the Y_C axis to the mirror, with the mirror as a side, the angle subtended by the mirror is:

$$\alpha = \sin^{-1} \left(\frac{\text{Opposite}}{\text{Hypotenuse}} \right) = \sin^{-1} \left(\frac{1''}{20''} \right) = 2.86^\circ$$

The commanded position of the TASS is determined as follows: The table is rested on the air bearing so that the optics train is pointing at the target (in our case, the map of the world.) The laser is turned on and aligned with the center of the mirror, and the optics are adjusted to produce a laser output on the map of the world. A sun sensor reading is taken in this position, and entered as the commanded position. When the table is floated, the laser is translated 3/8" higher to account for the air cushion.

Thus, the table has the laser centered on the primary mirror during operation. It can therefore only drift half of the mirror diameter ($2.86^\circ/2$), or 1.4° , in order to maintain the laser on the primary mirror. As was demonstrated in chapters 2 and 3, the Y_C axis sensor is only accurate to quanta of $\sim 1.2^\circ$. This is not accurate enough position knowledge to control the table reliably about the Y_C axis.

In order to achieve sufficient pointing accuracy during operation, sensors with position knowledge of the order 0.1-0.2 degrees are required.

2. Pseudolite GPS

The use of the Global Positioning System (GPS) for satellite position information has been used for many years. However, the use of GPS for satellite attitude control has recently been demonstrated. Using several antennas on the surface of a spacecraft and two GPS signals, the phase difference between different antennae can be translated into an angular position with respect to that satellite along the axis formed between the two antennae. Two signals are required to eliminate the angular ambiguity. If multiple antennas and satellites are used, and the position of each GPS satellite is known (via ephemeris data), then very precise attitude knowledge can be determined [Ref. 10, 11]. Although research is proceeding rapidly in this area, the accuracy currently possible is on the order of one degree [Ref. 12].

While this works well in space, GPS signals do not have the signal-to-noise ratio to penetrate into the murky basements where satellite attitude control is practiced and developed. In order to overcome this difficulty, pseudolites (pseudo-satellites) have been developed to mimic the signals created by the GPS constellation.

The concept of operations is as such: Several pseudolites are emplaced around the TASS laboratory, each with its own signal generator. Four (or more) antennas are placed on the TASS in such a way as to maximize the baselines between them. These antennas are interfaced with a computer via a data acquisition card. This allows the GPS signal demodulation and processing algorithms to be built and implemented in a software package such as SIMULINK [Ref. 13].

3. Star Trackers

The use of a commercial star tracker for attitude determination presents many problems for the TASS. Besides their high cost, an accurate star field would need to be constructed inside the laboratory to take advantage of the full capabilities of the star tracker. These reasons force us to look to a custom designed star sensor for our needs.

In many ways, the desired star tracker is similar to the current three-axis sun sensor. The same three-axis attitude information is desired, and a simple CCD construction suits our needs. However, some additional requirements have to be incorporated into a new sensor to make it more flexible and robust.

The use of infrared emitters and detectors is one of these requirements. Great difficulty was encountered attempting to use visible light for our current sun sensor, necessitating construction of a large blackout hood over the TASS. This was acceptable in our current facility, but in the upgraded TASS laboratory it will be more difficult to block out ambient light. Infrared emitters offer an alternative that can be used in ambient light with little sensor degradation. Additionally, several infrared sources at different frequencies (infrared constellations) can be placed around the room to allow for large-angle slew maneuvers. The CCD detector will be able to discriminate between the frequencies and identify different constellations.

The other additional requirement is that the field of view be sufficiently wide for coarse acquisition (approximately a 20-30° cone) and that the CCD array be of sufficient resolution to provide position knowledge to within 0.1-0.2 degrees.

4. Inertial Measurement Unit

Several other satellite simulators have chosen an inertial measurement unit (IMU) as their primary source of rate and position data [Ref. 15]. This can provide many

advantages, including having the data from the IMU in quaternion or Euler angle format. The Crossbow AHRS300A system provides three-axis position, rate, and acceleration information, and has been used successfully on the Satellite Simulator at the Georgia Institute of Technology. While the position knowledge of these systems are typically not adequate for laser operations, they do provide an excellent coarse-pointing capability in a single package with a simple interface.

5. Laser Tracking

Currently there is no data transfer between the BRMP and the TASS attitude control system. A slight modification of the BRMP would allow using the incoming laser beam as a source of attitude data. Figure 46 shows this hypothetical modification. The incoming laser beam passes through a beam splitter, diverting a portion of the main beam to an alignment tracking sensor (ATS). The ATS is constructed of a four quadrant photocell. When the ATS and the jitter sensor simultaneously ‘see’ the laser, it can be inferred that the laser is propagating through the optical train successfully. Once this is known, the laser position in the ATS can be fed to the TASS attitude control system with control authority to maintain the beam in its present position. The attitude control system is thus locked on to the incoming laser beam, maintaining the proper attitude for optical alignment and target tracking.

BRMP With Alignment Tracking Sensor

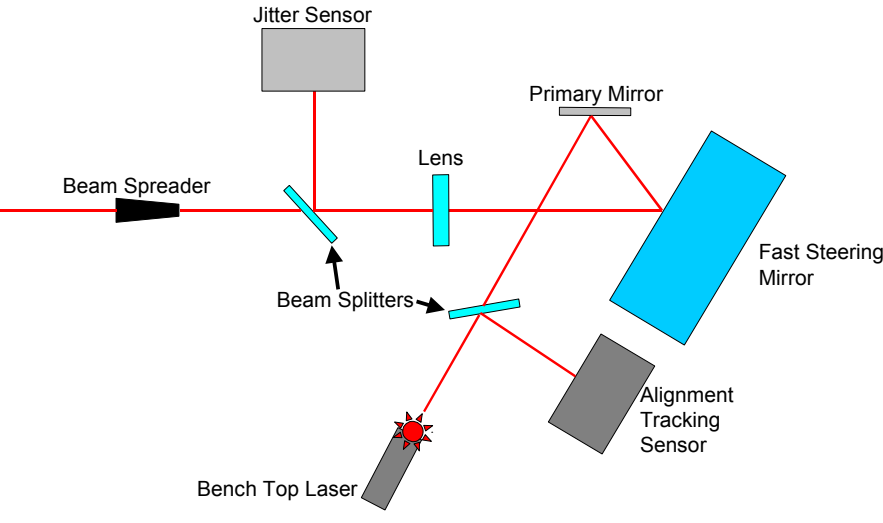


Figure 46. BRMP With Alignment Tracking Sensor

B. BALANCING IMPROVEMENTS

Balancing the TASS, and determination of its mass properties, offered several major challenges over the course of this research. While this area has much room for improvement, two key topics will be covered here: The addition of an active balancing unit to automatically, continuously balance the TASS, and the use of computer aided design (CAD) as a tool to track mass properties of the table.

1. Active Balancing Unit

Typically, an hour was spent prior to any data run on the TASS attempting to fine-tune the balance. If a component had been added to or removed from the table this process could take several days. This is time better spent on research.

The incorporation of an active balancing unit (ABU) would simplify operation of the table without a significant addition of hardware [Ref. 15]. These would be the equivalent to magnetic torque rods on a spacecraft, providing a constant torque about the center of mass. In the case of the TASS, however, torque could only be applied about axes not perpendicular with the gravity vector, in our case the X_C and Z_C axes.

Any ABU will involve moving a mass (or masses) on the table in order to slightly change the position of the center of mass. It will act in concert with a PID (or other) controller to minimize the integral portion of the control law output: The steady-state bias. If this bias is minimized, then the table is in balance.

Even this system is not without manual adjustment. The user must still adjust the center of mass fairly close to the center of gravity, or at least within the achievable control moment of the ABU. The user must also set the center of mass equal to the center of rotation, although a 3-axis ABU would eliminate this requirement.

Other design issues associated with an ABU are the reaction forces in moving the mass (or masses) on the table. If the ABU utilizes a single motor for any mass movement, it will produce a reaction torque about its spin axis. A reactionless system is desired. Such a system is shown in Figure 47. Here, two stepper motors are attached to gears that engage a balancing mass. If the system desires to move the balancing mass, the stepper motors are both activated, producing zero net torque yet moving the balancing mass. This system can be implemented at NPS with a low cost. Two ABUs mounted under the table surface with the bar masses parallel with the X_C and Z_C axes will provide balancing control in a fashion emulating magnetic torquers. A third ABU mounted with the bar mass perpendicular to the table will provide control in the Y_C axis.

Reactionless Automatic Balancing Unit

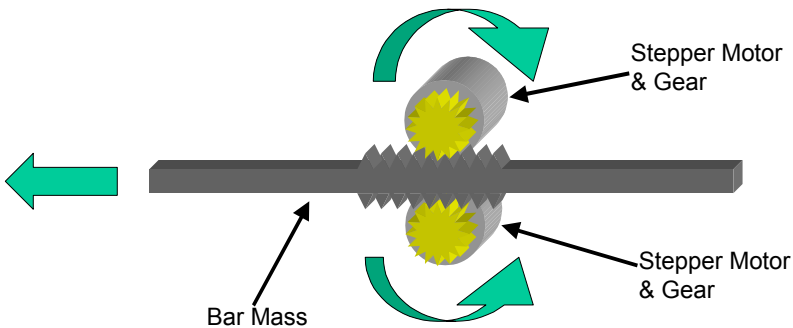


Figure 47. Reactionless Automatic Balancing Unit

2. CAD Principal Axes Determination

The determination of principal axes and mass properties for the TASS is based on experimentation and (in many cases) rough estimates of component mass. A solid modeling package such as SolidWorks would greatly reduce the amount of guesswork and experimentation required to produce mass properties data. The construction of a solid model of the TASS should be undertaken in order to provide an accurate model, and these results validated with experimental results.

This solid modeling will not be an isolated, one-time event. Any future revision of the TASS should include a component mass properties list, indicating the exact mass and dimensions of each component added to the table. This would allow the TASS users to mount the new hardware in such a fashion as to minimally (or favorably) change the mass properties and principal axes of the table.

In short, solid modeling provides not only a modeling tool for current table configuration, but also a planning tool used in the design and placement of future TASS payloads.

C. SYSTEM CHARACTERIZATION

1. Gain Determination

The gains determined for the TASS are experimentally determined based on actual system response. This system response is highly dependant upon the state of balance of the table, which is variable from day to day. This makes it difficult to create a system model that will hold for all states of balance.

It is possible to construct a dynamic model for the table in its condition of optimum balance, based on the moments of inertia previously calculated. Such a model can be constructed using a software package such as SIMULINK. This would allow for the determination of the proportional and derivative gains for each axis.

With the optimal gains determined, small out-of-balance conditions could be simulated by applying a small constant torque to an axis, and an integral gain determined for a wide range of conditions. This would only hold for conditions close to the optimal balance position, as the proportional and derivative gains will begin to change as their optimum position is departed.

2. Alternate Control Methods

There are other methods of control that may be better suited to controlling the TASS. Control methods based on neural networks, or adaptive control methods can be implemented in order to deal with the variables inherent in table operation. An adaptive control law capable of adjusting its own gains in response to a table that is out of balance will provide a much more robust response compared to a static PID controller.

VI. SUMMARY AND CONCLUSIONS

This experimentation and development with the TASS and BRMP has proven technologies vital to the Bifocal Relay Mirror project. Beam steering, control, and jitter reduction within the BRMP were successful, and system performance of the TASS was successful, with the exception of sun sensor position accuracy about one axis.

The TASS hardware saw many changes, including the integration of the BRMP, the addition of a video power supply unit, and the installation of voltage/current clamps on each reaction wheel circuit. The power system is awaiting parts for a two-phased upgrade to enhance the capacity and flexibility of the system, and the mass properties have been analytically determined and validated against experimental data. Signal processing algorithms were applied to the rate gyro and sun sensor signals, extracting useful data in all cases except the Y_C -axis sun sensor.. The Y_C -axis sun sensor was determined to have insufficient resolution for sustained BRMP operations, and alternative attitude determination methods were explored. The PID controller implemented was successful, as were the direction cosine matrices used to shuttle between control axes and principal axes. Several areas for future research were also identified and discussed, including advanced methods of automatic table balancing, development of a TASS dynamic system model for control law testing and gain determination, and the use of CAD for planning and mass properties determination.

The TASS is a test bed for satellite attitude control research in support of experimental payloads such as the bifocal relay mirror. It has evolved throughout this experiment, and it will continue to evolve as future experiments present new requirements. As a student tool, and as hardware supporting national interests, the Three Axis Satellite Simulator continues to be a successful, vital program.

THIS PAGE INTENTIONALLY LEFT BLANK

APPENDIX A: MASS PROPERTIES SPREADSHEET

Description	Weight (lb)	X Loc(in)	Y Loc(in)	Z Loc(in)	X Dim(in)	Y Dim(in)	Z Dim(in)
Rate Gyro Mounting Fixture	2	3.5	10	4	3.75	3.85	2.8
Reaction Wheel Mounting Fixture	4.66	-13	0	9.3	0.5	11.5	12
Reaction Wheel Mounting Fixture	4.66	0	13.8	9.3	11.5	0.5	12
Overspeed electronics	2	-17	-12.5	4.3	4.7	3.7	2.4
Triaxial magnetometer	0.0837	19.4	-11.4	3.8	3	0.8	0.8
Sun Sensor Assembly	2	0	0	13	4.6	2.3	7.5
Power Distribution/Thruster Driver Electronic	2	16	9	4.33	6.5	4.8	2.3
RF Transmitter	1	3.5	-17.5	4.33	3.2	5.2	1.6
12 VDC Battery	6.2	6	-3.5	4.3	3.5	6	2.6
12 VDC Battery	6.2	6	3.5	4.3	3.5	6	2.6
6 VDC Battery	4.4	-12	-18	4	6	3.7	1.4
Thruster Mounting Block 1	1	24	0	5	2.5	2.5	2.5
Thruster Mounting Block 2	1	0	-24	5	2.5	2.5	2.5
Thruster Mounting Block 3	1	-24	0	5	2.5	2.5	2.5
Thruster Mounting Block 4	1	0	-24	5	2.5	2.5	2.5
Notebook PC and DAC cards	4	15.3	0	5.75	10	12.6	1.5
Rate Gyro (Inner)	2.25	3	7	4.5	3	2	2
Rate Gyro (Top)	2.25	3	10	6.5	3	2	2
Rate Gyro (Other)	2.25	5.5	10	4.5	2	3	2
20 N-m-s Reaction Wheel	20.7	-12	-1	10.42	2.5	10	10
20 N-m-s Reaction Wheel	20.7	0	16.5	10.42	10	2.5	10
20 N-m-s Reaction Wheel	20.7	0	-11	6.8	10	10	2.5
Gas Cylinder #1 (Under Sun Sensor)	5.7	15	15	-1.3	6	6	11
Gas Cylinder #2 (Under Mirror)	5.7	-15	-15	-1.3	6	6	11
Platform	70	0	0	3	48	48	0.375
Spherical Ball Segment	39.5	0	0	-2.875			
Ballast Weight 1	33	5.5	-23.5	-1.5	4	4	8.7
Ballast Weight 2	33	-23.5	-5.5	-1.5	4	4	8.7
Ballast Weight 3	33	23.5	5.5	-1.5	4	4	8.7
Ballast Weight 4	33	-5.5	23.5	-1.5	4	4	8.7
Leg Shaft 1	3	24.5	-7	-5	1.5	1.5	16
Leg Shaft 1 Weight	8	24.5	-7	-15	4	4	2.5
Leg Shaft 2	3	-7	-24.5	-5	1.5	1.5	16
Leg Shaft 2 Weight	8	-7	-24.5	-15	4	4	2.5
Leg Shaft 3	3	7	24.5	-5	1.5	1.5	16
Leg Shaft 3 Weight	8	7	24.5	-15	4	4	2.5
Leg Shaft 4	3	-24.5	7	-5	1.5	1.5	16
Leg Shaft 4 Weight	8	-24.5	7	-15	4	4	2.5
Fine Balance Block	1	18	-3.7	0	2	2	3.5
Fine Balance Weight 'X' (In Y Dir)	3.8	18	4	-0.5	4	1	4
Fine Balance Weight 'Y' (In X Dir)	3.8	26	-3.7	-0.5	1	4	4
Fine Balance Weight Z	3.8	18	-3.7	-8	4	4	1
Electronics Aluminum Plate	1	13.5	-13.5	4	10.5	10.5	0.2
Optics aluminum plate	1	-13	13	4	10	20	0.2
Video Camera	1	-9	24	10	7	3	2
Optics (Approximate all as single mass)	0.5	-12	11	10	2	2	8
FSM	1	-21.5	5.5	10.5	2	5	5
AFRL Boxes	2	11	-17	7	8	8	4.5
Transmitter	0.5	-4	-18	3.5	3	6	1.5
Receiver	0.5	-19.5	-5.5	4	5.5	4	2
Video Power Supply	0.7	-5.5	-21	4	4	4.5	2
Weight Total (lbs):	429.5537						

Table 7. Mass Properties – Positions and Dimensions

Description	Shape	Rotation(Rad)	I _{x'x'}	I _{y'y'}	I _{z'z'}	I _{x'y'=l'y'x'}	I _{xx}	I _{yy}	I _{zz}
Rate Gyro Mounting Fixture	Box	0	3.777083	3.650417	4.814167		0	235.7771	60.27708
Reaction Wheel Mounting Fixture	Box	0	107.2771	56.01708	51.45417		0	510.3205	1297.86
Reaction Wheel Mounting Fixture	Box	0	56.01708	107.2771	51.45417		0	1346.511	459.0605
Overspeed electronics	Rot Box	-0.785398163	3.941667	3.941667	5.963333	-0.7	353.4217	618.9217	894.441667
Triaxial magnetometer	Rot Box	-0.785398163	0.038084	0.038084	0.067239	-0.0291555	12.12436	32.74804	42.4170675
Sun Sensor Assembly	Rot Box	-0.785398163	11.57917	11.57917	4.408333	-1.3225	349.5792	349.5792	11.5791667
Power Distribution/Thruster Driver Electronics	Box	0	4.721667	7.923333	10.88167		0	204.2195	554.2195
RF Transmitter	Box	0	2.466667	1.066667	3.106667		0	327.4656	33.46557
12 VDC Battery	Box	0	22.09267	9.821833	24.92917		0	212.6807	359.9307
12 VDC Battery	Box	0	22.09267	9.821833	24.92917		0	212.6807	359.9307
6 VDC Battery	Rot Box	-0.785398163	9.8285	9.8285	18.21967	-4.0901667	1505.829	713.8285	2069.0285
Thruster Mounting Block 1	Box	0	1.041667	1.041667	1.041667		0	26.04167	602.0417
Thruster Mounting Block 2	Box	0	1.041667	1.041667	1.041667		0	602.0417	26.04167
Thruster Mounting Block 3	Box	0	1.041667	1.041667	1.041667		0	26.04167	602.0417
Thruster Mounting Block 4	Box	0	1.041667	1.041667	1.041667		0	602.0417	26.04167
Notebook PC and DAC cards	Box	0	53.67	34.08333	86.25333		0	185.92	1122.28
Rate Gyro (Inner)	Box	0	1.5	2.4375	2.4375		0	157.3125	67.3125
Rate Gyro (Top)	Box	0	1.5	2.4375	2.4375		0	321.5625	116.8125
Rate Gyro (Other)	Box	0	2.4375	1.5	2.4375		0	273	116.0625
20 N·m-s Reaction Wheel	X-Cyl	0	16.17188	180.5859	180.5859		0	2284.403	5244.503
20 N·m-s Reaction Wheel	Y-Cyl	0	140.1563	258.75	301.875		0	8023.263	2387.688
20 N·m-s Reaction Wheel	Z-Cyl	0	140.1563	140.1563	258.75		0	3602.024	1097.324
Gas Cylinder #1 (Under Sun Sensor)	XY-Cyl	-0.785398163	47.975	47.975	70.3	22.325	1340.108	1340.108	2612.975
Gas Cylinder #2 (Under Mirror)	XY-Cyl	-0.785398163	47.975	47.975	70.3	22.325	1340.108	1340.108	2612.975
Platform	Z-Cyl	0	10080.82	10080.82	20160		0	10710.82	10710.82
Spherical Ball Segment	Hemi						323	323	418
Ballast Weight 1	Z-Cyl	0	241.1475	241.1475	66		18539.65	1313.648	19463.6475
Ballast Weight 2	Z-Cyl	0	241.1475	241.1475	66		1313.648	18539.65	19463.6475
Ballast Weight 3	Z-Cyl	0	241.1475	241.1475	66		1313.648	18539.65	19463.6475
Ballast Weight 4	Z-Cyl	0	241.1475	241.1475	66		18539.65	1313.648	19463.6475
Leg Shaft 1	Z-Cyl	0	64.42188	64.42188	0.84375		286.4219	1940.172	2012.17188
Leg Shaft 1 Weight	Z-Cyl	0	12.16667	12.16667	16		2204.167	6614.167	5206.16667
Leg Shaft 2	Z-Cyl	0	64.42188	64.42188	0.84375		1940.172	286.4219	2012.17188
Leg Shaft 2 Weight	Z-Cyl	0	12.16667	12.16667	16		6614.167	2204.167	5206.16667
Leg Shaft 3	Z-Cyl	0	64.42188	64.42188	0.84375		1940.172	286.4219	2012.17188
Leg Shaft 3 Weight	Z-Cyl	0	12.16667	12.16667	16		6614.167	2204.167	5206.16667
Leg Shaft 4	Z-Cyl	0	64.42188	64.42188	0.84375		286.4219	1940.172	2012.17188
Leg Shaft 4 Weight	Z-Cyl	0	12.16667	12.16667	16		2204.167	6614.167	5206.16667
Fine Balance Block	Box	0	1.354167	1.354167	0.666667		0	15.04417	325.3542
Fine Balance Weight 'X' (In Y Dir)	Y-Cyl	0	5.304167	7.6	8.866667		67.05417	1237.454	1297.30417
Fine Balance Weight 'Y' (In X Dir)	X-Cyl	0	0.475	5.304167	5.304167		53.447	2570.225	2621.297
Fine Balance Weight Z	Z-Cyl	0	4.116667	4.116667	7.6		299.3387	1478.517	1287.33867
Electronics Aluminum Plate	Rot Box	-0.785398163	9.190833	9.190833	18.375		0	207.4408	207.4408
Optics aluminum plate	Rot Box	-0.785398163	20.83667	20.83667	41.66667	12.5	205.8367	205.8367	358.836667
Video Camera	Rot Box	-0.785398163	2.75	2.75	4.833333	-1.6666667	678.75	183.75	659.75
Optics (Approximate all as single mass)	Z-Cyl	0	2.791667	2.791667	0.25		0	113.2917	124.7917
FSM	Box	0	4.166667	2.416667	2.416667		0	144.6667	576.66667
AFRL Boxes	Rot Box	-0.785398163	14.04167	14.04167	21.33333		0	690.0417	354.0417
Transmitter	Rot Box	-0.785398163	1.03125	1.03125	1.875	0.5625	169.1563	15.15625	171.03125
Receiver	Box	0	0.833333	1.427083	1.927083		0	23.95833	198.9583
Video Power Supply	Rot Box	-0.785398163	1.290625	1.290625	2.114583	0.12395833	321.1906	33.66563	331.165625
						I (lb-in^2)	99873.96	99270.31	153701.164
						I (slug-ft^2)	21.57277	21.44239	33.1994514
						I (kg-m^2)	29.2488	29.07202	45.0124802

Table 8. Mass Properties – Moments of Inertia

APPENDIX B: SIMULINK DIAGRAMS

Figure 48 shows the front-end control screen for the PID controller with gain inputs and rate, position, and reaction outputs. Figure 49 shows a high-level view of the hardware/software integration and the general flow of data through the controller. Figures 50, 51, and 52 are direction cosine matrices changing rate, position, and commanded position from the control axis frame to the principal axis. Figures 53, 54, and 55 show the X_p , Y_p , and Z_p axis PID controllers, and Figure 56 shows the final direction cosine matrix taking the output of these controllers and changing the commanded reaction from the principal axis frame back into the control axis frame.

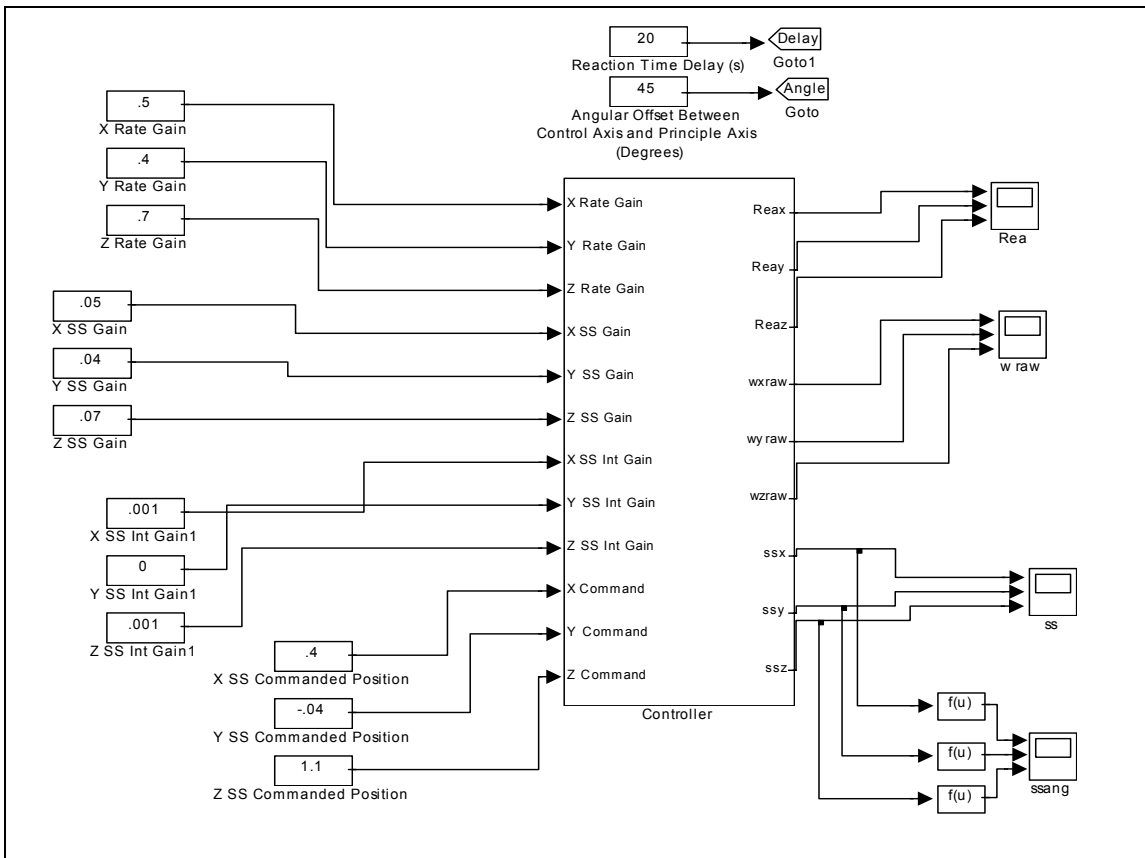


Figure 48. Controller Front End

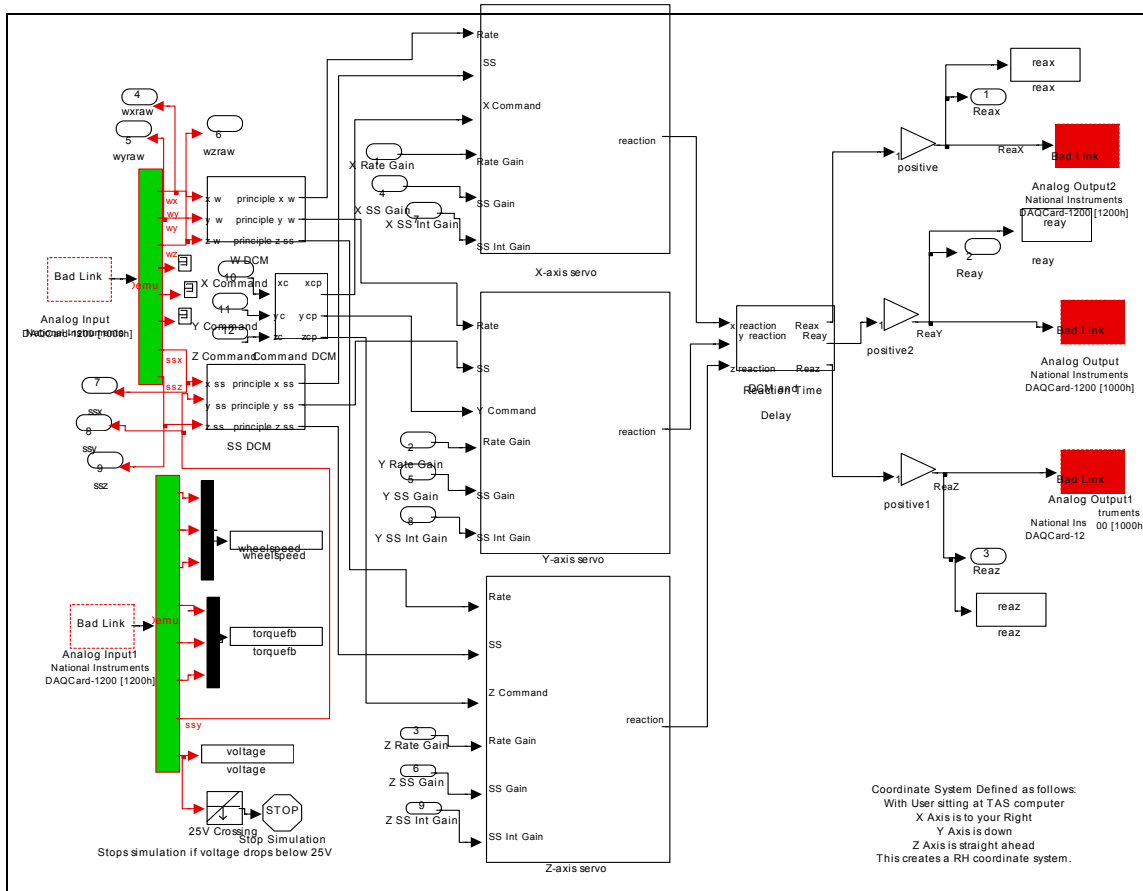


Figure 49. Hardware Interface and Data Flow

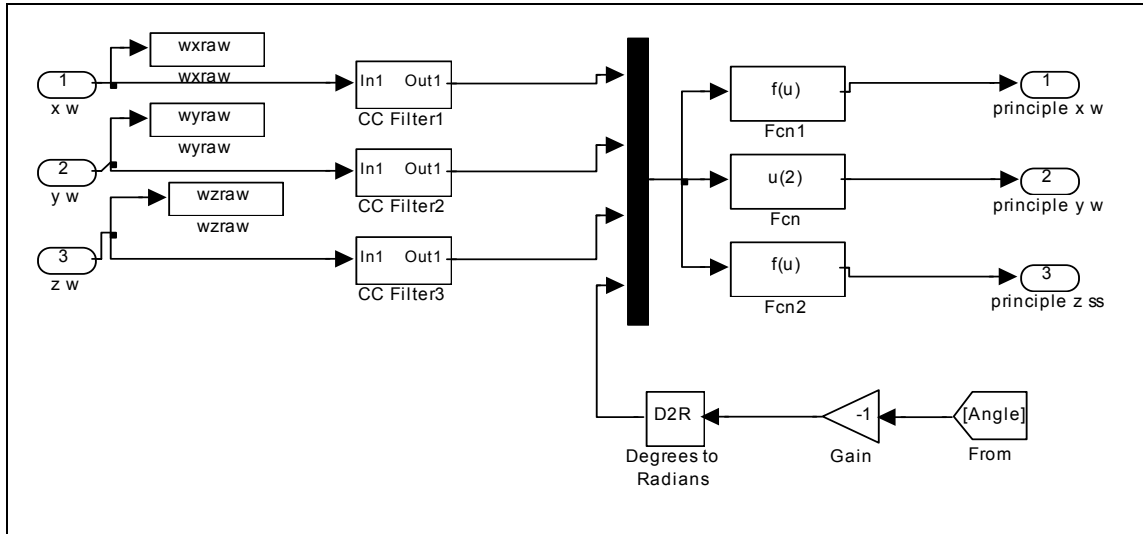


Figure 50. Rate Gyro Filtering and DCM

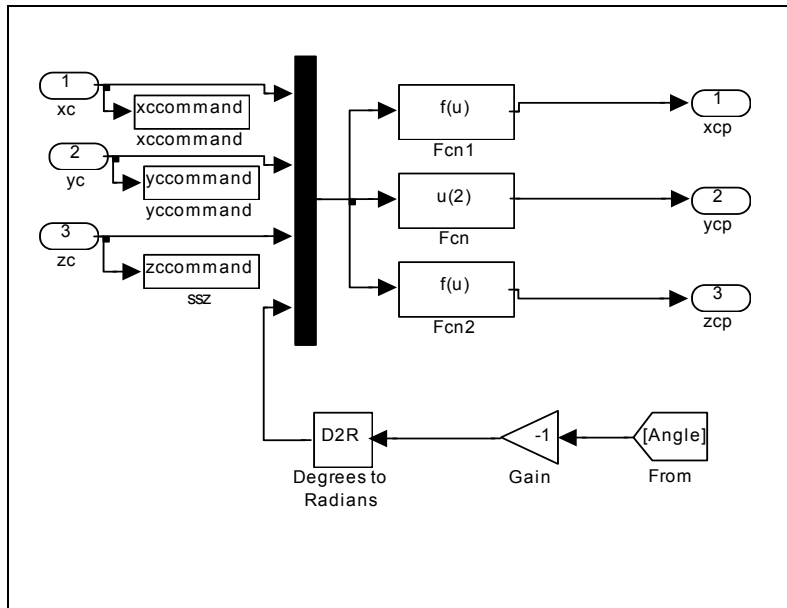


Figure 51. Commanded Position DCM

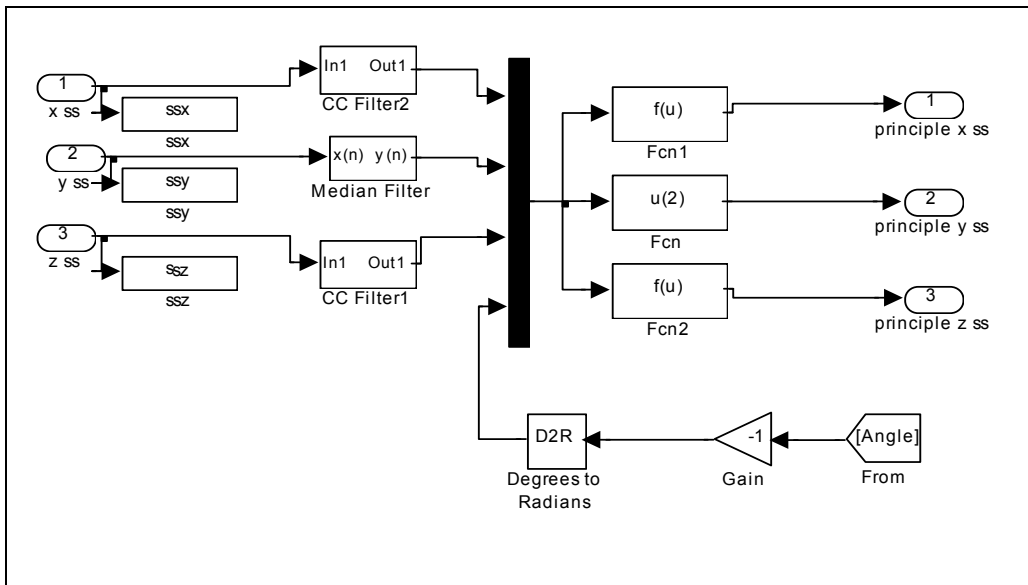


Figure 52. Sun Sensor Filtering and DCM

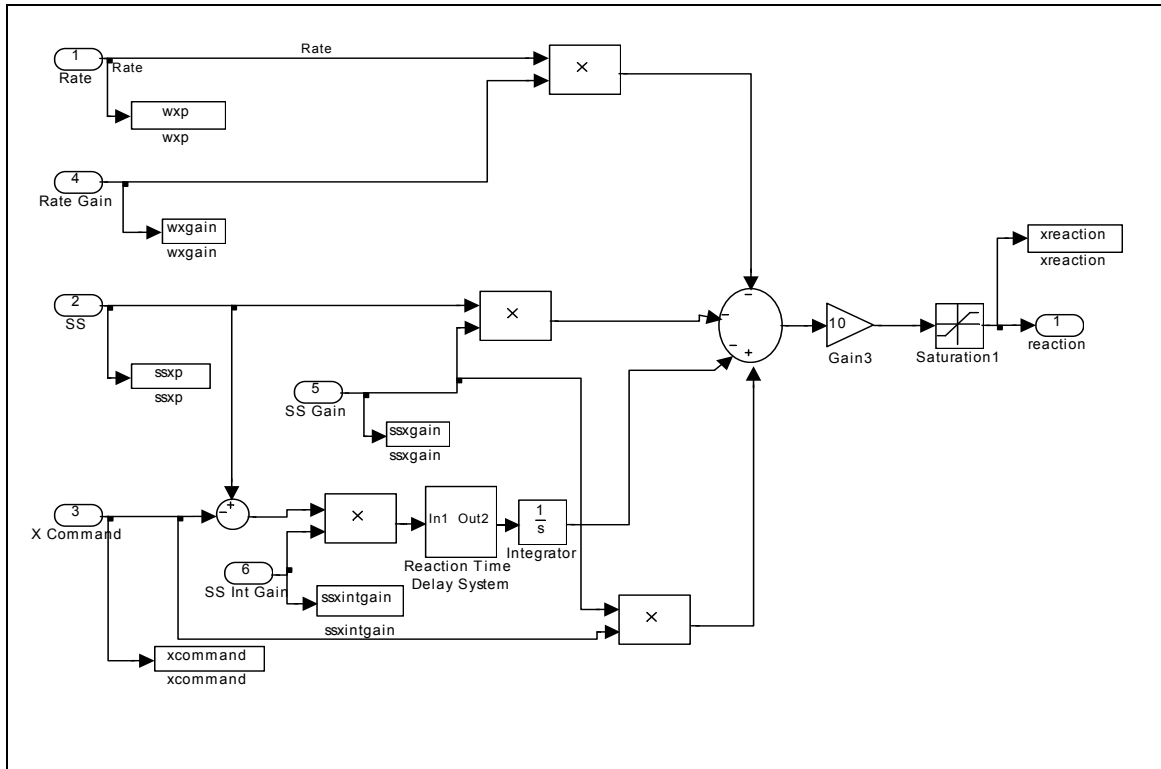


Figure 53. X_p Axis PID Controller

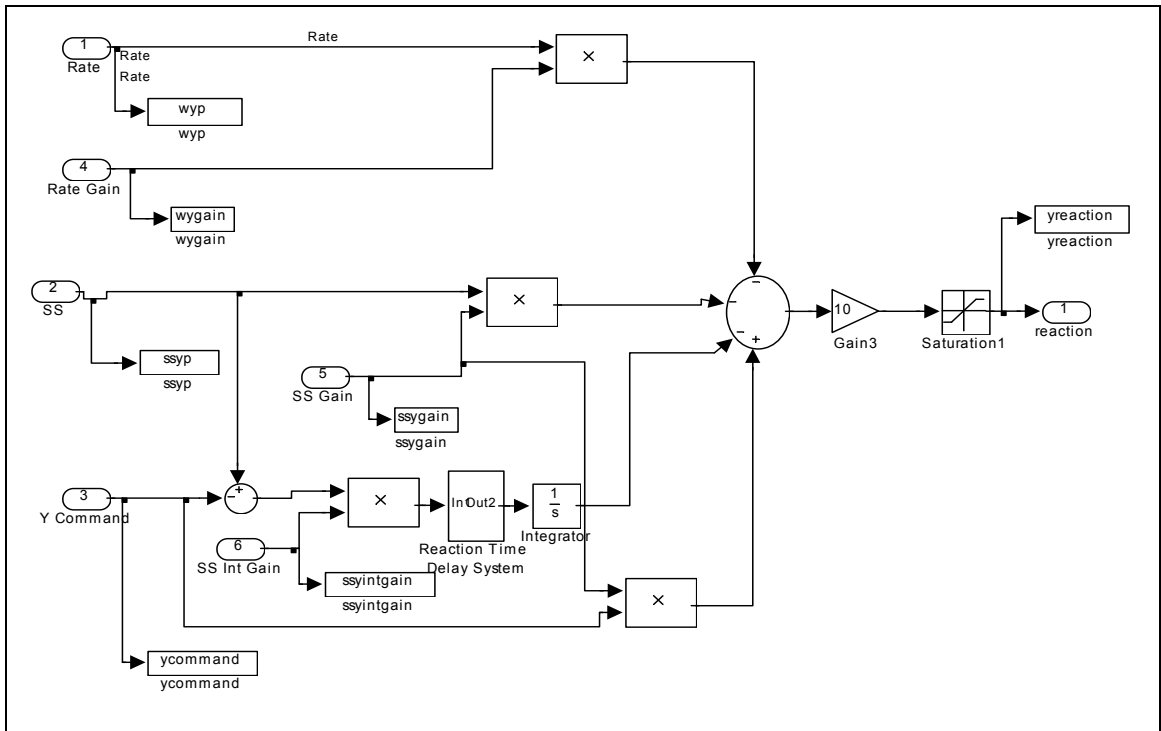


Figure 54. Y_p Axis PID Controller

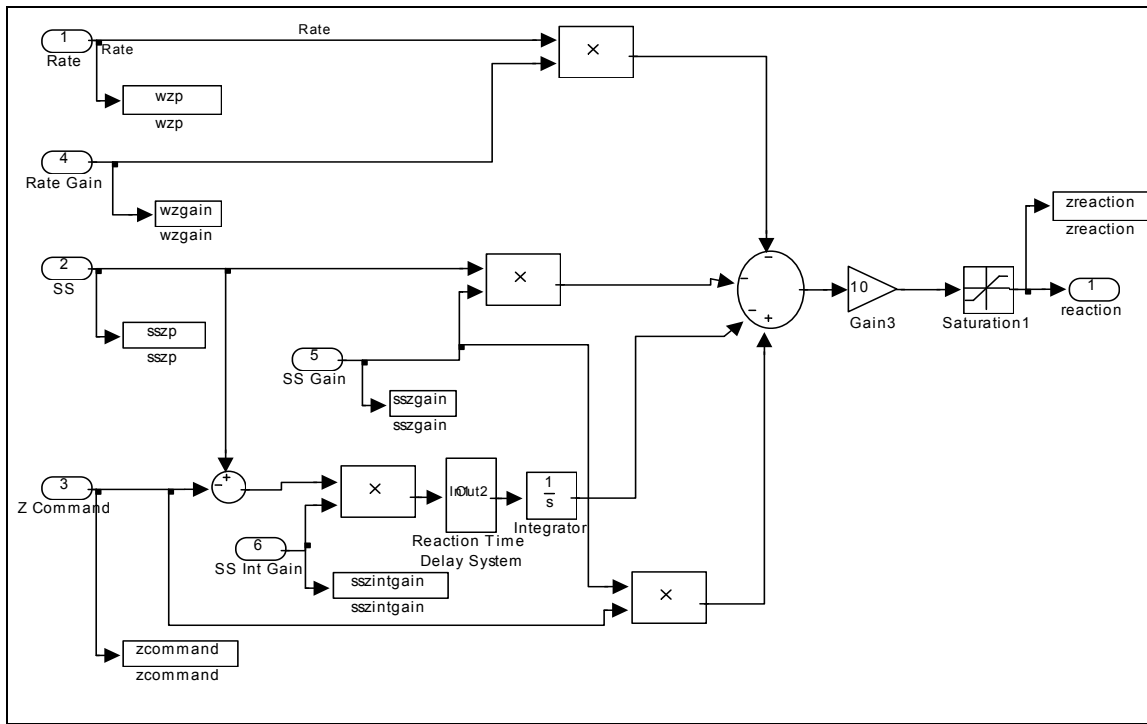


Figure 55. Z_p Axis PID Controller

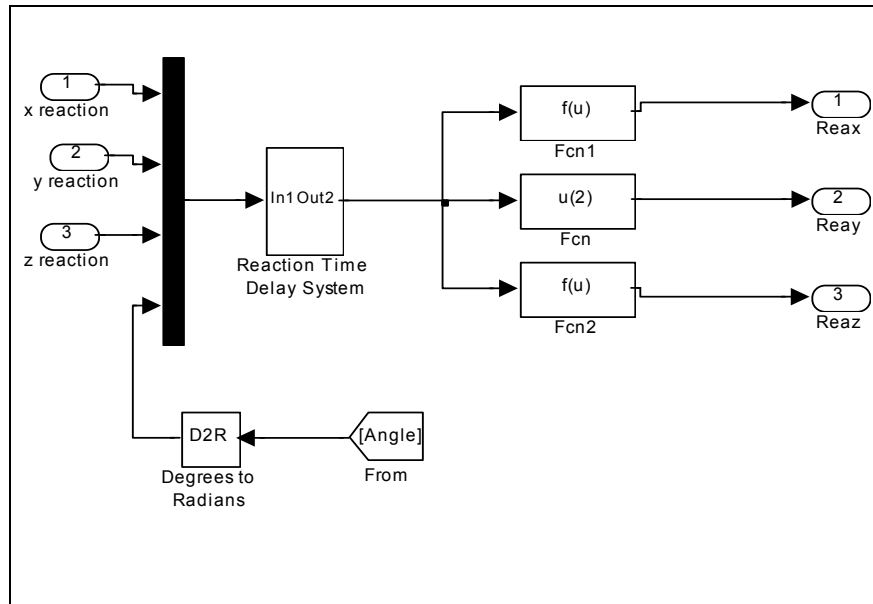


Figure 56. Reaction DCM

THIS PAGE INTENTIONALLY LEFT BLANK

APPENDIX C: VOLTAGE/CURRENT CLAMP DESIGN

This appendix contains plans for the Voltage/Current Clamp Circuit. Figure 57 is the circuit itself, and Figures 58 through 60 detail the manufacturing of the required housing.

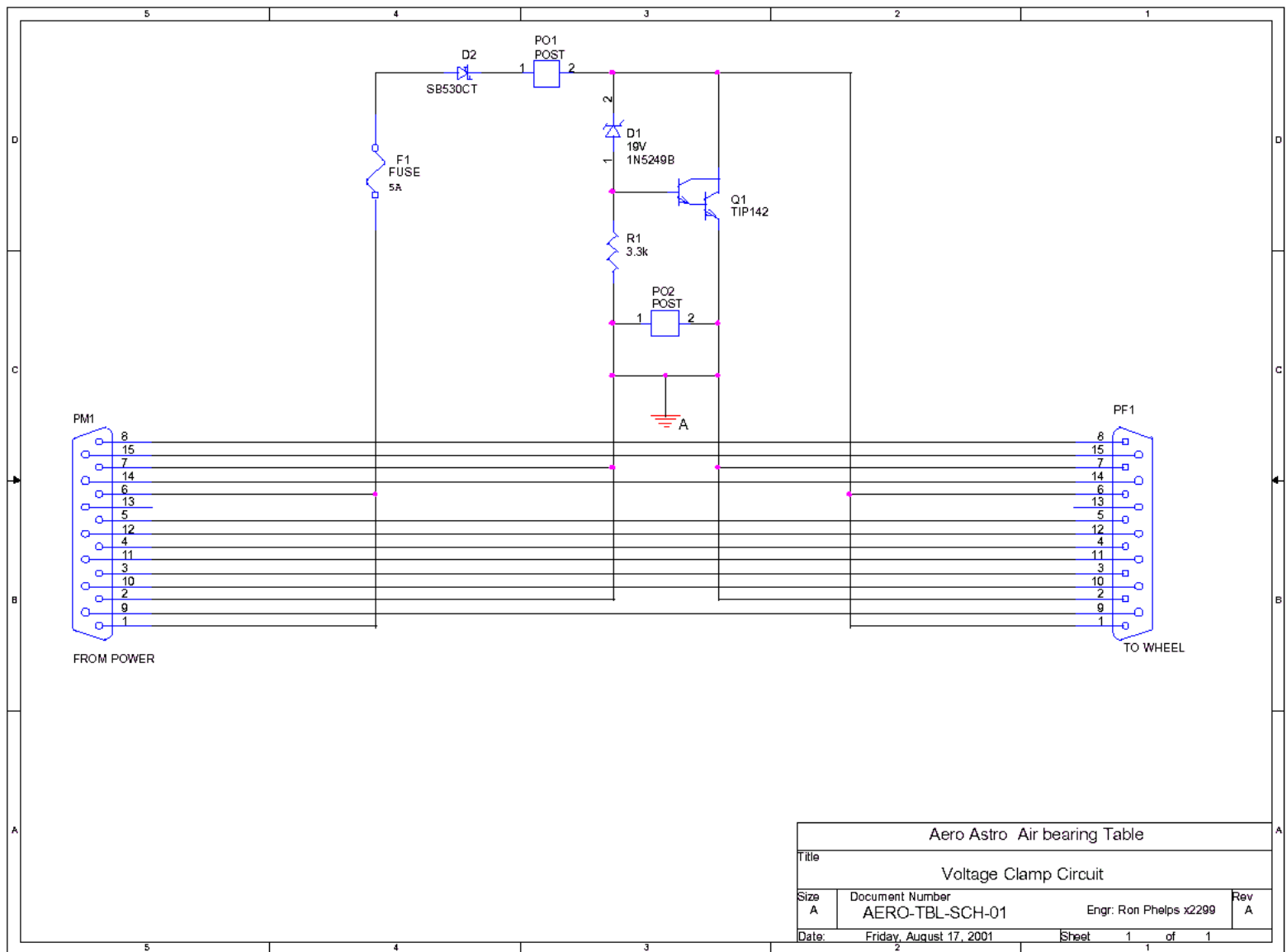


Figure 57. Voltage/Current Clamp Circuit

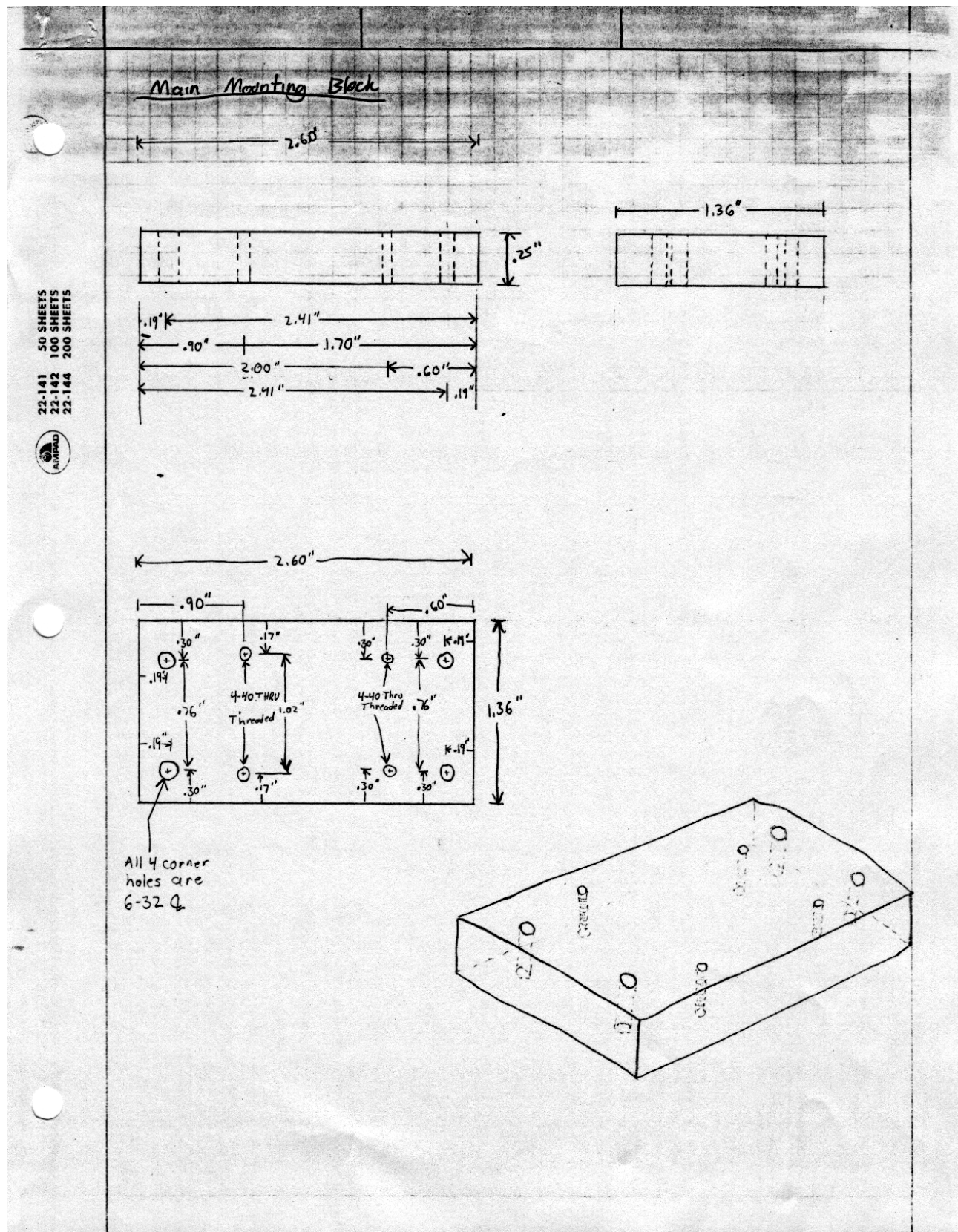


Figure 58. Clamp Circuit Housing – Base

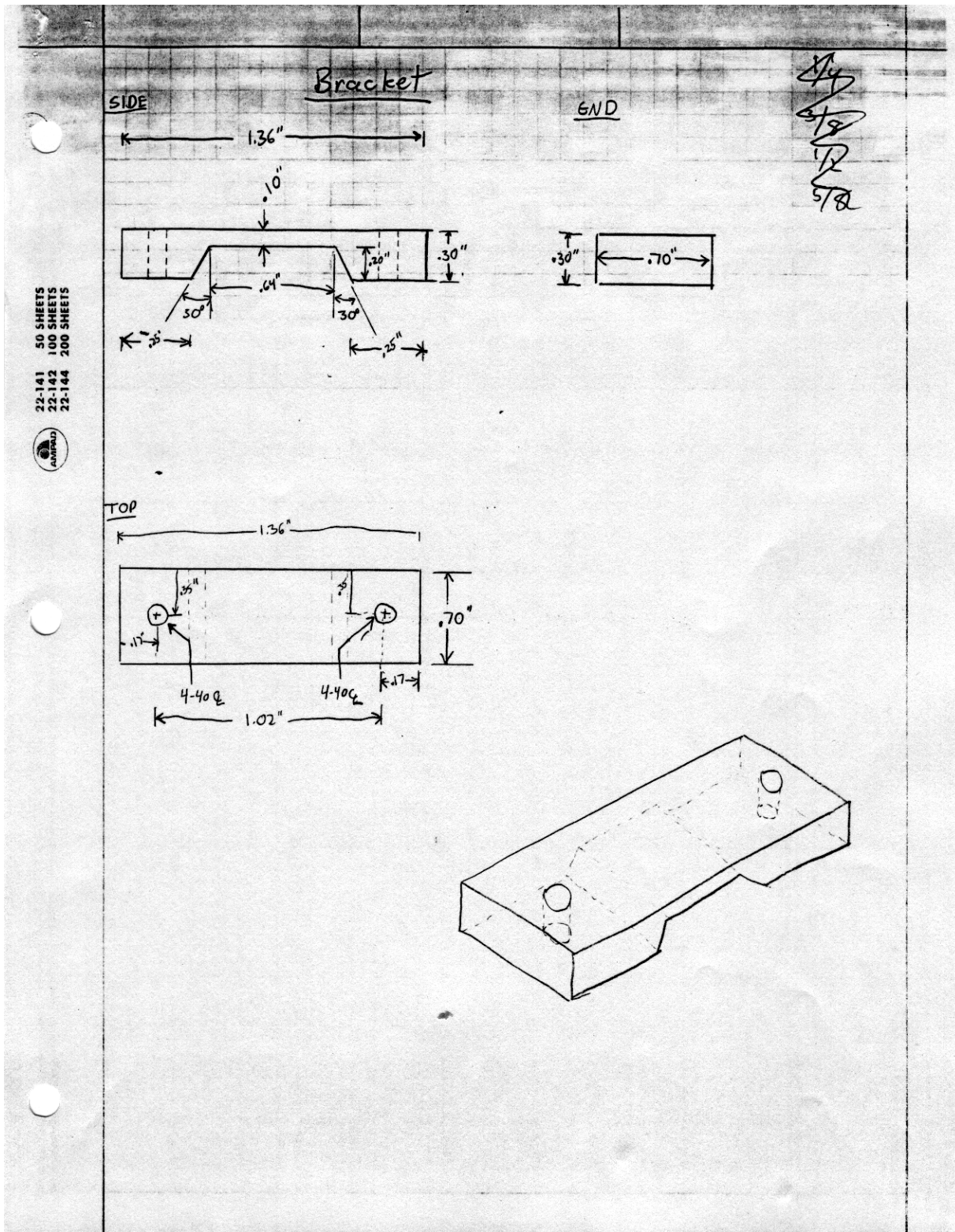


Figure 59. Clamp Circuit Housing – Transistor Restraint

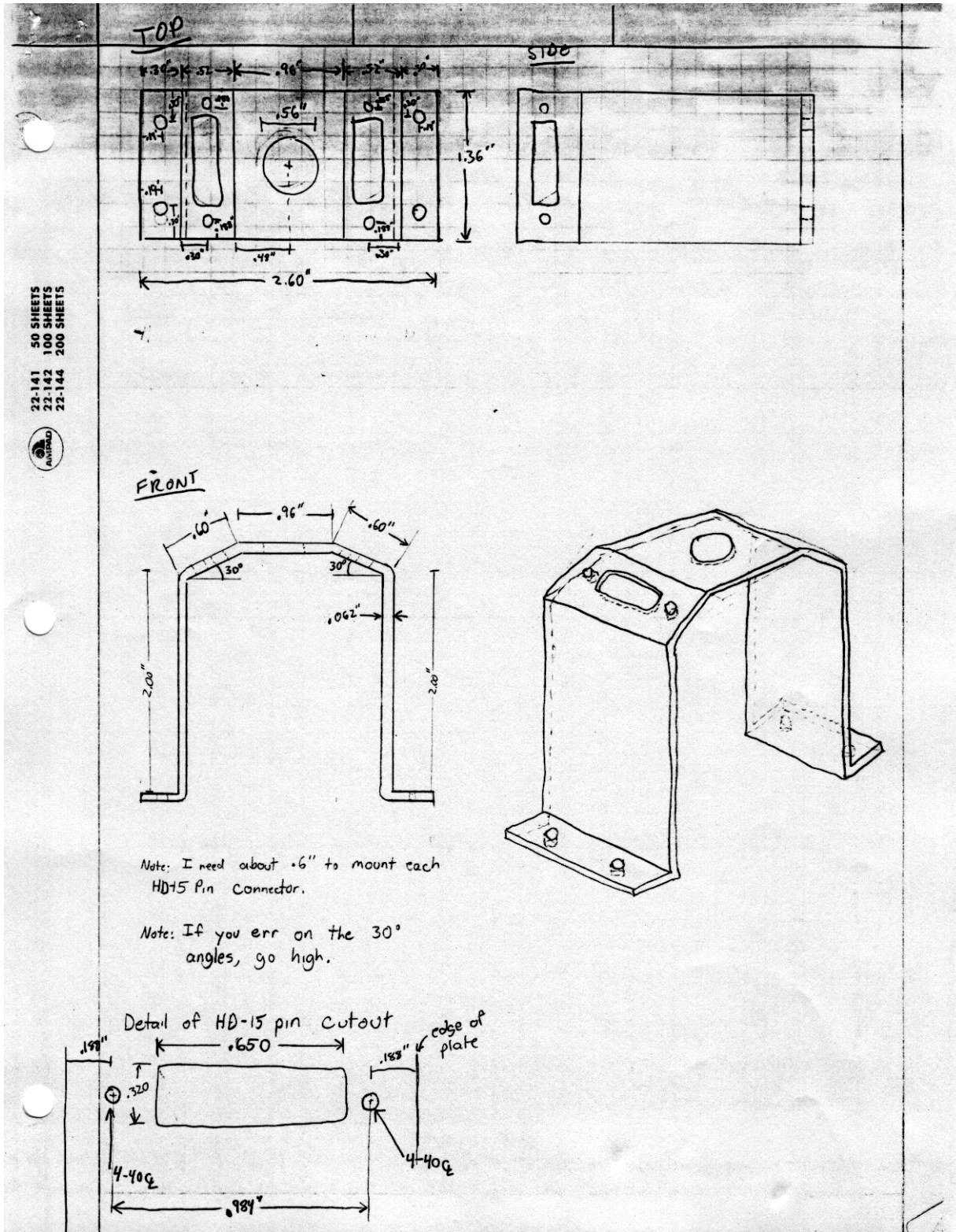


Figure 60. Clamp Circuit Housing – Mounting Shield

APPENDIX D: DAQCARD-1200 SIGNAL SUMMARY

This appendix contains a signal summary for each National Instruments DAQcard. Table 9 summarizes signals for the card at memory location 1000h, and Table 10 summarizes signals for the card at memory location 1200h.

DAQcard-1200 at Memory Location 1000h		
Analog Inputs		
Pin Number	Signal	Notes
1	X _C Rate	Noisy Signal
2	Y _C Rate	Noisy Signal
3	Z _C Rate	Noisy Signal
4	Magnetometer	DCM Required (not aligned with control axis system)
5	Magnetometer	DCM Required (not aligned with control axis system)
6	Magnetometer	DCM Required (not aligned with control axis system)
7	Z _C Sun Sensor	
8	X _C Sun Sensor	
Analog Outputs		
1	Z _C Reaction Wheel Command	Limit to ± 2 VDC
2	Y _C Reaction Wheel Command	Limit to ± 2 VDC
Digital Outputs		
1	-XC Thruster	
2	-YC Thruster	
3	+YC Thruster	
4	+ZC Thruster	
5	+XC Thruster	
6	+YC Thruster	
7	-ZC Thruster	
8	-YC Thruster	
9-24	Unused	

Table 9. Signal Summary for DAQcard at Memory Location 1000h

DAQcard-1200 at Memory Location 1200h		
Analog Inputs		
Pin Number	Signal	Notes
1	Y_C Wheel Speed	
2	Z_C Wheel Speed	
3	X_C Wheel Speed	
4	Y_C Torque Feedback	
5	Z_C Torque Feedback	
6	X_C Torque Feedback	
7	Y_C Sun Sensor	
8	Bus Voltage	= (Bus Voltage) / 10
Analog Outputs		
1	X_C Reaction Wheel Command	Limit to ± 2 VDC
2	Unused	
Digital Outputs		
1-24	Unused	

Table 10. Signal Summary for DAQcard at Memory Location 1200h

APPENDIX E: VIDEO HARDWARE DIAGRAMS

Figures 61 and 62 outline the wiring connections made while integrating the BRMP onto the TASS.

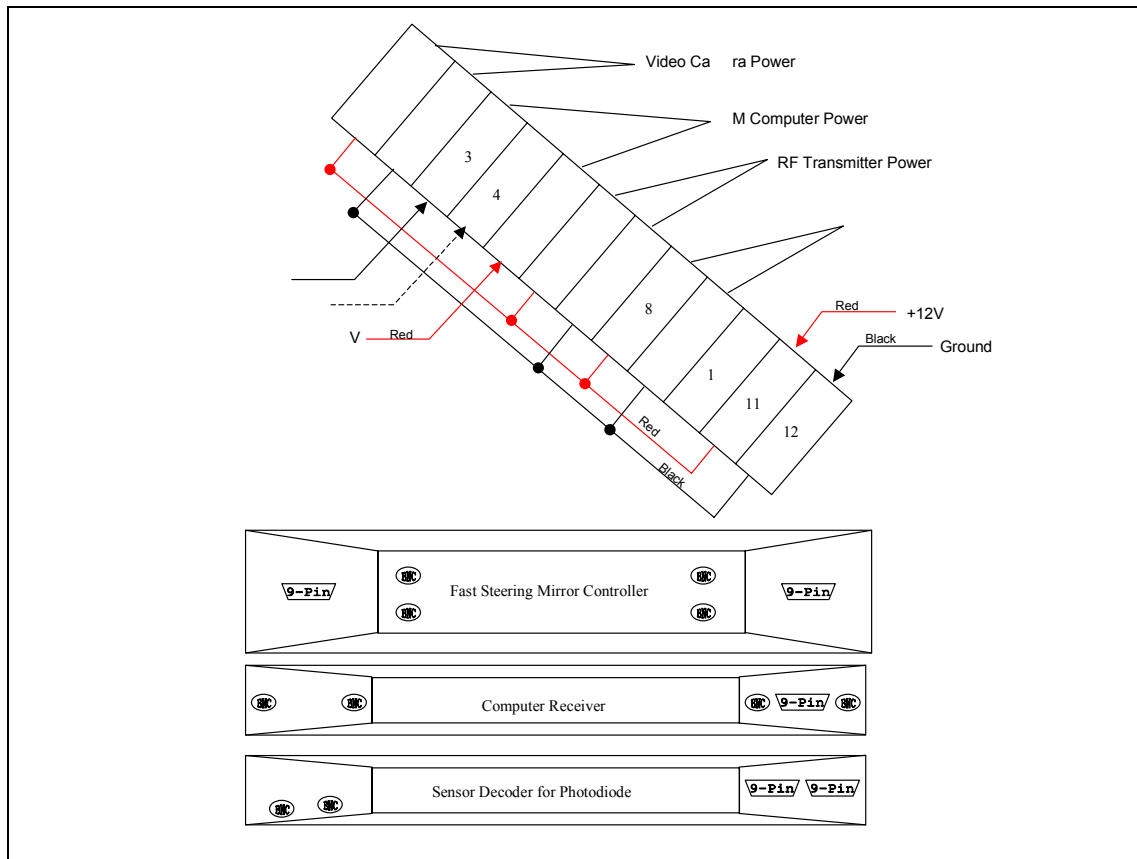


Figure 61. Terminal Strip Wiring Diagram

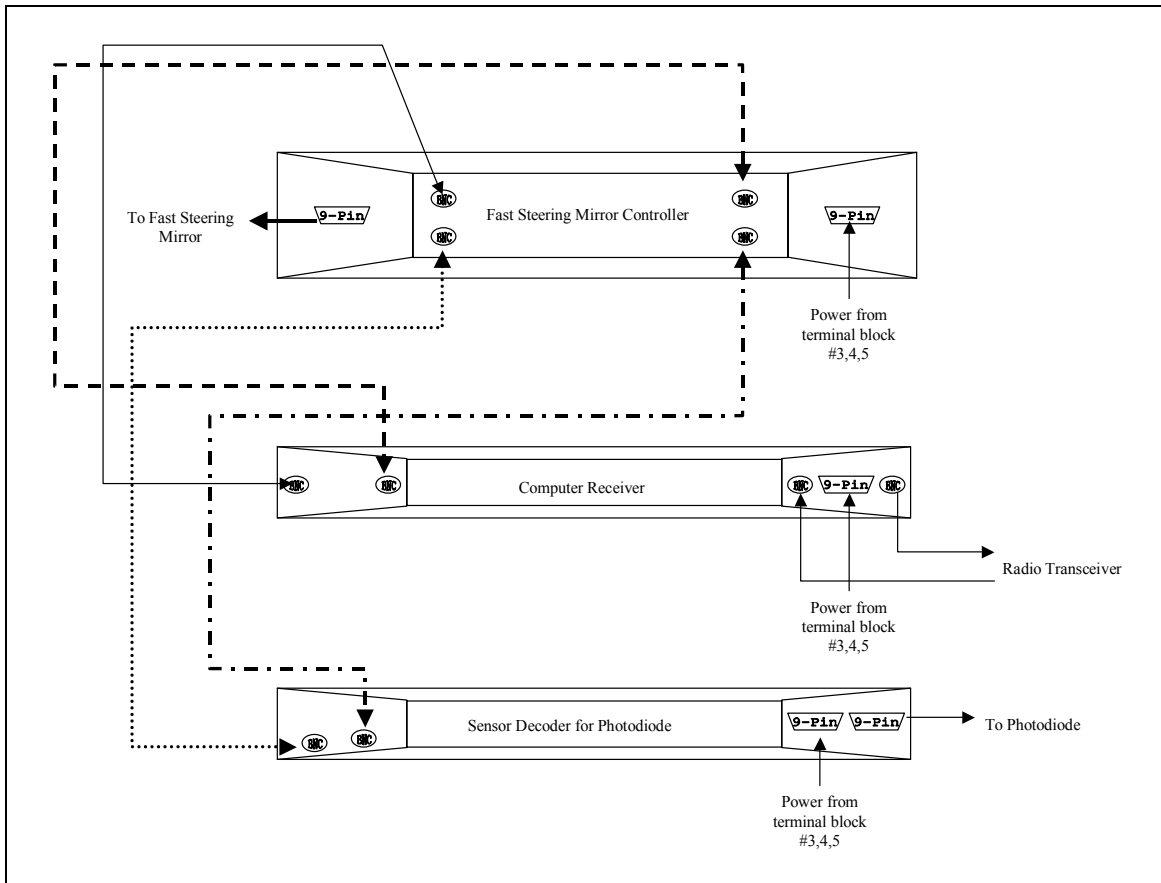


Figure 62. AFRL Controller Hardware Wiring Diagram

APPENDIX F: POWER ANALYSIS

Table 11 outlines the average power requirements for all TASS systems. Table 12 is similar, outlining the maximum power requirements.

TASS Power Requirements Summary - Average Power Consumption				
Component	Nominal Voltage (VDC)	Average Current (A)	Average Power (W)	
<u>28VDC Supplied Components</u>				
Rate Gyro #1	28	0.36	10.08	
Rate Gyro #2	28	0.36	10.08	
Rate Gyro #3	28	0.36	10.08	
Reaction Wheel #1	18	0.83	14.94	
Reaction Wheel #2	18	0.83	14.94	
Reaction Wheel #3	18	0.83	14.94	
Magnetometer	12	0.017	0.204	
RF Modem	5	0.0016	0.008	
Sun Sensor	28	0.1	2.8	
Valve Driver	28	3	84	
Control Electronics	28	0.5	14	<u>28VDC Max Subtotal (W)</u>
				176.072
<u>+/-12VDC Components</u>				
FSM/AFRL Computers	12	0.4	4.8	<u>+/-12VDC Max Subtotal (W)</u>
				4.8
<u>12VDC Components</u>				
Transmitter	12	0.2	2.4	
Receiver	12	0.2	2.4	
Video Camera	12	0.5	6	<u>12VDC Max Subtotal (W)</u>
				10.8
Totals		8.4886	191.672	
With 15% Margin		9.76189	220.4228	

Table 11. TASS Average Power Requirements

TASS Power Requirements Summary - Maximum Power Consumption				
Component	Nominal Voltage (VDC)	Max Current (A)	Max Power (W)	
<u>28VDC Supplied Components</u>				
Rate Gyro #1	28	0.39	10.92	
Rate Gyro #2	28	0.39	10.92	
Rate Gyro #3	28	0.39	10.92	
Reaction Wheel #1	18	4.33	77.94	
Reaction Wheel #2	18	4.33	77.94	
Reaction Wheel #3	18	4.33	77.94	
Magnetometer	12	0.017	0.204	
RF Modem	5	0.0016	0.008	
Sun Sensor	28	0.1	2.8	
Valve Driver	28	3	84	
Control Electronics	28	0.5	14	<u>28VDC Max Subtotal (W)</u>
				367.592
<u>+/-12VDC Components</u>				
FSM/AFRL Computers	12	0.4	4.8	<u>+/-12VDC Max Subtotal (W)</u>
				4.8
<u>12VDC Components</u>				
Transmitter	12	0.2	2.4	
Receiver	12	0.2	2.4	
Video Camera	12	0.5	6	<u>12VDC Max Subtotal (W)</u>
				10.8
Totals		19.0786	383.192	
With 15% Margin		21.94039	440.6708	

Table 12. TASS Maximum Power Requirements

APPENDIX G: VIDEO POWER SCHEMATIC

Figure 63 is a schematic of the Video Power Supply.

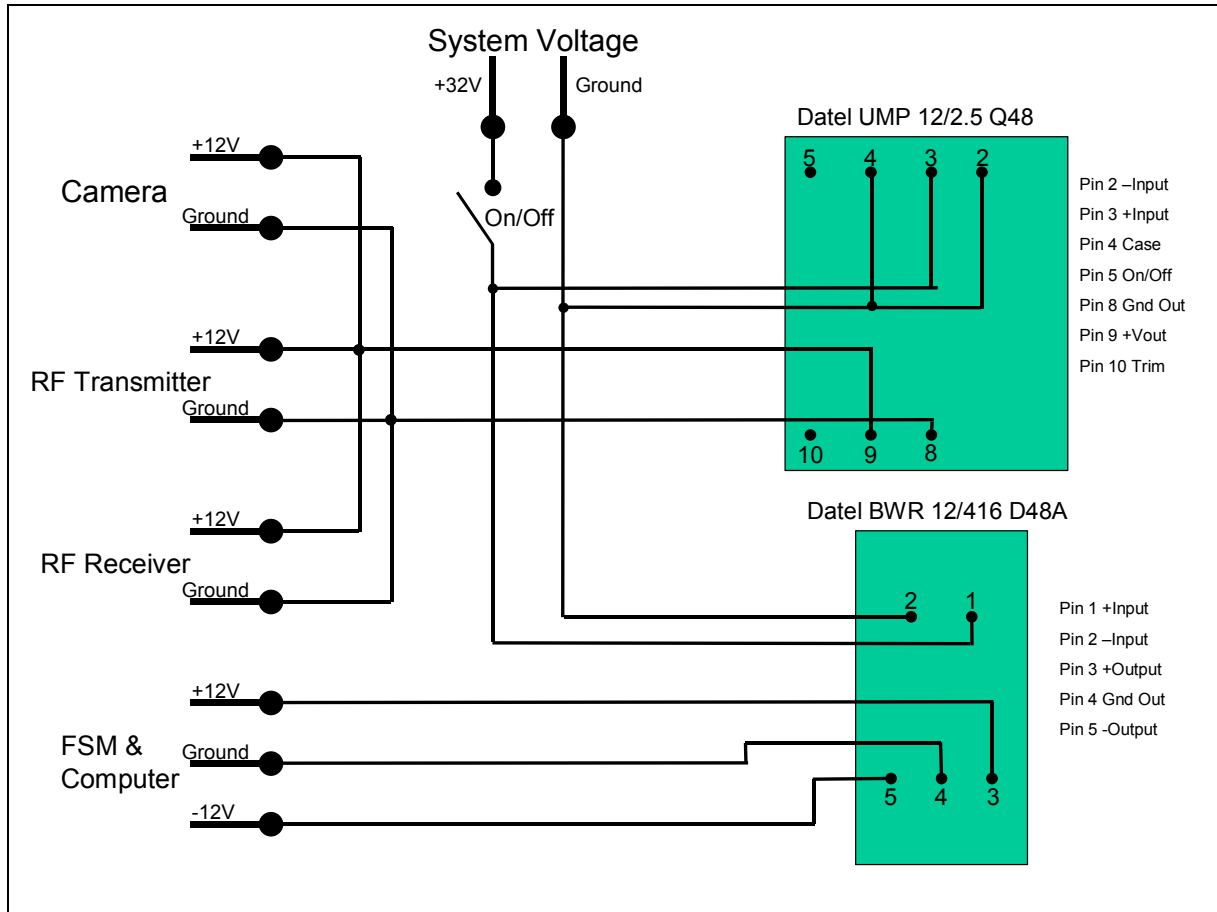


Figure 63. Video Power Supply Schematic

THIS PAGE INTENTIONALLY LEFT BLANK

LIST OF REFERENCES

1. Strategic Defense Initiative Organization, *Program Summary: Relay Mirror Experiment and Wideband Angular Vibration Experiment*, Washington, D.C., 1992.
2. Advanced Spacecraft Design Team, *MITHRA Relay Mirror Satellite*, Naval Postgraduate School, Monterey, California, September 2000.
3. National Reconnaissance Office (AS&T), *Director's Innovation Initiative: FY 2001 Government Sources Sought Announcement*, Chantilly, Virginia, 2001.
4. Guidance Dynamics Corporation, "Satellite Attitude Dynamics Simulator: Pneumatics & Mechanics Operating Manual", Simi Valley, California, 2000.
5. Automated Controlled Environments Inc., "Satellite Attitude Dynamics Simulator: Electronics Operating Manual", California, 2000.
6. Wertz, J.R., *Spacecraft Attitude Determination and Control*, D. Reidel Publishing Company, 1978.
7. Strum, R. D. and Kirk, D.E., *Discrete Systems and Digital Signal Processing*, Addison-Wesley, 1989.
8. Franklin, G.F., Powell, J.D., and Emami-Naeini, A., *Feedback Control of Dynamic Systems*, 3rd ed, Addison-Wesley, 1994.
9. Leonard, B., "Spacecraft Dynamics & Control Notes", Naval Postgraduate School, 2000.
10. Psiaki, Mark L., "Attitude Sensing Using a Global-Positioning-System Antenna on a Turntable", AIAA-2000-3947, Ithaca, New York, 2000.
11. Stone, J, LeMaster, E., Powell, J., Rock, S., "GPS Pseudolite Transceivers and their Applications", Stanford University, CA, 1999.
12. Purivigraipong, S., "Stand Alone Spacecraft Attitude Determination Using GPS Signals", University of Surrey, UK, 2000.
13. Conversation between Christopher B. Dunbar, Director (Electromechanical Control Department), The Aerospace Corporation and author, 22 November 2001.
14. Kim, B., Velenis, E., Kriengsiri, P., Tsiotras, P., "A Spacecraft Simulator for Research and Education", AAS 01-367, Atlanta, Georgia, 2001.

15. Fullmer, R., Peterson, G., Holmans, W., et. al., "The Development of a Small Satellite Attitude Control Simulator", Logan, Utah.

INITIAL DISTRIBUTION LIST

1. Defense Technical Information Center
Ft. Belvoir, Virginia
2. Dudley Knox Library
Naval Postgraduate School
Monterey, California
3. Department Chairman
Department of Aeronautics and Astronautics
Monterey, CA
4. Department of Aeronautics and Astronautics
Professor Michael G. Spencer
Naval Postgraduate School
Monterey, CA
5. Department of Aeronautics and Astronautics
Professor Brij N. Agrawal
Naval Postgraduate School
Monterey, CA
6. LT Vincent S. Chernesky, USN
Stratford, CT

THIS PAGE INTENTIONALLY LEFT BLANK